

# **The Astro-E2 Technical Description**

Announcement of Opportunity #1

Institute of Space and Astronautical Science (ISAS/JAXA)  
and the  
Laboratory for High Energy Astrophysics  
NASA/Goddard Space Flight Center

# Contents

<b>1</b>	<b>Introduction</b>	<b>2</b>
<b>2</b>	<b>Mission Description</b>	<b>4</b>
2.1	A Brief Introduction to <i>Astro-E2</i> . . . . .	5
2.2	Operational Constraints of <i>Astro-E2</i> . . . . .	9
2.2.1	Raster-scanning . . . . .	9
2.2.2	Cooling system constraints . . . . .	10
2.2.3	Telemetry rates . . . . .	10
2.3	Features and Capabilities of the XRS . . . . .	10
2.3.1	Design and Performance . . . . .	11
2.3.2	Unique attributes . . . . .	11
2.3.3	Characteristics . . . . .	11
2.3.4	Summary . . . . .	12
2.4	Calibration Plan . . . . .	13
<b>3</b>	<b>Observation Policies</b>	<b>18</b>
3.1	Data Rights . . . . .	19
3.2	Target of Opportunity (TOO) proposals . . . . .	19
3.3	Pointing constraints . . . . .	19
3.4	Sequence of events after submission . . . . .	20
<b>4</b>	<b>Guide to Writing An <i>Astro-E2</i> Proposal</b>	<b>22</b>
4.1	Ingredients of a Successful <i>Astro-E2</i> Proposal . . . . .	22
4.2	Using PIMMS and WebPIMMS . . . . .	22
4.3	Using XSPEC to Simulate an Observation . . . . .	23
4.3.1	Using WebSPEC to Simulate an Observation . . . . .	23
4.4	Examples . . . . .	24
4.4.1	Detailed profile of a Fe K line in an AGN . . . . .	24
4.4.2	Iron abundance in a region of a cluster of galaxies . . . . .	24
4.4.3	Measuring plasma turbulence . . . . .	25

4.5	Using XRSSIM . . . . .	27
4.5.1	An X-ray binary simulated with xrssim . . . . .	27
4.6	Using Viewing . . . . .	30
4.7	Using MAKI . . . . .	31
4.8	Guide to Using the RPS . . . . .	31
4.9	Checklist . . . . .	31
4.10	Additional Requirements for US Proposers . . . . .	32
<b>5</b>	<b>X-Ray Telescopes (XRTs)</b>	<b>33</b>
5.1	Basic Components of XRT . . . . .	34
5.1.1	Reflectors . . . . .	35
5.1.2	Pre-collimator . . . . .	36
5.1.3	Thermal Shields . . . . .	36
5.2	XRT Performance . . . . .	36
5.2.1	Effective Area . . . . .	36
5.2.2	Angular Resolution . . . . .	38
5.2.3	Optical Axes . . . . .	38
5.2.4	Focal Length . . . . .	38
5.2.5	Field of View and Stray Light . . . . .	39
<b>6</b>	<b>X-ray Spectrometer (XRS)</b>	<b>40</b>
6.1	Principles of Operation of the XRS Detector . . . . .	41
6.2	Details of the XRS Design . . . . .	43
6.2.1	XRS Cryogenic System . . . . .	43
6.2.2	XRS blocking filters . . . . .	44
6.2.3	XRS Filter Wheel and In-flight Calibration . . . . .	44
6.2.4	In-flight gain-tracking of the XRS . . . . .	45
6.3	On-board Signal Processing in the XRS . . . . .	45
6.3.1	Searching for X-ray events . . . . .	46
6.3.2	Pulse Height Determination: . . . . .	47
6.3.3	XRS Timing Accuracy . . . . .	49
6.4	XRS Background . . . . .	50
<b>7</b>	<b>X-ray Imaging Spectrometer (XIS)</b>	<b>51</b>
7.1	Overview of the XIS . . . . .	51
7.2	CCD Pixels and Coordinates . . . . .	53
7.3	Pulse Height Determination, Residual Dark-current Distribution, and Hot Pixels . . . . .	54
7.4	On-board Event Analysis . . . . .	55

7.5	Data Processing Modes . . . . .	55
7.5.1	Clock Modes . . . . .	56
7.5.2	Window and Burst Options . . . . .	56
7.5.3	Editing Modes . . . . .	58
7.5.4	Discriminators . . . . .	58
7.6	Photon pile-up . . . . .	59
7.7	Expected background rate and the telemetry limit . . . . .	60
7.7.1	Out-of-time events . . . . .	61
7.8	Radiation Damage and On-board Calibration of the XIS . . . . .	61
<b>8</b>	<b>Hard X-ray Detector</b>	<b>62</b>
8.1	GSO/BGO Counter Units . . . . .	63
8.2	PIN Diodes . . . . .	64
8.3	HXD Background, Background Rejection, and its Sensitivity . . . . .	64
8.4	Data analysis procedure . . . . .	65
<b>A</b>	<b>Acronyms</b>	<b>66</b>
<b>B</b>	<b>SWG Target List</b>	<b>68</b>
B.1	Targets Sorted by Category . . . . .	69
B.1.1	Calibration . . . . .	69
B.1.2	Gamma-Ray Burst . . . . .	69
B.1.3	Stars and Star Forming Regions . . . . .	70
B.1.4	CV'S and XRB'S . . . . .	70
B.1.5	Galactic Diffuse Emission . . . . .	71
B.1.6	Extragalactic Compact Sources . . . . .	72
B.1.7	Extragalactic Diffuse Sources . . . . .	73
B.2	Targets Sorted by RA . . . . .	73
B.3	Target Constraints . . . . .	77
<b>C</b>	<b>Important Web/e-mail/postal addresses</b>	<b>79</b>

# List of Figures

2.1	The 96 minute <i>Astro-E2</i> orbit. . . . .	4
2.2	[Left] Schematic picture of the bottom of the <i>Astro-E2</i> satellite. [Right] A side view of the instrument and telescopes on <i>Astro-E2</i> . . . . .	5
2.3	Effective area as a function of photon energy of the combined XRT + XRS system, for all 30 pixels. The upper (solid) curve shows the effective area with the open position of the filter wheel; the lower (dashed) curve shows it with the 300 $\mu\text{m}$ Be filter. . . . .	7
2.4	XIS Effective area of one XRT + XIS system, for both the FI and BI chips. . . . .	7
2.5	The XRS calorimeter array, showing the layout of the pixels. Each pixel has a dimension of 0.64 mm $\times$ 0.64 mm, corresponding to a sky projection of $\sim 0.49' \times 0.49'$ ; the entire X-ray sensitive portion of the array projects a solid angle of $\sim 2.9' \times 2.9'$ on the sky. The pixel numbers are determined by the geometry of the detector assembly; the marked but unlabeled pixel is inactive as of March 2004. In this Figure, the array is shown projected onto the sky. . . . .	8
2.6	The Encircled Energy Function (EEF) showing the fractional energy within a given radius for one quadrant of the XRT-I telescopes on <i>Astro-E2</i> at 4.5 and 8.0 keV. The XRT-S EEF is expected to be similar. . . . .	9
2.7	Total effective area of the HXD detectors, PIN and GSO, as a function of energy. . . . .	9
2.8	Comparison of the effective area of the XRS against <i>XMM-Newton</i> 's RGSs and <i>Chandra</i> 's grating instruments. . . . .	13
2.9	Comparison of the energy resolution of the XRS and XIS against <i>XMM-Newton</i> 's RGSs and <i>Chandra</i> 's grating instruments. . . . .	14
2.10	The fraction of X-ray photons processed into the "low-res," "mid-res," and "high-res" events by the XRS for a point source with a power-law spectrum ( $\Gamma = 2.0$ ) between 0.5-10 keV. The mid-res counts are separated into primary events, which have nearly the same resolution as the hi-res events, and secondary events (marked with an "S") which have somewhat lower resolution. Secondary events occur when the event time is within 142 ms of an earlier pulse (see also Fig. 6.5). . . . .	15
2.11	Similar to Fig. 2.10, but showing the counting rate as a function of source flux. This figure includes the effects of the point-spread function of the mirror. . . . .	16
5.1	Layout of the 5 XRTs on the <i>Astro-E2</i> spacecraft. . . . .	34
5.2	An <i>Astro-E2</i> X-Ray Telescope . . . . .	35
5.3	A thermal shield. . . . .	37

5.4	The predicted effective area of a quadrant of the <i>Astro-E2</i> XRT-Is compared to measurements taken at particular energies for three different XRTs. . . . .	37
5.5	(a) Encircled Energy Function at Ti-K (4.5 keV) and Cu-K (8.0 keV). (b) Point Spread Function for the same energies. . . . .	38
5.6	Stray light images of the spare quadrant in the field of view of the XIS at 45' off aaxis. The [Left] and [Right] panels correspond to the images at Al-K (1.49 keV) before and after the pre-collimator installation, respectively. In each panel the right side is dominated by a stray light component from "secondary-only reflection" while the left side is by dominated by "backside reflection." The stray flux is reduced by two orders of magnitude after the pre-collimator installation. The small filled circles in both images are identified as background particles, <i>i.e.</i> , cosmic rays. . . . .	39
6.1	The <i>Astro-E2</i> XRS in the lab. . . . .	40
6.2	A schematic diagram of the entire XRS instrument, showing the main subsystems. .	41
6.3	Principle of operation of the XRS. The deposited photon energy $E_{ph}$ creates a temperature rise $\Delta T = E_{ph}/C$ , where $C$ is the heat capacity of the pixel. The pulse subsequently decays with the time constant $\tau$ of about $C/G$ , where $G$ is the thermal conductance of the pixel supports. . . . .	42
6.4	Calibration spectrum from the XRS flight detector array showing the resolution and centroiding for emission lines between 4.5–12 keV. . . . .	46
6.5	Diagram showing the event grade determination in the XRS data processing chain.	47
6.6	[Left] XRS spectral resolution at Mg K $\alpha$ using Hi-res events only. [Right] The same plot using Mid-res (primary) events only. . . . .	48
6.7	XRS measurement of Cu K $\alpha$ emission line on a logarithmic scale compared to a simple Gaussian fit. . . . .	49
7.1	The four XIS detectors before installation onto <i>Astro-E2</i> . . . . .	51
7.2	One XIS instrument. Each XIS consists of a single CCD chip with $1024 \times 1024$ X-ray sensitive cells, each $24 \mu\text{m}$ square. <i>Astro-E2</i> contains four CCD sensors (XIS-S0 to S3), two AE/TCUs (AE/TCE01 and AE/TCE23), two PPUs (PPU01 and PPU23), and one MPU. AE/TCU01 and PPU01 service XIS-S0 and XIS-S1, while AE/TCE23 and PPU23 service XIS-S2 and XIS-S3. Two of the XIS CCDs will be front-illuminated (FI) and two will be back-illuminated (BI). . . . .	53
7.3	Time sequence of the exposure, frame-store transfer, CCD readout, and data transfer to the pixel RAM in PPU is shown (1) in normal mode without options, (2) in normal mode with Burst option, and (3) in normal mode with Window option. In this example, the 1/4 Window option is assumed. . . . .	57
7.4	Information sent to the telemetry is shown for $5 \times 5$ , $3 \times 3$ , and $2 \times 2$ modes. 1-bit information means whether or not the PH of the pixel exceeds the outer split threshold. In $2 \times 2$ mode, the central 4 pixels are selected to include the second and the third (or fourth) highest pixels among the 5 pixels in a cross centered at the event center. . . . .	59
7.5	Definition of the grades in the P-Sum/timing mode. Total pulse height and the grade of the event are output to the telemetry. Note that the grades are defined referring to the direction of the serial transfer, so the central pixel of a grade 1 event has the <i>larger</i> RAWX value, while the opposite is true for a grade 2 event. . . . .	59

8.1	The Hard X-ray Detector before installation. . . . .	62
8.2	Schematic picture of the HXD instrument, which consists of two types of detectors: the PIN diodes located in the front of the GSO scintillator, and the scintillator itself.	63
8.3	The HXD background, including both intrinsic and cosmic components for both the PIN and GSO detectors. . . . .	64
8.4	[Left] The sensitivity of the HXD to continuum emission, taking into account the expected background. [Right] Same, for line emission. . . . .	65

# List of Tables

2.1	Overview of <i>Astro-E2</i> capabilities . . . . .	6
2.2	Error Budgets of Scientific Instrument Calibrations . . . . .	17
3.1	The preliminary schedule for <i>Astro-E2</i> and percentage of time for each group of observers. The ESA time is in parentheses as it is part of the Japanese allotment. . .	19
5.1	Telescope Dimensions and Parameters of XRT . . . . .	33
5.2	Design Parameters for Pre-collimator . . . . .	36
6.1	Filter Element and Calibration Source on Filter Wheel . . . . .	45
6.2	The energy-dependence of XRS pixels; $1\sigma$ measurement uncertainties are 0.3 eV. Note that the two unusual pixels are on the perimeter of the array and should have minimal impact on most observations. . . . .	49



# Chapter 1

## Introduction

*Astro-E2* is the fifth in the series of Japanese astronomy satellites devoted to observations of celestial X-ray sources, following the highly successful *Hakucho*, *Tenma*, *Ginga* and *ASCA* satellites. Like *ASCA*, *Astro-E2* is a joint Japanese-US mission, developed by the Institute of Space and Astronautical Science (part of the Japan Aerospace Exploration Agency, ISAS/JAXA) in collaboration with the National Aeronautics and Space Administration's Goddard Space Flight Center (NASA/GSFC) and many other institutions. Launch is planned for February 2005 using the Japanese M-V launch vehicle. *Astro-E2* has excellent X-ray sensitivity, with high throughput over a broad-band energy range of 0.2 to 600 keV. This broad bandpass, combined with high resolution spectroscopy capabilities, makes *Astro-E2* a unique tool capable of addressing a variety of outstanding problems in astrophysics, involving the origins of elements and structures in the Universe as well as the evolution and dynamics of these structures.

Guest observing time on *Astro-E2* will be awarded on a competitive basis. The overall purpose of this document is to aid potential users of *Astro-E2* in proposing for time during the Guest Observer (GO) phase of the mission. In particular, upon reading this document, the proposer should be able to determine whether or not *Astro-E2* is best suited to conduct the investigation in question. This should be demonstrated in the proposal, preferably using simulations of the proposed observations. All proposals should clearly answer the following four questions:

1. Is *Astro-E2* capable of the proposed observation?
2. Is it the best available instrument for the investigation?
3. When can *Astro-E2* observe a given source?
4. How much exposure time is required to meet the scientific goals?

In addition, since *Astro-E2*'s X-Ray Spectrometer (XRS) has a limited lifetime, priority will be given to science that requires the XRS. More information on the XRS and the *Astro-E2* mission in general can be found in Chapter 2, which briefly describes *Astro-E2*'s instruments, including their capabilities and operational constraints.

Chapter 3 covers how the satellite time will be allocated. This includes the data rights and available time for both the Science Working Group (SWG) and GOs, as well as policies regarding Targets of Opportunity (TOOs). In addition, observational constraints due to the orbit, sun angle, and the pointing accuracy are described. Finally, the proposal process is reviewed, including how to submit a proposal, how they will be evaluated, and how observations will be scheduled, performed, and the results disseminated. US proposers should note especially the NASA requirements regarding the relevance of the proposed science to NASA's mission.

Chapter 4 explains how to write a strong proposal, including a summary of what constraints must be met, and what must be included in the proposal. It is expected that most proposals will be for targets which have been observed previously in X-rays, and so existing X-ray data can be used to estimate the likely *Astro-E2* count rates and determine if any filters are required. Simulation tools, including **XSPEC**, **PIMMS**, and **xrssim**, can help make these estimates and are covered in detail with examples.

The last four chapters describe the telescope and instruments on *Astro-E2*. Chapter 5 covers the five X-ray Telescopes (XRTs) on *Astro-E2*. Chapter 6 describes the X-Ray Spectrometer (XRS), the prime instrument on *Astro-E2* which will provide 6–7 eV resolution between 0.3–12 keV. Chapter 7 reviews the X-ray Imaging Spectrometers (XISs), four CCDs with moderate spectral resolution and a large field of view. Chapter 8 explains the operation of the Hard X-ray Detector (HXD), which extends the high energy bandpass of *Astro-E2* to 600 keV.

**Disclaimer:**

This document was prepared using the best current knowledge of the *Astro-E2* satellite by the *Astro-E2* teams at ISAS/JAXA and NASA/GSFC as of May 2004. It is possible that information contained in this document may contain inadvertent errors or omissions. We welcome suggestions for corrections or clarifications. Revisions of this document will be available on the *Astro-E2* Web sites listed in Appendix C.

## Chapter 2

# Mission Description

This chapter is a brief introduction to the satellite and its instruments, and is intended as a simplified guide for the proposer. Reading it thoroughly should provide the reader with the necessary information to understand the capabilities of the instruments at a level sufficient to prepare the feasibility section of an *Astro-E2* proposal.

*Astro-E2* is scheduled to launch from the Uchinoura Space Center (USC) on a Japanese M-V rocket in February 2005. After launch, the satellite will undergo an initial checkout phase lasting approximately 4 weeks, including instrument turn-on and initial calibration. Science observations will begin immediately after this initial phase and will focus on using the XRS for as long as the cryogenic system lasts, which is expected to be  $\sim 2.5$  years.

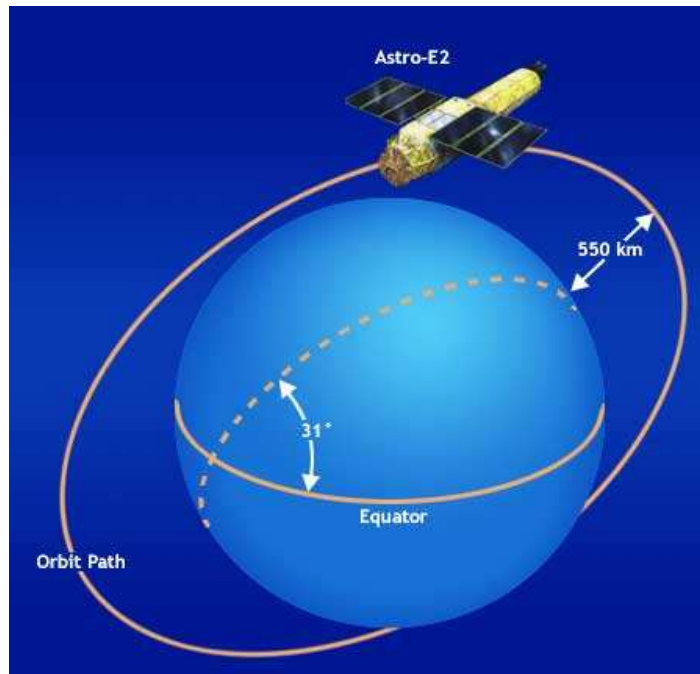


Figure 2.1: The 96 minute *Astro-E2* orbit.

*Astro-E2* is in many ways similar to ASCA in terms of its orbit, the pointing and tracking capabilities of the spacecraft, and uses the same station (USC) for uplink and downlink. Therefore, the operational constraints for *Astro-E2* are also similar to those of ASCA. *Astro-E2* will be placed in a near-Earth orbit, with inclination of 31 degrees, orbit altitude of roughly 550 km, and orbital

period of about 96 minutes. The maximum slew rate of the spacecraft is 12 degrees/min, and settling to the final attitude will take about 10 minutes. The normal mode of operations will have the spacecraft pointing in a single direction for at least 1/4 day (10 ksec; but see “raster-scanning” below). With this constraint, most targets will be occulted by the Earth for about one third of each orbit, but some objects near the orbital poles can be observed nearly continuously. The current projection is that the observing efficiency of the satellite will be about 45%.

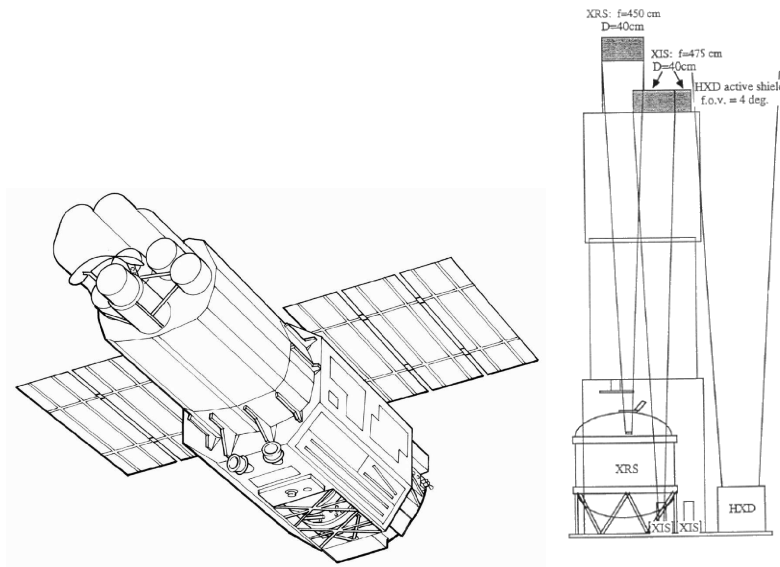


Figure 2.2: [Left] Schematic picture of the bottom of the *Astro-E2* satellite. [Right] A side view of the instrument and telescopes on *Astro-E2*.

## 2.1 A Brief Introduction to *Astro-E2*

The scientific payload of *Astro-E2* (Fig. 2.2) consists of three types of co-aligned scientific instruments. High-resolution X-ray spectroscopy will be carried out with the X-ray Spectrometer (XRS). The XRS is an X-ray calorimeter array capable of precisely measuring the energy of an incoming X-ray photon (between 0.3-12 keV) by detecting the temperature rise resulting from the absorption of the photon. This instrument uses consumable cryogenes, and it is expected that its lifetime will be  $\sim 2.5$  years. The observatory also features four X-ray sensitive imaging CCD cameras (X-ray Imaging Spectrometers, or XISs), two front-illuminated (FI; energy range 0.4-12 keV) and two back-illuminated (BI; energy range 0.2-12 keV), capable of moderate energy resolution. The XRS and each XIS are located in the focal planes of five dedicated X-ray telescopes. The third type of instrument is the non-imaging, collimated Hard X-ray Detector (HXD), which extends the bandpass of the observatory to much higher energies with its 10–600 keV bandpass.

All of the instruments on *Astro-E2* operate simultaneously. Each of the five co-aligned XRTs features an X-ray mirror with an angular resolution (expressed as Half-Power Diameter, or HPD) of  $\sim 2'$  (cf. Fig. 2.6). Figure 2.3 shows the total effective area of the XRS+XRT, which includes features due to the elemental composition of the XRS and XRT. K-shell absorption edges from the oxygen (0.54 keV), aluminum (1.56 keV), and nickel (8.33 keV) in the blocking filters can be seen, as well as a number of weak M-shell features between 2–3 keV arising from the gold in the XRT. Of course, similar features exist in the total effective area of the XIS+XRT (for both FI and BI

S/C	Orbit Altitude	550 km
	Orbital Period	96 minutes
	Observing Efficiency	$\sim 45\%$
XRT	Focal length	4.75 m (XRT-I), 4.50 m (XRT-S)
	Field of View	17' at 1.5 keV 13' at 8 keV
	Plate scale	0.724 arcmin/mm (XRT-I), 0.764 arcmin/mm (XRT-S)
	Effective Area	440 cm <sup>2</sup> at 1.5 keV 250 cm <sup>2</sup> at 8 keV
	Angular Resolution	2' (HPD)
XRS	Field of View	$2.9' \times 2.9'$
	Bandpass	0.3–12 keV
	Pixel Grid	$6 \times 6$ ; 30 active
	Pixel size	0.624 mm $\times$ 0.624 mm
	Pixel spacing	0.64 mm $\times$ 0.64 mm
	Energy Resolution	6.5 eV (FWHM) at 6 keV
	Lifetime	$\sim 2.5$ years
	Effective Area	190 cm <sup>2</sup> at 1.5 keV 100 cm <sup>2</sup> at 8 keV
	(incl. XRT-S)	
	Absolute Line Centroiding	$\lesssim 2$ eV
	Absolute Time Resolution	100 $\mu$ s
	Average Telemetry limit	5 counts/s/pixel
	Background rate	$\sim 2$ counts/pixel/day
XIS	Field of View	$18' \times 18'$
	Bandpass	0.2–12 keV
	Pixel grid	1024 $\times$ 1024
	Pixel size	24 $\mu$ m $\times$ 24 $\mu$ m
	Energy Resolution	$\sim 130$ eV at 6 keV
	Effective Area	340 cm <sup>2</sup> (FI), 390 cm <sup>2</sup> (BI) at 1.5 keV 150 cm <sup>2</sup> (FI), 100 cm <sup>2</sup> (BI) at 8 keV
	(incl XRT-I)	
	Time Resolution	8 s (Normal mode), 7.8 ms (P-Sum mode)
HXD	Field of View	$4.5^\circ \times 4.5^\circ$ ( $\gtrsim 100$ keV)
	Field of View	$34' \times 34'$ ( $\lesssim 100$ keV)
	Bandpass	10 – 600 keV
	– PIN	10 – 60 keV
	– GSO	30 – 600 keV
	Energy Resolution (PIN)	$\sim 3.0$ keV (FWHM)
	Energy Resolution (GSO)	$7.6/\sqrt{E_{MeV}}$ % (FWHM)
	Time Resolution	61 $\mu$ s

Table 2.1: Overview of *Astro-E2* capabilities

CCDs), seen in Figure 2.4, but the energy resolution of the XRS makes these more significant if they coincide with an astronomical feature.

The XRS includes a  $6 \times 6$  array of individual detector elements (pixels), of which 30 are active<sup>1</sup>, arranged as illustrated on Fig. 2.5. There is also one calibration pixel used for gain tracking, set away from the main array and illuminated by a collimated <sup>55</sup>Fe source (see § 6.2). As of this writing, the final assembly of the XRT for the XRS (the XRT-S) is in progress and its HPD has

<sup>1</sup>One of the original 31 imaging array pixels (pixel 3) is inoperable as of March 2004.

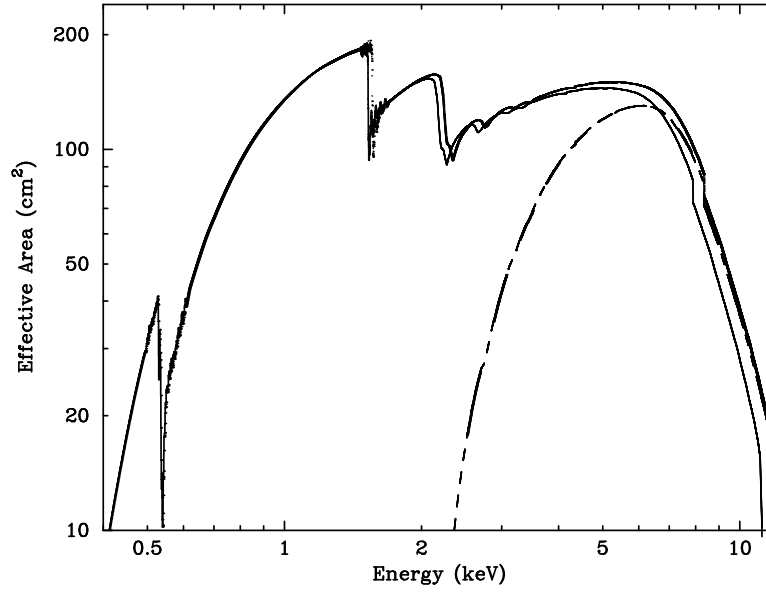


Figure 2.3: Effective area as a function of photon energy of the combined XRT + XRS system, for all 30 pixels. The upper (solid) curve shows the effective area with the open position of the filter wheel; the lower (dashed) curve shows it with the 300  $\mu\text{m}$  Be filter.

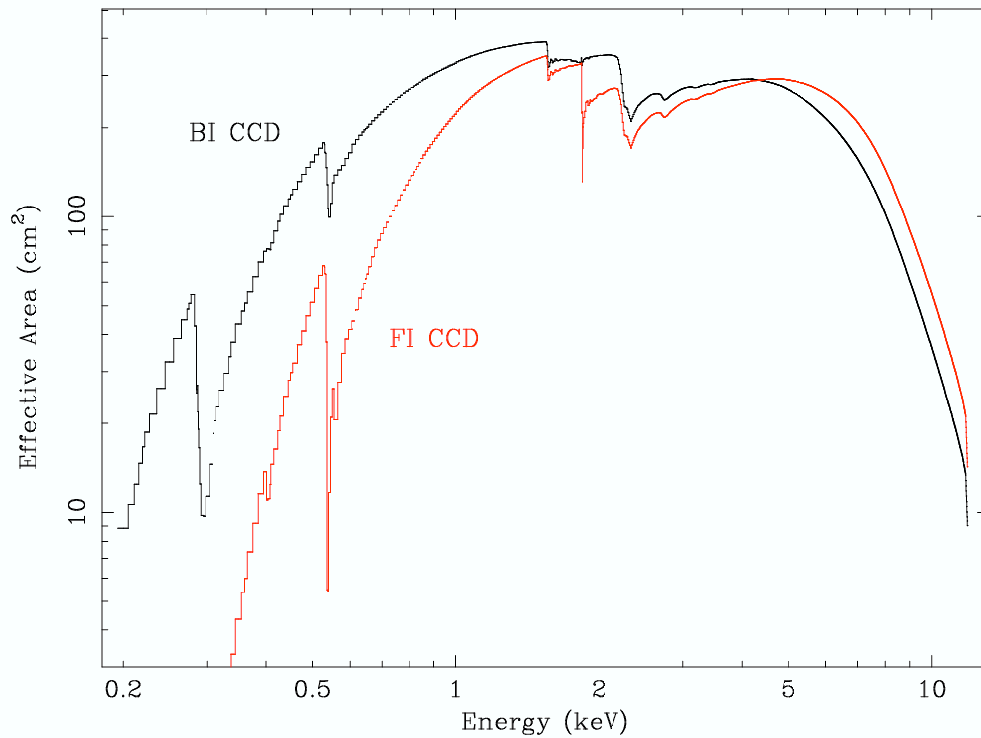


Figure 2.4: XIS Effective area of one XRT + XIS system, for both the FI and BI chips.

not yet been measured, but it is expected to be between 1.6 and 2.0 arcminutes. Gravity will also slightly distort the ground-based HPD measurements (cf. Fig. 2.6) for all the XRTs in as-yet unknown ways. If the HPD is  $2'$  (a conservative estimate), an on-axis point source will put  $\sim 64\%$  of its flux onto the XRS array, which is  $\sim 2.9' \times 2.9'$  on the sky.

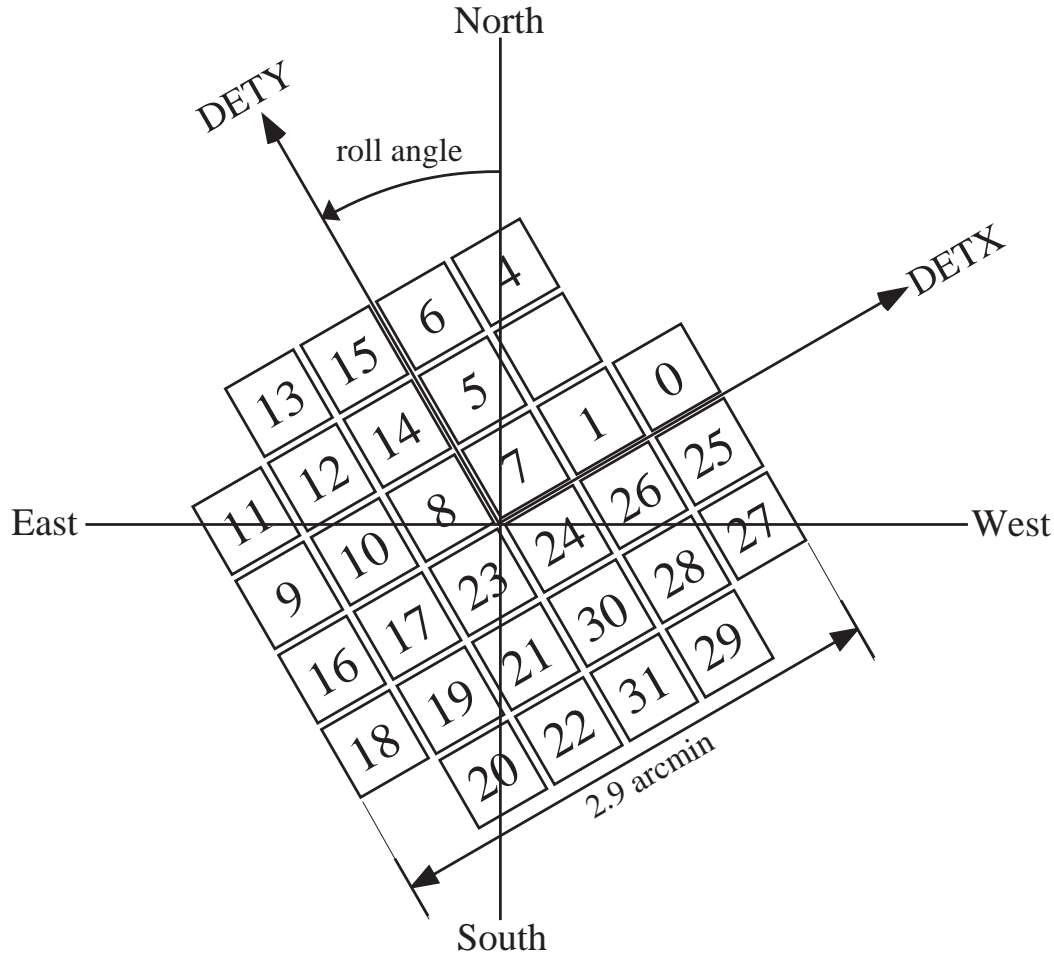


Figure 2.5: The XRS calorimeter array, showing the layout of the pixels. Each pixel has a dimension of  $0.64 \text{ mm} \times 0.64 \text{ mm}$ , corresponding to a sky projection of  $\sim 0.49' \times 0.49'$ ; the entire X-ray sensitive portion of the array projects a solid angle of  $\sim 2.9' \times 2.9'$  on the sky. The pixel numbers are determined by the geometry of the detector assembly; the marked but unlabeled pixel is inactive as of March 2004. In this Figure, the array is shown projected onto the sky.

The four XISs (cf. Fig. 7.2) are true imagers, and have a larger field of view ( $\sim 18' \times 18'$ ), but significantly lower spectral resolution than the XRS ( $\sim 130 \text{ eV}$  at  $6 \text{ keV}$ ; see Fig. 2.9). The XISs do not require cryogenic cooling, and should continue to operate well after the cryogenic system has been exhausted.

The HXD (cf. Fig. 8.1) is a non-imaging instrument with an effective area of  $\sim 300 \text{ cm}^2$ , featuring a compound-eye configuration and an extremely low background. It dramatically extends the bandpass of the mission with its nominal sensitivity over the  $10 - 600 \text{ keV}$  band (cf. Fig. 2.7). The HXD consists of two types of sensors:  $2 \text{ mm}$  thick silicon PIN diodes sensitive over  $10 - 60 \text{ keV}$ , and GSO crystal scintillators placed behind the PIN diodes covering  $30 - 600 \text{ keV}$ . The HXD field of view is actively collimated to  $4.5^\circ \times 4.5^\circ$  by the well-shaped BGO scintillators, which, in combination with the GSO scintillators, are arranged in the so-called phoswich configuration. At energies below  $\sim 100 \text{ keV}$ , an additional passive collimation further reduces the field of view to  $34' \times 34'$ . The energy resolution is  $\sim 3.0 \text{ keV}$  (FWHM) for the PIN diodes, and  $7.6/\sqrt{E} \%$  (FWHM) for the scintillators (where  $E$  is energy in MeV). The HXD time resolution for both sensors is  $61 \mu\text{s}$ . While the HXD is intended mainly to explore the faintest hard X-ray sources, it can also tolerate very bright sources up to  $\sim 10 \text{ Crab}$ .

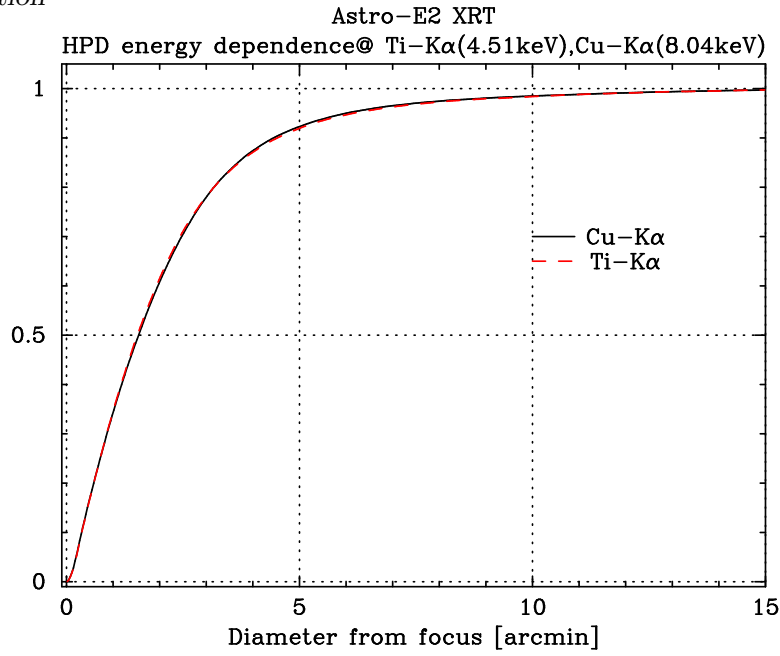


Figure 2.6: The Encircled Energy Function (EEF) showing the fractional energy within a given radius for one quadrant of the XRT-I telescopes on *Astro-E2* at 4.5 and 8.0 keV. The XRT-S EEF is expected to be similar.

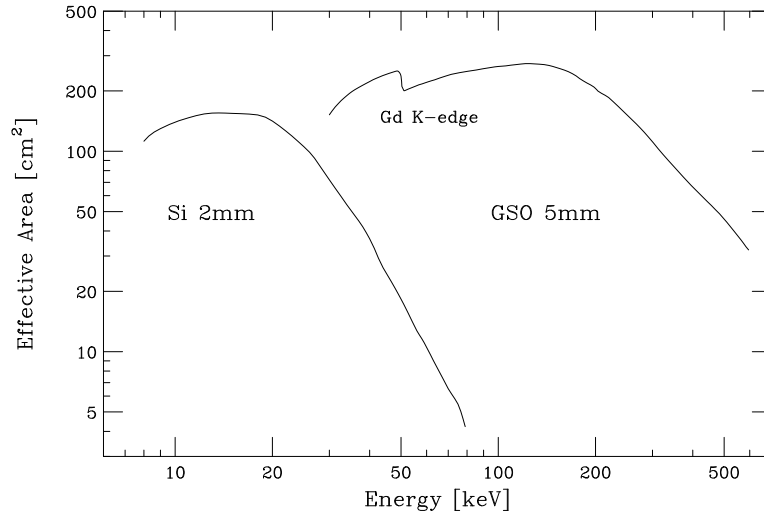


Figure 2.7: Total effective area of the HXD detectors, PIN and GSO, as a function of energy.

Although this document emphasizes the XRS, each observation will contain data from all instruments since they are co-aligned and operate simultaneously.

## 2.2 Operational Constraints of *Astro-E2*

### 2.2.1 Raster-scanning

While a substantial change of the spacecraft attitude (more than a few degrees) is time-consuming, small offsets can be made efficiently. Such offsets would require that no new stars need to be acquired by the star trackers, and thus are limited to  $\sim 1$  to  $2^\circ$ . This is particularly useful for



studies of extended sources larger than a few arcmin with the XRS (which is a unique tool for high resolution spectroscopy of extended sources). The minimum total time is still 10 ksec, and each point in the raster scan must be observed for at least 3 ksec. Raster-scanning observations should be specified on the RPS form, with the details to be entered in the “remarks” field. If the raster-scan pattern is complex or unusual, PIs are encouraged to contact the *Astro-E2* team at ISAS/JAXA or the NASA *Astro-E2* GOF for assistance before submitting a proposal.

### 2.2.2 Cooling system constraints

Another operational constraint for the XRS arises from the operation of the refrigerator for the XRS. To maintain the base temperature of the array at 60 mK, the instrument uses an Adiabatic Demagnetization Refrigerator (ADR), which has to be recharged periodically, about once every day. The recharge will take about 65 minutes. The current plan is to recharge when the spacecraft is slewing, or when a target of an observation is in the Earth’s shadow, but this may change as a result of the on-orbit verification of the satellite.

### 2.2.3 Telemetry rates

Astro-E2 carries a 6 Gbit data recorder. Data will be downlinked to USC at a rate of 4 Mbps for a total of 2 Gbits per pass, up to 5 times a day. This allows a maximum of 10 Gbits of data to be obtained per day, but fewer passes may be available to Astro-E2 as it will share the use of USC ground station with other ISAS satellites<sup>2</sup>. Data can be recorded at 4 different rates: Super-High (524 kbps), High (262 kbps), Medium (131 kbps), and Low (33 kbps). The recording rate will be changed frequently throughout an observation, according to a sequence that will be determined by the operations team at ISAS. This is to optimize the selection of the data rates and the usage of the data recorder, taking into account the expected count rates supplied by the proposers. Thus an accurate estimation of the count rates is important for the optimization of the mission operation. We emphasize that proposers cannot arbitrarily choose the data recording rate.

We expect that on-source data will usually be recorded at High (during contact orbits, during which the satellite passes over USC) or Medium (during remote orbits, without USC passes) data rate. The Low rate will be used mostly for times of Earth occultations and SAA passages, as it is probable that the background rates in the XIS and HXD exceed their telemetry allocation limit at Low data rate. The XRS telemetry allocation is a constant 160 ct/s regardless of the total data recording rate, while the telemetry limits for the XIS are presented in Chapter 7. Unless otherwise specified, the XIS data mode will be chosen for each data recording rate used to prevent telemetry saturation, based on the count rate supplied by the proposer.

## 2.3 Features and Capabilities of the XRS

The truly new and unique aspect of the *Astro-E2* mission will be the availability of the XRS to obtain high-resolution X-ray spectra of a wide variety of celestial sources. The XRS differs from a grating spectrometer in two important ways. First, it is a non-dispersive detector so it can measure high-resolution spectra of extended sources as well as point source. Secondly, since the XRS energy resolution is nearly constant the resolving power  $E/\Delta E$  *increases* with energy rather than decreasing.

---

<sup>2</sup>Unlike ASCA, NASA DSN stations will not be used, since a 4 Mbps down-link is not possible at DSN stations.

### 2.3.1 Design and Performance

The XRS absorbs the energy of each photon  $E_{\text{ph}}$  in a pixel (one of the 30 active elements of the XRS detector), which is then converted into heat (see Fig. 6.3). This results in a change of the temperature of the pixel  $\Delta T$ , which is roughly  $\Delta T = E_{\text{ph}}/C$ , where  $C$  is the heat capacity of the pixel. As discussed in Chapter 6, maintaining the sensitivity of the detector requires keeping its operating temperature to a minimum; at the operating temperature, the typical  $C$  of all constituents of an XRS pixel is  $\sim 10^{-6}$  erg/K. With this, a 1 keV photon with  $E_{\text{ph}}$  of  $1.6 \times 10^{-9}$  erg produces  $\Delta T$  of  $\sim 1.6$  mK. The energy resolution of the XRS is thus related to the accuracy with which the above  $\Delta T$  can be measured. The pre-launch energy resolution  $\Delta E$  of the flight detector pixels is 6.5 eV (FWHM) at 6 keV. With adequate counts, the centroid energy of monochromatic photons can be determined to  $\lesssim 2$  eV; this is likely to be limited by the systematics of the instrument, and specifically, the temperature stability of the cooling system, but should be aided by the on-board calibration sources (cf. §6.2). While at low energies, X-ray spectrometers such as the LETG on *Chandra* and RGS on *XMM-Newton* have better energy resolution, in the crucial Fe K region (6 - 7 keV), the energy resolution of the XRS is superior (by  $\sim 5\times$ ) to the *Chandra* HETG (see Figs. 2.8 & 2.9). **Note that there are essentially no user-specified parameters for the XRS, except for the setting of the Filter Wheel (cf. §6.2), which is external to the instrument itself.**

### 2.3.2 Unique attributes

While both *XMM-Newton* and *Chandra* have high resolution spectroscopy capabilities, there are several aspects where the *Astro-E2* XRS will provide unique data. First, both *XMM-Newton* and *Chandra* rely on dispersive spectroscopy using diffraction gratings, and unambiguous spectra can be obtained only for point or point-like sources with angular extent (or small, well-defined structure) which is smaller than or comparable to the PSF of the telescope. There are many classes of diffuse celestial X-ray emitters (such as supernova remnants and clusters of galaxies) with a larger angular size, and these simply *cannot* be effectively studied with gratings. The XRS, on the other hand, is a non-dispersive instrument, and *can* study these sources and so it will open a new, unique window on the X-ray Universe. Secondly, the XRS has superior resolution at high energies compared to existing X-ray telescopes. The *XMM-Newton* gratings have essentially no effective area above  $\sim 2$  keV and above  $\sim 3$  keV, the energy resolution of the *Chandra* gratings is inferior to that of the XRS. Therefore, the high resolution spectroscopy with the XRS lends itself well towards answering such questions as:

- What is the composition and temperature of hot cosmic plasma (as inferred from the relative intensities of emission lines)?
- What is the velocity field of line-emitting material (as inferred from Doppler shifts of emission lines such as Fe K $\alpha$ )?
- What is the nature and kinematics of hot, tenuous absorbing material in the line of sight to an astrophysical source (from profiles of absorption lines)?

### 2.3.3 Characteristics

By comparison with some other instruments (such as proportional counters) the time to detect and measure the energy of an X-ray photon with the XRS is relatively long—on the order of 100 milliseconds (although the arrival time can be measured to a few tens of microseconds). As a result, the throughput of events whose energy can be determined with high resolution will drop as the

counting rate increases beyond  $\sim 3.5$  photons  $\text{s}^{-1}$  per pixel. The on-board signal processing (see §6.3) distinguishes “high resolution” events (entirely uncontaminated by temporally neighboring events), “medium resolution” events (slightly contaminated events, with  $\Delta E_{\text{mid}} \sim 1.2 \times \Delta E_{\text{hi}}$ ), and “low resolution” events, with  $\Delta E_{\text{low}} \sim 5 \times \Delta E_{\text{hi}}$ . **Note that this limitation affects each pixel independently, since all the channels are processed separately: even when the count rate on one pixel may be excessive, another pixel, receiving a lower photon rate, may be unaffected.** As a result, considering the point spread function of the XRT, it is possible that the XRS pixels close to the nominal source position may be strongly affected, while the pixels farther away from the peak may yield mostly “high resolution” and “medium resolution” events. The relative fractions and event rates are illustrated in Figures. 2.10 & 2.11, which assume a Poisson distribution of arrival times between events from a point source.

The relative fraction of event types will also be affected by cosmic rays impinging on the XRS. Cosmic rays can heat the entire array, leading to false events on every pixel. The rate will have to be measured on orbit, but a conservative estimate is  $\sim 0.5$  count/s. The effect of these cosmic rays will be to decrease the number of high resolution events, as it puts a lower floor on the count rate in any pixel even for faint sources. Since the Hi-res record length is 0.16 s, the fraction of time affected by cosmic rays is  $0.5 \text{ counts/s} \times 0.16 \text{ s} = 8\%$ . In earlier X-ray detectors such as CCDs or proportional counters, this would be considered unusable “deadtime.” In the XRS, cosmic rays do not cause true deadtime, but instead migrate events toward lower resolution.

For the studies of very bright sources, there is a filter wheel located in the X-ray beam between the mirror and the detector, capable of reducing the photon flux incident on the detector. This filter wheel (see § 6.2) has three different filter elements; OPEN, BE, and ND, with optional  $^{55}\text{Fe}$  calibration sources that illuminate the detector. BE is a soft X-ray cutoff filter containing  $300\mu\text{m}$  of beryllium; its effect can be seen in Figure 2.3. ND is a neutral density filter that is partially opaque with energy-independent transmission of 10%. It is important to stress that except for the Crab nebula, there are no known extended sources such as clusters of galaxies or supernova remnants that would cause enough pulse pileup to warrant the use of any filters in the filter wheel. We thus expect that the filter wheel should be necessary only for bright Galactic binary sources (with flux in excess of  $\sim 50$  milliCrab).

The XRS has a relatively modest field of view, covering only  $\sim 2.9' \times 2.9'$ . For sources with larger angular extent, multiple pointings may be required, increasing the integration time needed to map a large diffuse region. In addition, for point sources, the energy resolution of the *XMM-Newton* RGS or *Chandra* LETG is superior below  $\sim 2$  keV.

### 2.3.4 Summary

The XRS excels for observations such as:

- Spectroscopy at energies  $E > 2$  keV where the highest spectral resolution is required, and in particular, in the Fe K line region.
- All high spectral resolution studies of extended sources (modulo the surface brightness; very faint and/or large sources may require inordinate integration times in multiple pointings to take advantage of the energy resolution of the XRS, and are better suited to study with instruments subtending a larger solid angle on the sky).

The XRS is less appropriate for:

- Studies requiring primarily high spatial resolution: the resolution of *Chandra* is about 100 times better, while the *XMM-Newton* is about 10 times better.

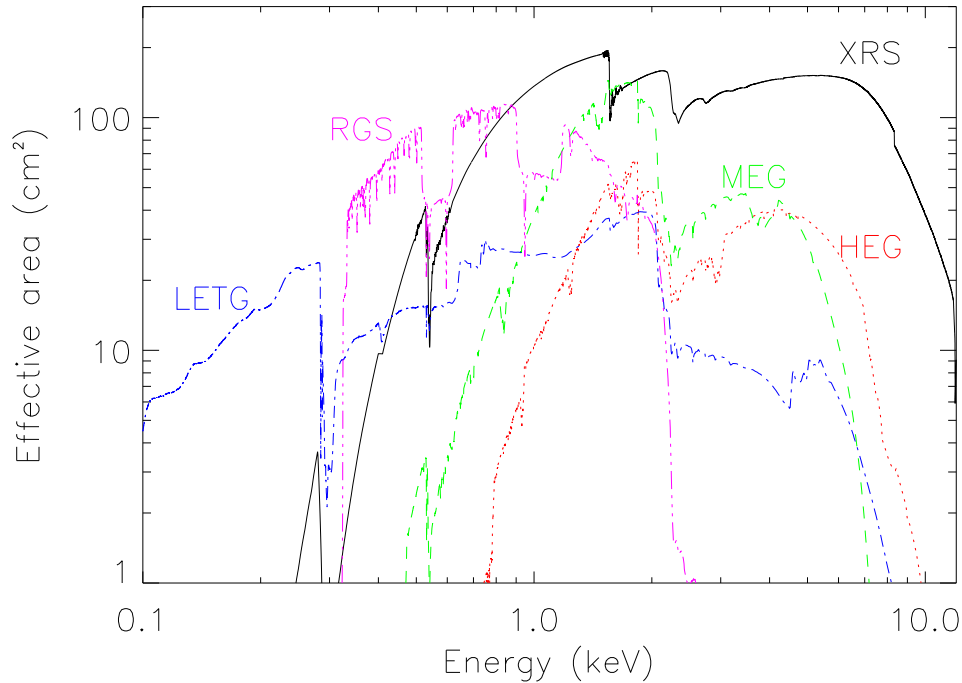


Figure 2.8: Comparison of the effective area of the XRS against *XMM-Newton*'s RGSs and *Chandra*'s grating instruments.

- Studies of very large ( $> \text{a degree}$ ), diffuse objects with low surface brightness: collecting a sufficient number of photons for a meaningful study may require unreasonable integration times.
- Soft X-ray spectroscopy of point sources at  $E < 1.0 \text{ keV}$ . The *XMM-Newton* RGSs and *Chandra* LETG are more appropriate, as the *Astro-E2* XRS has worse spectral resolution and a lower effective area than these.
- Spectroscopy of *broad* ( $> 200 \text{ eV}$ ) spectral features. For this, the *XMM-Newton* EPIC and *Chandra* ACIS detectors are superior, as they provide greater collecting area.
- Rapid variability studies on millisecond time scales: for bright sources, the counting rate limitation requires the use of filters, resulting in the loss of counts. For such studies, the RXTE or *XMM-Newton* may be more appropriate. Nonetheless, the XRS does have good time resolution, and may be an excellent instrument for temporally resolved spectroscopy (pulsars).

## 2.4 Calibration Plan

Observations for scientific instrument calibration are to start  $\sim 3$  weeks after the launch. Those to calibrate the functions essential for achieving the mission goals have the highest priorities, and hence, all of them will be carried out by the end of Phase-1A. After that, long term variation of the

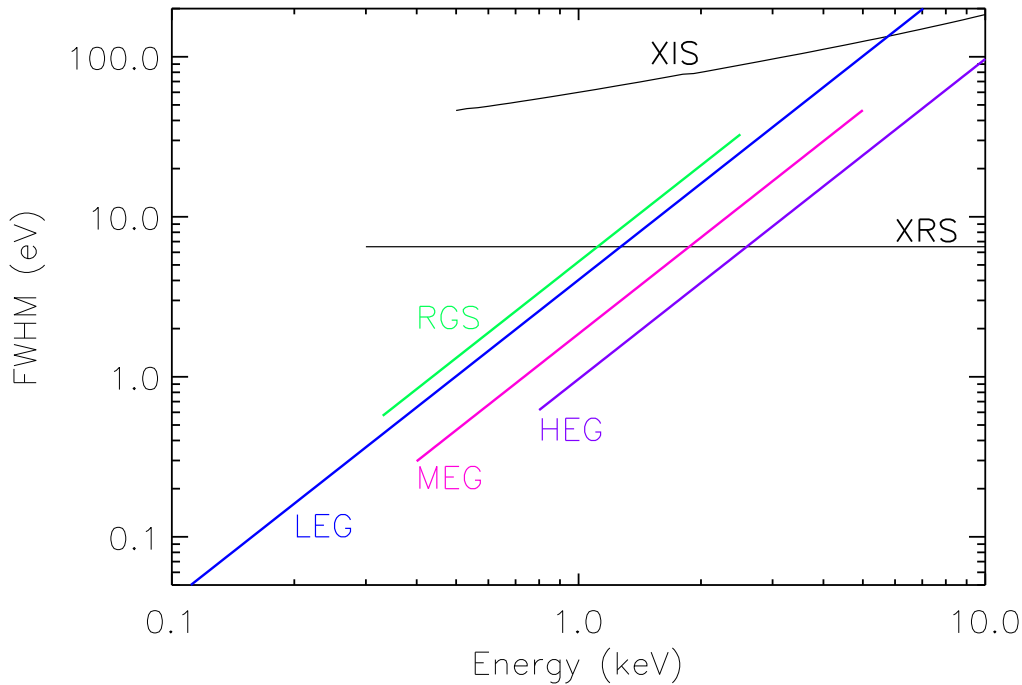


Figure 2.9: Comparison of the energy resolution of the XRS and XIS against *XMM-Newton*'s RGSs and *Chandra*'s grating instruments.

functions will have been monitored every half a year or so. The list of all the calibration targets during Phase-1A can be found on the *Astro-E2* websites listed in Appendix C.

Table 2.2 summarizes the calibration items of all scientific instruments and their expected accuracy. Note that the values listed are those required from the scientific purpose and ultimate goals which are possible to be realized on the basis of the instrument design, and are not the results of real measurements. Since the scientific instruments of *Astro-E2* are very sensitive to the environment, it scarcely makes sense to list the values of the ground-based calibration. We will add a column to the table representing the results from inflight calibration until the start of AO-1 observations (2005 September). Please regard the current values in the table as providing rough idea on the order of calibration accuracy in orbit.

*Note from the XIS team* — All the values about the XIS in the table are estimated from the very preliminary results of the ground calibrations of the FI sensors. The goals of the BI sensor calibrations should be almost the same. Furthermore, since the XIS will suffer the radiation damage, it is very difficult to predict how the characteristics of the XIS will change even in the first half year after the launch. The XIS team will update these values as ground or flight calibrations progress.

*Note from the HXD team* — It is very difficult to estimate the background levels on the ground. The HXD team will continue study on them, and will prepare some documents on HXD BGD estimation until the start of AO-1 observations.

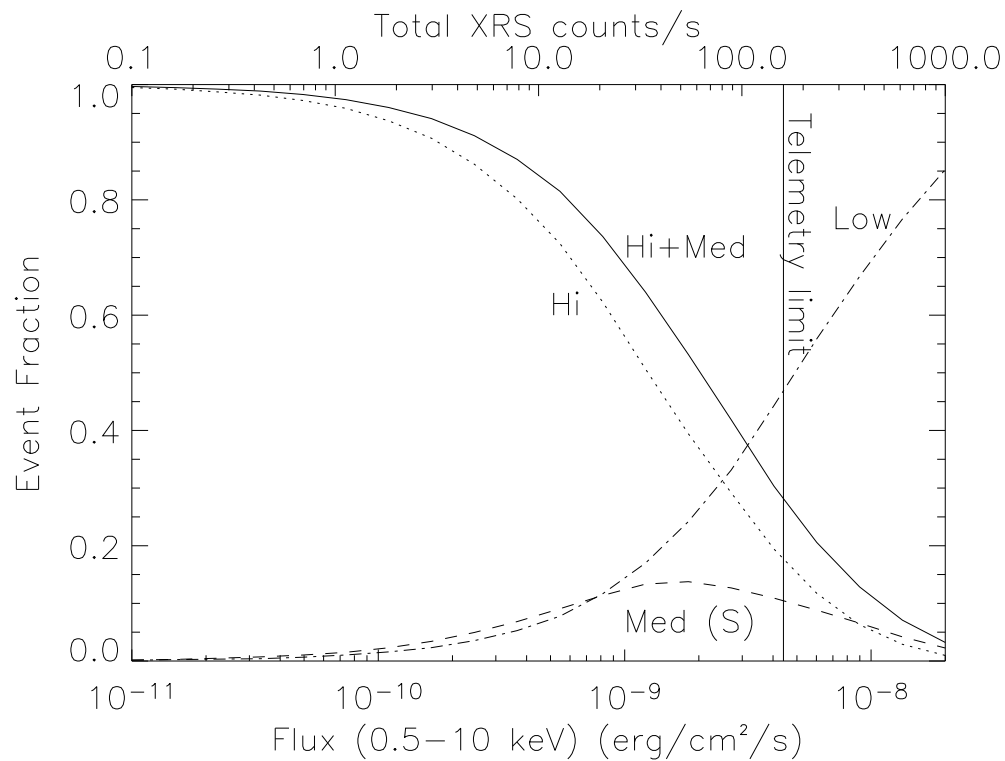


Figure 2.10: The fraction of X-ray photons processed into the “low-res,” “mid-res,” and “high-res” events by the XRS for a point source with a power-law spectrum ( $\Gamma = 2.0$ ) between 0.5-10 keV. The mid-res counts are separated into primary events, which have nearly the same resolution as the hi-res events, and secondary events (marked with an “S”) which have somewhat lower resolution. Secondary events occur when the event time is within 142 ms of an earlier pulse (see also Fig. 6.5).

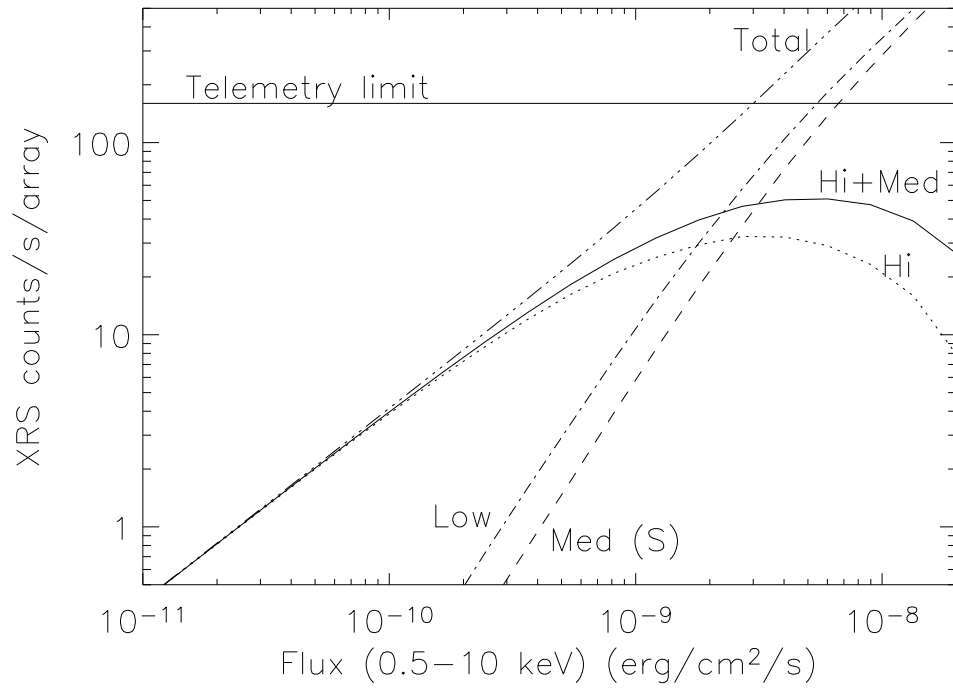


Figure 2.11: Similar to Fig. 2.10, but showing the counting rate as a function of source flux. This figure includes the effects of the point-spread function of the mirror.

Table 2.2: Error Budgets of Scientific Instrument Calibrations

S/S	Calibration Item	Requirement	Goal
XRT	absolute effective area (2–10 keV in XIS) . . . . .	5%	5%
	XRT-S to XRT-I effective area cross-calibration	5%	5%
	vignetting for all XIS f.o.v. . . . .	2%	2%
	on-axis PSF (for all integration radii from 1'–6')	1%	1%
	off-axis PSF (as on-axis but for all XIS f.o.v.)..	2%	2%
	optical axis position in XRS . . . . .	< 1'	< 1'
	optical axis position in XIS . . . . .	< 0.2'	< 0.2'
XRS	energy scale . . . . .	2 eV	1 eV
	line spread function (FWHM) . . . . .	1 eV	1 eV
	effective area . . . . .	10% <sup>a</sup>	5% <sup>a</sup>
	absolute timing . . . . .	300 $\mu$ s	100 $\mu$ s
	relative timing . . . . .	80 $\mu$ s	10 $\mu$ s
XIS	Q.E. at 10 keV . . . . .	5% <sup>b</sup>	5% <sup>b</sup>
	energy scale . . . . .	0.1% <sup>b</sup>	0.1% <sup>b</sup>
	resolution (FWHM) at 5.9 keV . . . . .	1% <sup>b</sup>	1% <sup>b</sup>
	Q.E. vs position . . . . .	5% <sup>b</sup>	5% <sup>b</sup>
	OBF integrity . . . . .	broken/unbroken	broken/unbroken
HXD	absolute effective area . . . . .	20%	5%
	relative effective area . . . . .	10%	5%
	vignetting . . . . .	10%	5%
	background modelling <sup>c</sup> . . . . .	$\sim 10\%$ <sup>c</sup>	5% <sup>c</sup>
	absolute timing . . . . .	300 $\mu$ s	100 $\mu$ s
	relative timing . . . . .	$10^{-8}$	$10^{-10}$
	GBST absolute timing . . . . .	100 ms	15 ms

*Note* . . . All the values quoted are preliminary.

a: Including the errors associated with the XRT.

b: All values of the XIS are based on the ground calibration data and very preliminary. See the text in more detail.

c: Study continues. The HXD team will prepare some documents on HXD BGD estimation for updated results by the start of AO-1 observations.



## Chapter 3

# Observation Policies

The prime instrument on *Astro-E2* will be the XRS, a state-of-the-art, high throughput X-ray spectrometer, capable of high resolution spectroscopy over the 0.3 - 12 keV band. This instrument operates at very low temperatures (0.060 Kelvin). It is cooled using an Adiabatic Demagnetization Refrigerator (ADR) in combination with solid and liquid cryogens, which have a limited lifetime ( $\sim 2.5$  years). Due to this limitation, the policy of awarding the observing time on *Astro-E2* varies somewhat from that used for the recent X-ray astronomy missions such as ASCA, *Chandra*, or *XMM-Newton*. Since any observations primarily requiring instruments other than the XRS can be conducted after the cryogens are expended, priority will be given to proposals whose science objectives require the use of the XRS. Because of this, the details given in this document emphasize the XRS over the other instruments.

Over the lifetime of the XRS, the majority of all observations is reserved for Japanese, US, and ESA Guest Observers (GOs) and will be allocated via a competitive proposal review. A certain amount of the observing time is reserved for the *Astro-E2* Science Working Group (SWG), which consists of the instrument, software, and operations teams, and a few external Science Advisors.

The current best estimate for the schedule of the *Astro-E2* mission is given in Table 3.1. For the purpose of proposal selection, we assume 37 ksec of good on-source time per day, and 360 days of operations per year. Furthermore, observatory time (5%) and TOO time (3%) will also be reserved from this total. Therefore, the net observing time in the current AO (Phase Ib of Table 3.1) available to Japanese, US, and ESA proposers is  $\sim 3860$  ksec,  $\sim 3980$  ksec, and  $\sim 735$  ksec respectively. It is anticipated that an additional  $\sim 12$  calendar months of observing time with the XRS will be available in the next *Astro-E2* AO (Phase Ic), and possibly more in Phase Id.

The nationality of the PI's institution determines which agency should receive the proposal. That is, resident researchers at US institutions must submit their proposals to NASA and those at institutions in ESA member countries must submit theirs to ESA. While the ISAS/JAXA proposal process is primarily aimed at researchers resident in Japan, proposals from researchers in other (non-US, non-ESA) countries will also be considered. In addition, Co-Is from any country may be part of any proposal.

In Phase Ib, 5% of the total observing time is set aside for Japan-US joint investigations. When the respective national reviews have selected the same target, the two proposals will be merged if both teams indicated their willingness to collaborate on the RPS form, and the observation will be

Phase	Months Post-Launch	SWG	Japan (ESA)	US	Japan/US
0	<1	0	0 (0)	0	0
Ia	1–7	100	0 (0)	0	0
Ib	8–19	25	37.5 (6)	32.5	5
Ic	20–31	15	42.5 (7)	37.5	5
Id	32–cryogen end	0	50 (8)	37.5	12.5
II	indefinite	0	60 (10)	30	10

Table 3.1: The preliminary schedule for *Astro-E2* and percentage of time for each group of observers. The ESA time is in parentheses as it is part of the Japanese allotment.

counted against the Japan-US time. If such mergers do not take up 5% of total time, the remainder will be divided between separate Japanese and US investigations.

### 3.1 Data Rights

The data rights policy for *Astro-E2* is similar to previous missions. The normal exclusive period for both SWG and GO data is one year, except that all Phase Ia SWG science data will be made available at the end of Phase Ib. It is also expected that some selected targets from the SWG list will be released immediately to the community, although which targets will be released is not available as of this writing. Please check the *Astro-E2* websites (see Appendix C) for updates.

### 3.2 Target of Opportunity (TOO) proposals

TOO proposals are allowed for *Astro-E2* through the normal proposal process. However, these may only include unpredictable phenomena in a specific target (*e.g.* SS Cyg in outburst), not a generic target (*e.g.* the next Galactic supernova). The triggering criteria must be clearly defined and stated in detail in the proposal text; a brief summary should appear in the Remarks section of the target form. It will be the PI's responsibility to notify the *Astro-E2* project when the criteria are met. It is anticipated that there will exist a mechanism to allow TOO proposals outside the formal proposal review process. This mechanism can be used for generic TOOs; however, the rights for this data will be determined at the Director's discretion. In addition, for gamma-ray bursts (GRBs), the SWG has allocated 200 ksec to perform coordinated observations following alerts from other monitoring satellites. Therefore, **no GO TOO proposals will be accepted for additional GRBs.**

### 3.3 Pointing constraints

The Solar panels on the *Astro-E2* satellite are fixed. This places a restriction on the pointing direction with respect to the satellite-Sun line: the Sun angle constraint is normally 65 - 115 degrees. This means that at any given time of the year, only a swath of the sky 50 degrees wide is accessible for astronomical observations, and thus most celestial sources are available for observations for about 50 days every 6 months. If a specific observing date or a coordinated observation with other missions is required, the proposer must first determine if the observation is possible. This can be done using the "Viewing" tool on the *Astro-E2* proposal website (see Appendix C).

It is anticipated that long (>1 day) observations will be the norm for *Astro-E2*, based both on the *Astro-E* and the *Astro-E2* SWG target lists. In addition, a large number of short observations

is an inefficient use of the satellite because of the unusable time during slews and attitude settling. The pointing is expected to be accurate to 0.3 arcmin and can be reconstructed to better than 0.2 arcmin, except during the initial settling period of up to 10 minutes. Moreover, there is a limit on the number of slews that can be uploaded to *Astro-E2*. For these reasons, a minimum exposure time of 10 ksec has been set for all proposed observations. However, raster observations over a small ( $< 1^\circ$ ) area of the sky may be allowed where the individual pointings are at least 3 ksec. For such observations, the total exposure time (which must still be at least 10 ksec) and the number of separate pointings should be entered into the RPS form. Particularly complicated operations may not be feasible; please contact either the ISAS/JAXA *Astro-E2* team or the NASA *Astro-E2* GOF for assistance on difficult or unusual observation plans.

There are also orbital constraints upon the orientation of the projection of the XRS array on the sky. Since the *Astro-E2* XRS array is roughly square (unlike the rectangular array used for *Astro-E*), selecting a specific roll angle (see Fig. 2.5) is less significant. However, since support structures in the XRT-S will cross the array in a diagonal X pattern, some roll angle constraints may be useful. If a specific roll angle is scientifically advantageous, the proposer must first determine if it is allowed. This can be done using the MAKI tool described in §4.7. Then the required roll range can be entered on the RPS proposal form. For objects close to the ecliptic poles it is possible to arrange for any XRS orientation by scheduling observations at a specific time, but for those located close to the ecliptic, the XRS will project on the sky in a nearly fixed orientation. **Note that any roll constraint will make a proposal time critical.** Due to their increased overhead, only a fraction of the total available time can be used for constrained observations, and proposers should justify their requirements carefully.

During a pointed observation, there will be interruptions due to the location of *Astro-E2* in a low Earth orbit. Normally, a target will be occulted by the Earth for  $\sim 30$  minutes every satellite orbit. In addition, *Astro-E2* will pass through the South Atlantic Anomaly (SAA) during parts of 5 or 6 orbits every day. Due to the harsh radiation environment of the SAA, scientific observation is not possible during SAA passages. There are other variations in the particle background, depending primarily on the cut-off rigidity<sup>1</sup>. It is likely that some high background region will typically be excluded from data analysis; however, the extent to which this is the case will be determined with in-orbit experiences.

### 3.4 Sequence of events after submission

After the *Astro-E2* proposal deadline, there will be three independent proposal reviews for the US, Japan, and ESA proposals. Each review will create a target list from the proposed observations, ranking the accepted targets as category A, B, or C. Only category A and B targets are guaranteed to be observed; category C targets will be observed as time permits. Category A observations will be deemed to be complete when they have received at least 90% of the requested time with the XRS detector. Category B observations are considered complete after they have been observed with the XRS for 70% of the requested time. Category C observations are performed on a best-effort basis.

Even though observations are scheduled to acquire roughly the approved exposure time, and ASCA experiences suggest this will usually be achieved with *Astro-E2*, occasional losses of usable observation time are inevitable. Additional observations will be scheduled automatically for non-time-critical targets whose observations are considered incomplete by the project scientist at ISAS. In the case of time-critical observations which are incomplete or unusable, it will be the PI's

---

<sup>1</sup>*Astro-E2* will be protected from solar and cosmic-ray particles by the geomagnetic field; cut-off rigidity is an indicator of the minimum momentum required for a particle to reach a specific location, given the average geomagnetic field configuration.

responsibility to determine the best course of action.

An international merging committee will collate the three target lists and produce a single, unified list. Overlaps between US and Japanese targets will be resolved, either by merging the investigations (if both parties are willing) or by choosing one. In the latter process, the priority given by the national reviews, as well as the lengths of the accepted observations, will be considered. The final target list will be  $\sim 40\%$  oversubscribed. Category A targets will have 50% of the available time, category B 40%, and category C 50%.

US PIs, or US Co-Is on foreign PI projects, may propose for funding once notified that their target has been accepted. This process is described in ROSS 2004 document; further details of this process will be made available on the NASA *Astro-E2* GOF website listed in Appendix C.

Each PI will be assigned a contact scientist, either at ISAS or the NASA *Astro-E2* GOF, who will work with the PI to assure the maximum science return. This will include double-checking coordinates, reviewing the Filter Wheel settings, and confirming the XIS configuration. It is important to note that once an observation has been scheduled, any delay in responding to questions from the contact scientist may result in targets being removed from the schedule. Special scheduling request and TOO's will be accommodated on a best effort basis. For simultaneous observations, the mission scheduler at ISAS, in consultation with the contact scientist, will contact the PI in advance for detailed scheduling information, and will often work directly with schedulers of other missions. For Phase Ib, we do not have a mechanism to approve coordinated observations with *Astro-E2* and another observatory through a single proposal. It is the PI's responsibility to secure observing time with other observatories, when simultaneous observations are desirable; **the *Astro-E2* component of such a proposal may be approved contingent on the success of other proposals.**

Once the observation has been completed, the data will be promptly run through the processing pipeline and put into both the US and Japanese archives, initially in encrypted form. The PI will be sent the decryption key along with instructions on how to download and decrypt the data.

With the exception of the code that converts raw binary telemetry into FITS format files, all *Astro-E2* software will be written as FTOOLS and distributed through the *Astro-E2* team at ISAS/JAXA and the NASA/GSFC HEASARC. This includes the tools used in the processing. All calibration files will be distributed through the HEASARC `caldb` (Calibration Database) system. This will enable users to apply any calibration updates themselves. The *Astro-E2* team at ISAS and the NASA *Astro-E2* GOF will provide additional FTOOLS that may be necessary or desirable in analyzing *Astro-E2* data. Use of other software packages will only be supported at a lower priority level.

## Chapter 4

# Guide to Writing An *Astro-E2* Proposal

Each *Astro-E2* proposals must include at a minimum the source coordinates, exposure time, instrument configuration and expected count rates, and any observing constraints within the four page limit. The review panels will base their decision primarily upon the justification of the proposed science to be done with the data. This chapter describes how to prepare a strong proposal, including the various software tools available to assist the proposer.

### 4.1 Ingredients of a Successful *Astro-E2* Proposal

While it is conceivable that one would wish to study a previously unknown X-ray source with the XRS, a more likely scenario would involve a detailed spectroscopy of an object with known X-ray flux. A viable proposal should state the scientific objective as to what new information will be gleaned from the high resolution spectrum. Of crucial importance is the justification for the requested exposure time, especially given the limited lifetime of the XRS. This will likely require at least a simulation of the expected spectrum, or possibly a simulation of the entire observation.

Every *Astro-E2* proposal must have an estimate of the expected counting rates from the proposed target. This rate is used both by the reviewers to evaluate the viability of the proposal and the operations team to evaluate any safety concerns. The simplest tool to use in estimating the expected XRS or XIS count rate is PIMMS. This tool is freely available as a stand-alone tool or on the Web as WebPIMMS; see Appendix C for locations. The next level of detail is provided via simulations using XSPEC, and such simulations should provide significant insight into the expected spectrum obtained from a proposed observation. A brief guide to XSPEC simulations is given in § 4.3. In many case, this should be sufficient for a point source. There are also tools available to simulate imaging data, which may be useful for an extended source or a particularly bright source. In particular, the most powerful tool is `xrssim`, which can use a FITS format image with an assumed spectral shape of the source to estimate the distribution of events in all elements of the XRS array.

### 4.2 Using PIMMS and WebPIMMS

This tool is an interactive, menu-driven program, which has an extensive HELP facility. It is also available as the web-based tool WebPIMMS. In either case, users specify the flux and spec-

tral model with its parameters, and PIMMS/WebPIMMS returns the predicted counting rate. PIMMS/WebPIMMS can be used for a variety of other instruments, so if for instance the counting rate and spectrum of a given source observed with the ROSAT PSPC is known, it can calculate the flux, which in turn can be used as input to estimate the XRS counting rate.

### 4.3 Using XSPEC to Simulate an Observation

Perhaps the easiest tool for simulating X-ray spectra is the XSPEC program (a part of the XANADU software package), which is designed to run on a variety of computer platforms and operating systems and is freely distributed on the NASA GSFC HEASARC Website (see Appendix C). The simulation of an XRS observation requires the current instrument redistribution matrix (the so-called .rmf file) and the energy-dependent effective area of the instrument (the so-called .arf file), both available on the Web or via anonymous FTP (see Appendix C). For the purpose of the simulation, these files assume that all pixels can be described by a single matrix, and that the source of photons is a point source. Although the on-orbit performance of the XRT-S is unknown, the point source .arf file assumes that 64% of the photons from an on-axis point source will reach the XRS array, based on a conservative estimate (2.0') of the XRT-S HPD. For a constant diffuse source that fills the field of view, the XRS array will be more uniformly illuminated and the effective area (and thus count rate) will be slightly larger ( $\lesssim 50\%$ ), although the exact value depends on the surface brightness and spectrum of the source. The best estimate of the XRS effective area for a diffuse source can be calculated using `xrssim` (described below).

The procedure for simulations is relatively simple: if the XSPEC program is installed, one should start XSPEC making sure that the proper .rmf and .arf files are accessible. Within XSPEC, one should specify the spectral model, such as hot thermal plasma or the like (via `model` command). Specifying the model will drive XSPEC to query for the model parameters (such as temperature and abundances for an APEC collisional plasma model), as well as normalization. The key command to create a simulated spectrum is the `fakeit` command, which will query for the redistribution response (the .rmf file), and the ancillary response (the .arf file). The `fakeit` command also will request the simulated data filename, and the length of simulated observation. One can now use this file within XSPEC to determine the sensitivity of the simulated data file to changes in the model parameters.

#### 4.3.1 Using WebSPEC to Simulate an Observation

Most of the features of XSPEC are also available as a web-based tool on the HEASARC website (see Appendix C). WebSPEC calls XSPEC behind the scenes, so all the issues described above apply here as well. WebSPEC contains the effective area and response files for *Astro-E2* already, and allows the proposer to simply select which filters will be used. The fact that the XRS array does not sample the entire beam is also taken into account in the effective area.

After selecting the instrument, WebSPEC allows the user to choose the spectral model, such as an absorbed collisional plasma or a power-law spectrum with an absorption component. The next page will then query for the model parameters (such as temperature and abundances for an APEC collisional plasma model), as well as normalization, exposure, upper and lower energies, and the number of bins to use in the spectral plot. WebSPEC will then create a simulated spectrum after clicking the “Show me the Spectrum” button, using the `fakeit` command. This folds the specified model through the instrument response and effective area, calculating the observed count rate and fluxes as well. WebSPEC will then allow one to download the postscript file of the spectrum, change the model parameters, or replot the data.

## 4.4 Examples

To show how to estimate the proper exposure, we include some simple examples of XRS observations that illustrate the process.

### 4.4.1 Detailed profile of a Fe K line in an AGN

Let us assume that one wants to measure the profile (structure) of an isolated emission line (for instance, the iron  $K\alpha$  line at  $E_{\text{rest}} = 6.4 \text{ keV}$ ). Assume that the continuum flux at 6.4 keV is  $2 \times 10^{-3} \text{ photons cm}^{-2} \text{ s}^{-1} \text{ keV}^{-1}$  (a good approximation for an AGN with a 2 – 10 keV flux of  $\sim 10^{-10} \text{ erg cm}^{-2} \text{ s}^{-1}$ ), while the line flux is  $1 \times 10^{-4} \text{ photons cm}^{-2} \text{ s}^{-1}$ . Assume also that the line is unresolved with an ASCA observation, such that  $\sigma < 50 \text{ eV}$ . We can also assume that the level of continuum is known precisely, from simultaneous observations with the XISs.

To take advantage of the energy resolution of the calorimeter in measuring the structure of the line, one should have a meaningful measurement of the line flux in each 10 eV energy bin to, say, 20% or better. The effective area of the XRS + XRT at 6.4 keV is  $\sim 150 \text{ cm}^2$ . A crude, order-of-magnitude estimate can be made as follows:

The continuum flux in the vicinity of 6.4 keV is  $2 \times 10^{-5} \text{ photons cm}^{-2} \text{ s}^{-1}$  per 10 eV bin. Let us assume for the moment that the line flux is uniformly distributed over 100 eV, or ten 10 eV-wide bins. This means that each 10 eV bin will have  $10^{-5} \text{ line photons cm}^{-2} \text{ s}^{-1}$ . Total is  $3 \times 10^{-5} \text{ photons cm}^{-2} \text{ s}^{-1}$  per 10 eV bin. If one wishes to measure the structure of the line such that the flux of the line in each energy bin is known to 20%, we require the total of 75 line photons per bin (one must consider the Poisson statistics of both line and continuum photons). This now translates to an exposure of  $75/(150 \times 10^{-5}) \text{ s}$ , or  $\sim 50 \text{ ksec}$ . For an isolated line (with no continuum), a similar argument would suggest an observation of  $25/(150 \times 10^{-5}) \text{ s}$ , or  $\sim 17 \text{ ksec}$ .

### 4.4.2 Iron abundance in a region of a cluster of galaxies

Consider a project to measure the abundance of iron in a cluster of galaxies using the He-like and H-like Fe K lines, such that the 90% confidence regions are  $\pm 0.1 \text{ Solar}$ . (In the case of such a hot cluster, most of temperature / abundance information comes from the Fe K rather than Fe L region.) The ROSAT PSPC and ASCA observations indicate that the intervening absorption is small ( $2 \times 10^{20} \text{ cm}^{-2}$ ), the spectrum is well-described by an APEC collisional plasma model with a temperature  $kT$  of 6 keV and abundances of  $\sim 0.3 \text{ Solar}$ , and that the cluster image is circular, with a diameter of  $10'$ . Those data also show that the 0.2 - 2 keV flux from the whole cluster is  $5 \times 10^{-12} \text{ erg cm}^{-2} \text{ s}^{-1}$ , and the surface brightness is reasonably uniform.

An important issue to keep in mind is the surface brightness of the cluster, which affects the results in two ways. First, the XRS subtends only  $\sim 8 \text{ arcmin}^2$  on the sky, while the entire cluster subtends  $\sim 80 \text{ arcmin}^2$ . This means that the 0.2 - 2 keV flux in the XRS beam is only 1/10th of the total, or  $5 \times 10^{-13} \text{ erg cm}^{-2} \text{ s}^{-1}$ . Secondly, since the cluster will fill the XRS field of view, the final count rate might be somewhat conservative since the .arf file assumes the source is a point source.

We begin by simulating the spectrum with XSPEC using a nominal time of 100 ksec, using an absorbed APEC collisional plasma model with a normalization (0.000783) which gives the desired flux between 0.2-2.0 keV:

```
XSPEC> model wabs*apec
Model: wabs<1>( apec<2> )
```

```

Input parameter value, delta, min, bot, top, and max values for ...
1:wabs:nH>0.02
2:apec:kT>6.0
3:apec:Abundanc>0.3
4:apec:Redshift>
5:apec:norm>0.000783
XSPEC> fakeit none
For fake data, file #    1 needs response file: xrs_2d6eV_2003-02-19.rmf
... and ancillary response file: xrs_onaxis_all_2003-09-30.arf
Use counting statistics in creating fake data? (y)
Input optional fake file prefix (max 4 chars):
Fake data filename (xrs_2d6eV_2003-02-19.fak) [/ to use default]: cluster.fak
Exposure time, correction norm  (1, 1): 100000
XSPEC> flux 0.2 2.0
Model flux  4.0046E-04 photons ( 5.0114E-13 ergs)cm**-2 s**-1 ( 0.200- 2.000)

```

We have now created a sample “fake” dataset called `cluster.fak` with the correct flux. To consider only the Fe K lines, we restrict the fit to the 4-10 keV band, where the only strong emission lines are from Fe K. We fit the data using an absorbed APEC model to determine the accuracy to which we can measure the abundance. Note that we have to thaw the model abundance (which is by default fixed), and use the `cstat` statistical model since we have very few counts per bin.

```

XSPEC> freeze 1
XSPEC> thaw 3
XSPEC> statistic cstat
XSPEC> ignore **-4.0, 10.-**
XSPEC> fit
XSPEC> error 2.706 3
Parameter   Confidence Range (      2.706)
      3      0.266950      0.530534      (  -0.113708      ,      0.149875      )

```

This shows that the total 90% confidence range is  $+0.11, -0.15$ , slightly larger than the desired value of  $\pm 0.1$ . However, the source is diffuse and fills the field of view, so the observed count rate might be as much as 50% larger. The potential effect can be quickly estimated by redoing the simulation using a time of 150 ksec and refitting, which leads to a 90% confidence range of  $-0.06, +0.08$ . Therefore, 100 ksec should suffice for this science; to get a more accurate estimate, `xrssim` could be used to simulate the entire observation and get the true count rate.

#### 4.4.3 Measuring plasma turbulence

Suppose we have a collisional plasma source and we want to determine any internal velocity spread in excess of that due to the temperature. V11.3.1 of XSPEC includes two new models, `bapec` and `bvapec`, which apply thermal and gaussian velocity broadening to emission lines. The sigma of the gaussian velocity broadening (in km/s) is a parameter of these models. We can use these models to “fake” a 100 ksec observation and then determine how small a velocity broadening we could detect at the 90% confidence level.

```

XSPEC>model phabs(bapec)
Model:  phabs<1>( bapec<2> )
Input parameter value, delta, min, bot, top, and max values for ...

```



```

1:phabs:nH>0.1
2:bapec:kT>4
3:bapec:Abundanc>0.3
4:bapec:Redshift>0.05
5:bapec:Velocity>200
6:bapec:norm>
...
XSPEC>thaw 3
Number of variable fit parameters =    4
XSPEC>new 6 1e-2
XSPEC>ignore 0.-0.5 10.-**
  ignoring channels      1 -    501 in dataset      1
  ignoring channels 10000 - 16384 in dataset      1
XSPEC>fakeit none
For fake data, file #    1 needs response file: xrs_2d6eV_2003-02-19.rmf
      ... and ancillary response file: xrs_onaxis_all_2003-09-30.arf
Use randomization in creating fake data? (y)
Input optional fake file prefix (max 4 chars):
Fake data filename (xrs_2d6eV_2003-02-19.fak) [/ to use default]: test.fak
Exposure time, correction norm (1, 1): 100000
Net count rate (cts/s) for file   1  0.4233   +/-  2.0575E-03
  using response (RMF) file...      xrs_2d6eV_2003-02-19.rmf
  using auxiliary (ARF) file...      xrs_onaxis_all_2003-09-30.arf
Chi-Squared =      7513.420   using  9498 PHA bins.
Reduced chi-squared =      0.7913862   for  9494 degrees of freedom
Null hypothesis probability =  1.00
XSPEC>stat cstat
C-statistic =      8794.805   using  9498 PHA bins.
XSPEC>fit
-----
Model:  phabs<1>( bapec<2> )
Model Fit Model Component  Parameter  Unit      Value
par  par comp
  1   1   1   phabs      nH        10^22    0.100616   +/-  0.336496E-02
  2   2   2   bapec      kT         keV      3.92762   +/-  0.493891E-01
  3   3   2   bapec      Abundanc      0.305391   +/-  0.129515E-01
  4   4   2   bapec      Redshift      5.000000E-02 frozen
  5   5   2   bapec      Velocity km/s    200.000   frozen
  6   6   2   bapec      norm        1.007288E-02 +/-  0.105322E-03
-----

```

We have now created a fake 100 ksec observation using an absorbed apec model that includes a 200 km/s velocity broadening to all lines, and then fit it while fixing the velocity broadening and redshift. We now allow the velocity term to vary and have XSPEC calculate the 90% confidence interval around the best-fit value:

```

XSPEC>thaw 5
XSPEC>fit
-----
Model:  phabs<1>( bapec<2> )

```

Model	Fit	Model	Component	Parameter	Unit	Value		
par	par	comp						
1	1	1	phabs	nH	10 <sup>22</sup>	0.100600	+/-	0.336504E-02
2	2	2	bapec	kT	keV	3.92907	+/-	0.494203E-01
3	3	2	bapec	Abundanc		0.303315	+/-	0.129845E-01
4	4	2	bapec	Redshift		5.000000E-02	frozen	
5	5	2	bapec	Velocity	km/s	167.628	+/-	23.4625
6	6	2	bapec	norm		1.007846E-02	+/-	0.105433E-03

-----

XSPEC>unc 5

Parameter	Confidence	Range (	2.706)				
5	132.119	205.914	(	-35.5092	,	38.2857	)

So a 100 ksec observation could easily detect the intrinsic 200 km/s velocity broadening of this plasma, with the 90% confidence interval ranging from 132–205 km/s.

## 4.5 Using XRSSIM

`xrssim` is an *Astro-E2* XRS event simulator. It reads a FITS format photon list file, traces photon paths in the telescope (via ray-tracing), and outputs a simulated XRS event file. XRT thermal shield transmission, XRS filter wheel transmission, and XRS detection efficiency are taken into account if requested. Each record of the photon list file describes the celestial positions, arrival time, and energy of the input photon. The `mkphlist` ftool can create such photon list files from FITS images (e.g., ROSAT HRI images) and spectral models (which may be created in XSPEC). The `xrssim` output event file may be analyzed just like a real data, using standard analysis tools such as `xselect`.

When planning XRS observations, there will be at least two situations where `xrssim` will be useful:

- For extended sources, users can obtain the expected numbers of events on each pixel. Users can specify the pointing direction and roll-angle through the satellite Euler angle.
- For point sources, users may estimate branching ratios of the event grades (high, medium or low) for each pixel. Also, users can calculate expected number of events for each pixel when the source is put at an off-axis positions.

These programs are available from the Tools web page listed in Appendix C.

### 4.5.1 An X-ray binary simulated with `xrssim`

We consider here an observation of GX13+1, an LMXB with Fe K lines that happens to be a SWG target. One of the goals of the observation is to resolve and measure the Fe K lines. From §2.3 we know that the fraction of high resolution events declines when the source flux becomes too high (cf. Fig 2.11), which would affect the results. This can be mitigated using either the neutral density filter or the Be filter, at the cost of substantially reducing the count rate. To properly evaluate the best filter setting requires an `xrssim` simulation. Fortunately, this is not difficult.

After installing the `mkphlist` and `xrssim` software, the first step is to prepare the input spectrum for `mkphlist`. After finding a good spectral model for the source (in this case, taken from Ueda et al. 2001, ApJ, 556, L87), we set up the model in XSPEC as follows:

```
XSPEC> model wabs*edge*(diskbb + bb + gauss + gauss)
Model: wabs<1>*edge<2>( diskbb<3> + bbody<4> + gaussian<5> + gaussian<6> )
Input parameter value, delta, min, bot, top, and max values for ...
1:wabs:nH>2.9
2:edge:edgeE>7.61
3:edge:MaxTau>0.13
4:diskbb:Tin>0.91
5:diskbb:norm>1078.72
6:bbody:kT>1.45
7:bbody:norm>0.1224
8:gaussian:LineE>6.42
9:gaussian:Sigma>0.02
10:gaussian:norm>2.48e-3
11:gaussian:LineE>7.01
12:gaussian:Sigma>0.02
13:gaussian:norm>-3.465e-3 0.01 -1 -1 1 1
XSPEC> dummyrsp 0.1 10 3000 lin
XSPEC> flux 0.1 10
Model flux 1.897 photons ( 1.1863E-08 ergs)cm**-2 s**-1 ( 0.100- 10.000)
XSPEC> plot model
XSPEC> iplot
XSPEC> wdata spectrum.qdp
```

These commands define the model, show the total flux, and create an input spectrum file `spectrum.qdp` with energy bins 3.3 eV wide. This is adequate since only an estimate of the count rates for the different event types is needed. Finer binning might be needed for other projects, such as estimating how accurately a narrow line could be measured. Now `spectrum.qdp` can be used input to `mkphlist` to generate a list of photons to be simulated by `xrssim`. For this example, we run `mkphlist` as follows:

```
unix% mkphlist
photon flux in photons/s/cm2 (astePhotonGen)[3.325] 1.897
Emin (keV) for photon flux (astePhotonGen)[2.0] 0.1
Emax (keV) for photon flux (astePhotonGen)[10.0] 10.0
SPEC-MODE 0:QDP-SPEC, 1:MONOCHROME (astePhotonGen)[0] 0
qdp spectral file (astePhotonGen)[crab.qdp] spectrum.qdp
IMAGE-MODE 0:FITS-IMAGE, 1:POINT-LIKE (astePhotonGen)[1] 1
R.A. (deg) for point source (astePhotonGen)[83.5] 273.63
DEC (deg) for point source (astePhotonGen)[22.0] -17.157
TIME-MODE 0:CONSTANT, 1:POISSON (astePhotonGen)[1] 1
LIMIT-MODE 0:NPHOTON, 1:EXPOSURE (astePhotonGen)[1] 0
exposure time in sec (astePhotonGen)[20] 1000000
output photon FITS file (astePhotonFITSwrite)[crab.photons] gx13.photons
```

The meaning of these parameters is explaining in the documentation accompanying `mkphlist`, but briefly, the first five set the total flux, energy range, and spectrum type. `mkphlist` can use

a FITS image or simply assume a point source for input. The source position (RA,Dec) is not required for this purpose, but can be used. Finally, the events may be distributed either evenly spaced or with poisson distribution. We use the poisson distribution, since this will affect which photons become Hi-, Mid- or Low-res. Finally, we selected a run with  $10^6$  photons, and put the output into the file `gx13.photons`.

This file can now be input to `xrssim`, as shown here. Note that `xrssim` uses a number of FITS files for which the default files should be used. The exact command sequence for our example is:

```
unix% punlearn xrssim
unix% xrssim
teldef file for XRS (SimASTERoot)[xrs_teldef_2003-02-15.fits]
default 1st Euler Angle (deg) (SimASTERoot)[83.5] 273.63
default 2nd Euler Angle theta (deg) (SimASTERoot)[68.0] 107.157
default 3rd Euler Angle psi (deg) (SimASTERoot)[0.0]
Name of input photon file #1 (astePhotonRead)[crab.photons] gx13.photons
Name of input photon file #2 (astePhotonRead)[none]
Xray Telescope Description File name (asteXRTsim)
[xrt-s_geometry_45degrot_1999-02-19.fits]
Reflection Table file name (asteXRTsim)[xrt-s_reflect_2003-09-10.fits]
Pre-Collimator Description File name('none' means no use of collimator) (asteXRTsim)
[xrt-s_precollimator_geometry_45degrot_2003-09-11.fits]
Pre-Collimator Reflection (asteXRTsim)[xrt-s_reflect_2003-09-10.fits]
XRT thermal shield transmission file (asteXRTsim)
[xrt_thermal_shield_trans_2003-01-20.fits]
Name of input RMF file (asteXSRMFsim)[xrs_2d6eV_2003-02-19.rmf]
XRS Filter Wheel filter transmission file (asteXSRMFsim)[none]
Multiply XRS efficiency or not (asteXSRMFsim)[yes]
Discard events fallen outside of pixels (asteXSRMFsim)[no]
output event FITS file (asteEventFITSwrite)[crab.events] gx13_evt.fits
```

The inputs for `xrssim` are described in the documentation, but a short review is given here. The fields called “teldef file for the XRS”, “Xray Telescope Description File”, “Reflection Table”, “Pre-Collimator Description File”, “Pre-Collimator Reflection”, “XRT thermal shield transmission”, and “Name of input RMF file” should be left unchanged and all the files described should be in the current directory. The remaining options can be varied to set the pointing direction, filters used, and the details of the simulation. The 1st Euler Angle should be set to the RA of the source used in `mkphlist`. **However, the Euler angle theta is defined as  $90^\circ$  minus the target Declination, so  $\text{theta}(\text{xrssim}) = 90 - \text{DEC}(\text{mkphlist})$ .** The Euler Angle psi is similarly related to the *Astro-E2* Roll Angle, such that the **Roll Angle** =  $90 - \text{psi}$ . If desired, the XRS Filter Wheel transmission file can be set to `xrs_fw_pos3.be300_trans_2003-11-10.fits` to use the  $300\mu\text{m}$  Be filter. The 10% neutral density filter can be approximated by simply reducing the input flux in `mkphlist` by a factor of 10. Optionally, the XRS efficiency may be included or not, and events that do not land on a pixel may be excluded to save space.

The final result of this run is the file `gx13_evt.fits` and a table of pixel statistics, output at the end of the `xrssim` run. For this run, the table breaks the emission down by pixel, and a précis is shown here:

Pixel	Total	Hi-Res	Mid-Res	Low-Res	Secondary
7	11759	5(0.04%)	1949(16.5%)	9805(83.3%)	11492(97.7%)
15	2392	553(23.1%)	1076(44.9%)	763(31.8%)	1233(51.5%)

```
...
all      118812    13015(10.9%)    38224(32.1%)    67573(56.8%)    89462(75.2%)
```

Out of the 118,812 events detected only 11% will be Hi-res; more than will pass the 10% neutral density filter, but possibly adding the 300 $\mu$ m filter would increase the number of Hi-res counts. However, primary Mid-res counts have nearly the same resolution as Hi-res counts, so we should check that first. This can be done using the FTOOL `fstatistic`:

```
unix% fstatistic "gx13_evt.fits[EVENTS][PIXEL.ge.0 && PIXEL.ne.3 &&
FLAG_MIDRES.ne.0 && FLAG_SECONDARY.eq.0]"
```

which in this case shows 10,058 matching rows with a primary (i.e., FLAG\_SECONDARY is 0) Mid-res (i.e., FLAG\_MIDRES is not 0) event. Adding that to the 13,015 Hi-res events shows that  $\sim 19\%$  of the events will have good energy resolution. Re-running the simulation (using the same `gx13.photon` file) with the 300 $\mu$ m Be filter file listed above returns

Pixel	Total	Hi-Res	Mid-Res	Low-Res	Secondary
7	5670	163(2.87%)	2207(38.9%)	3300(58.2%)	4723(83.2%)
15	1092	557(51.0%)	350(32.0%)	185(16.9%)	311(28.4%)
...					
all	57210	14698(25.6%)	21827(38.1%)	20685(36.1%)	31756(55.5%)

So at a cost of more than half the events, we can increase the Hi-res fraction to 25.6% percent—but the actual number of counts (14,698) is only slightly more than with the OPEN filter (13,015). Re-running the `fstatistic` command adds an additional 7000 primary Mid-res events for a total of 21,698—fewer than the 22,902 seen with the OPEN filter. We therefore chose to use the OPEN filter, since it returns the most data.

It should also be noted that unlike CCD pile-up, **there is very little degradation of the energy resolution in Hi-res and primary Mid-res events detected from high flux sources.** CCD pileup, especially at small or moderate levels, is difficult to detect since the piled-up events simply appear to be from higher-energy photons. This is not the case with the calorimeter. Even for Low-res events, the true energy is measured; only the accuracy of the measurement is affected. However, X-rays hitting the silicon frame outside of the pixels and thermal crosstalk from other pixels are a source of noise that at very high incident flux begins to degrade the XRS resolution in the Hi-res and Mid-res grade events. For an observation of a point source, we project that the resolution will degrade to  $\sim 10$  eV for source fluxes (in the *Astro-E2* XRS bandpass) of  $10^{-8}$  ergs/s/cm<sup>2</sup>.

## 4.6 Using Viewing

One of the first tasks in preparing a proposal is determining when and for how long a target can be observed. This can be easily done with Viewing, a simple Web-based interactive tool (see Appendix C for location) that can determine visibility for many different satellites. To use Viewing, simply enter the target name or coordinates, and select the satellite. Viewing will return all the available dates when that target will be available.

## 4.7 Using MAKI

MAKI is another Web-based interactive tool (see Appendix C) that can determine the orientation of the XRS array (or the XIS) on the sky as a function of the observation epoch within the visibility window of the target. For *Astro-E2*, the orientation of the Solar panels with respect to the spacecraft is fixed, and at the same time, the range of the angles between the vector normal to the Solar panels and the vector pointing to the Sun is restricted, which in turn restricts the roll angle of the spacecraft.

When using the tool, general instructions are available via the “Help” button. section. To check the visibility and available roll angles for a target, first load an image. This can be done with either an existing FITS image, or by entering the RA and Declination of the source and clicking the “New Graph” button. This creates an image upon which the *Astro-E2* XRS or XIS field of view (FOV) will be shown.

The “Mission and Roll Selector” (in the upper right of the display) allows different instruments from different missions to be selected. After selecting either the *Astro-E2* XRS or XIS, a FOV will appear on your image. The FOV can be rotated using the “Roll angle” slider bar.

## 4.8 Guide to Using the RPS

RPS, or the Remote Proposal Submission tool, must be used to enter the basic proposal data into the ISAS/JAXA, HEASARC, or ESA database. Proposers should make sure they use the correct RPS, since there are multiple reviews. See Appendix C for the list of RPS websites and addresses. Two versions of RPS are available: a character-oriented version, where the user submits all the required information via e-mail, or a Web-oriented version.

One aspect of RPS that is not immediately obvious is how to specify the time-constrained observations. For instance, a need for such an observation may arise for a study of a spectrum of a binary system in a particular orbital phase. If some particular aspect of the observation cannot be clearly specified in the RPS form, the user should detail it in the “comments” field of the RPS form and/or contact either the *Astro-E2* team at ISAS/JAXA or the NASA *Astro-E2* GOF before submitting.

## 4.9 Checklist

A successful *Astro-E2* proposal, from a technical point of view, must include the following elements:

**Coordinates:** The PI is responsible for supplying the correct J2000 coordinates. For extended sources, specify single FOVs (coordinates for the center of XRS array) or rastering parameters (a schematic drawing overlaid on images would be the least ambiguous; equivalent textual descriptions are acceptable).

**XRS Count rate and exposure time:** Explain how they were calculated; optionally, select a filter; note the (post-filter) count rate on the form (for a highly variable source, added explanation — such as “excluding any bursts” — would be helpful).

**Observing constraints, if any:** These include monitoring, coordinated, phase-dependent, and roll-dependent; TOOs are allowed, but the triggering criteria must be spelled out in text, and summarized in target remarks.

Note that the GOs are allowed to propose for targets already approved for the SWG time (see the Announcement of Opportunity). However, GOs must explain why the already-approved observation does not meet their scientific objectives. Valid reasons include a much longer exposure time ( $\sim 3\times$  longer); incompatible time constraints; different positions within an extended source.

We note also that the XISs are also subject to count rate limitations, because of possible multiple events in an XIS pixel within one frame (see § 7.6). This is much less of a problem than with the ACIS aboard *Chandra*, as *Chandra*'s mirror focuses the X-ray flux into a region of a CCD that is orders of magnitude smaller. The rule of thumb is that the XIS can tolerate a point source with a count rate up to  $\sim 10$  counts  $\text{s}^{-1}$  per CCD with essentially no loss of counts or resolution. For brighter sources, these limitations can be reduced via a variety of XIS modes, such as the use of a sub-array of the XIS, as discussed in § 7.5. More details regarding which XIS mode is most appropriate for what observation will be known after *Astro-E2* is in orbit, so for borderline cases the proposer may choose to specify the default (full-frame) mode of the XIS, and coordinate adjustments with their contact scientist later.

## 4.10 Additional Requirements for US Proposers

There are three additional NASA-specific proposal rules that must be followed by US proposers. First, a “Notice of Intent” (NOI) should be submitted to the Web address listed in the official announcement (see Appendix C) by June 16, 2004. Filing a NOI will aid the NASA *Astro-E2* GOF in organizing the proposal review, although proposals may be submitted without first filing an NOI. Secondly, a NASA Cover Page which includes a proposal and budget summary **must** be generated, using the Web form listed in §C. The cover page requires some budget information, and as noted in the official NASA announcement, a placeholder value of \$1 should be used since budget information is not required until Stage 2. After submitting the cover page, a copy should be printed and saved for use in the Stage 2 budget process. Finally, as described in the NRA, the NASA Office of Space Science requires all proposals to demonstrate their relationship to NASA Goals and Research Focus Areas (RFAs). Therefore, each proposal should include a sentence stating its specific relevance to one of the RFAs given in Table 1 of the Summary of Solicitation. In particular, *Astro-E2* science will often address the science themes in the “Astronomical Search for Origins” and the “Structure and Evolution of the Universe.”

## Chapter 5

# X-Ray Telescopes (XRTs)

*Astro-E2* has five light-weight thin-foil X-Ray Telescopes (XRTs). The XRTs have been developed jointly by NASA/GSFC, Nagoya University, Tokyo Metropolitan University, and ISAS/JAXA. These are grazing-incidence reflective optics consisting of compactly nested, thin conical elements. Because of the reflectors' small thickness, they permit high density nesting and thus provide large collecting efficiency with a moderate imaging capability in the energy range of 0.2-12 keV, all accomplished in telescope units under 20 kg each.

Four XRTs onboard *Astro-E2* (XRT-I) are used on the XIS, and the other XRT (XRT-S) is for the XRS. They are arranged on the Extensible Optical Bench (EOB) on the spacecraft in the manner shown in Figure 5.1. Because of the different space requirement in the spacecraft for the micro-calorimeter, the XRT-S is different in terms of focal lengths than that of the 4 XRT-I's. Consequently, the number of the reflectors and their angular placement are also different. The external dimensions of the 5 XRTs, however, are the same (See Table 5.1, which also includes a comparison with the ASCA telescopes).

The angular resolutions of the XRTs range from  $1.5'$  to  $2.3'$ , expressed in terms of half-power diameter, which is the diameter within which half of the focused X-ray is enclosed. The angular resolution does not significantly depend on the energy of the incident X-ray in the energy range of *Astro-E2*, 0.2-12 keV. The effective areas are typically  $440 \text{ cm}^2$  at 1.5 keV and  $250 \text{ cm}^2$  at 8 keV. The focal lengths are 4.75 m for the XRT-I and 4.5 m for the XRT-S. Individual XRT quadrants

	<i>Astro-E2</i> XRT-I	<i>Astro-E2</i> XRT-S	ASCA
Number of telescopes	4	1	4
Focal length	4.75 m	4.5 m	3.5 m
Inner Diameter	118 mm	119 mm	120 mm
Outer Diameter	399 mm	400 mm	345 mm
Height	279 mm	279 mm	
Mass/Telescope	19.5 kg	18.5 kg	9.8 kg
Number of nested shells	175	168	120
Reflectors/Telescope	1400	1344	960
Geometric area/Telescope	$873 \text{ cm}^2$	$887 \text{ cm}^2$	$558 \text{ cm}^2$
Reflecting surface	Gold	Gold	Gold
Substrate material	Aluminum	Aluminum	Aluminum
Substrate thickness	$155 \mu\text{m}$	$155 \mu\text{m}$	$127 \mu\text{m}$
Reflector slant height	101.6 mm	101.6 mm	101.6 mm

Table 5.1: Telescope Dimensions and Parameters of XRT



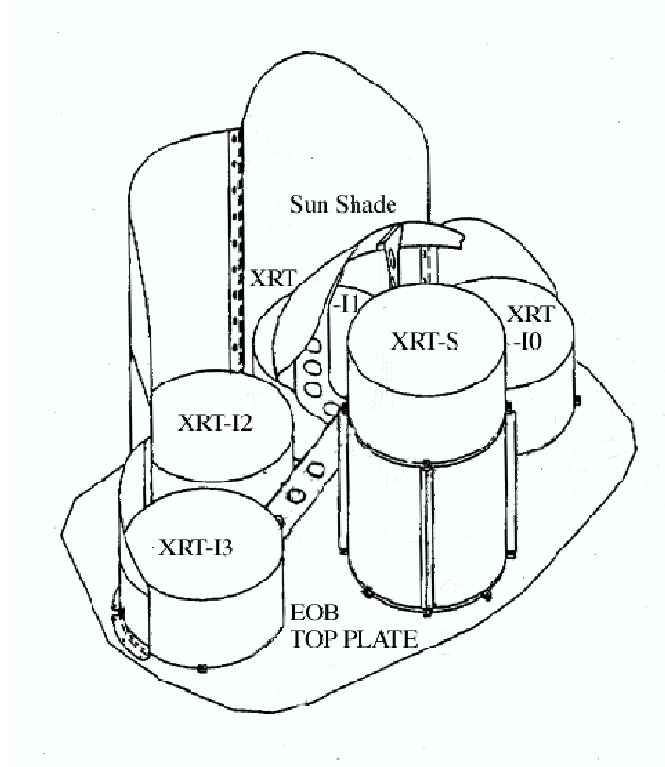


Figure 5.1: Layout of the 5 XRTs on the *Astro-E2* spacecraft.

have their component focal lengths deviated from the design values by a few cm. The optical axes of the quadrants of each XRT are aligned within 2' from the mechanical axis. The field of view for all 5 XRTs is about 17' at 1.5 keV and 13' at 8 keV. (see also Table 2.1)

## 5.1 Basic Components of XRT

The *Astro-E2* X-Ray Telescopes (XRTs) consist of closely nested thin-foil reflectors, reflecting X-ray at small grazing angles. An XRT is a cylindrical structure, having the following layered components: 1. a thermal shield at the entrance aperture to help maintain a uniform temperature; 2. a pre-collimator mounted on metal rings for stray light elimination; 3. a primary stage for the first X-ray reflection; 4. a secondary stage for the second X-ray reflection; 5. a base ring for structural integrity and interface with the EOB of the spacecraft. All these components, except the base rings, are constructed in 90° segments. Four of these quadrants are coupled together by interconnect-couplers and also by the top and base rings (Figure 5.2). The telescope housings are made of aluminum for an optimal strength to mass ratio. Each reflector consists of a substrate also made of aluminum and an epoxy layer that couples the reflecting gold surface to the substrate.

Including the alignment bars, collimating pieces, screws and washers, couplers, retaining plates, housing panels and rings, each XRT consists of over 4000 mechanically separated parts (4112 for XRT-I and 4028 for XRT-S). In total, nearly 7000 qualified reflectors were used and over 1 million cm<sup>2</sup> of gold surface was coated.



Figure 5.2: An Astro-E2 X-Ray Telescope

### 5.1.1 Reflectors

In shape, each reflector is a  $90^\circ$  segment of a section of a cone. The cone angle is designed to be the angle of on-axis incidence for the primary stage and 3 times that for the secondary stage. They are 101.6 mm in slant length and with radii extending approximately from 60 mm at the inner part to 200 mm at the outer part. The reflectors are nominally  $178\ \mu\text{m}$  in thickness. All reflectors are positioned with grooved alignment bars, which hold the foils at their circular edges. There are 13 alignment bars at each face of each quadrant, separated at approximately  $6.4^\circ$  apart.

To properly reflect and focus X-ray at grazing incidence, the precision of the reflector figure and the smoothness of the reflector surface are important aspects. Since polishing of thin reflectors is both impractical and expensive, reflectors in *Astro-E2* XRTs acquire their surface smoothness by a replication technique and their shape by thermo-forming of aluminum. In the replication method, metallic gold is deposited on extrusion glass mandrel (“replication mandrel”), of which the surface has sub-nanometer smoothness over a wide spatial frequency, and the substrate is subsequently bonded with the metallic film with a layer of epoxy. After the epoxy is hardened, the substrate-epoxy-gold film composite can be removed from the glass mandrel and the replica acquires the smoothness of the glass. The replica typically has  $\sim 0.5\ \text{nm}$  rms roughness in the mm or smaller spatial scale, which is sufficient for excellent reflectivity at incident angle less than the critical angle. The *Astro-E2* XRTs are designed with on-axis reflection at less than critical angle, which is approximately inversely proportional to X-ray energy.

In the thermo-forming of the substrate, pre-cut, mechanically rolled aluminum foils are pressed onto a precisely shaped “forming mandrel”, which is not the same as the replication mandrel. The combination is then heated until the aluminum softened. The aluminum foils acquire the figure of the properly shaped mandrel after cooling and release of pressure. In *Astro-E2* XRTs, conical approximation of the Wolter-I type geometry is used. This approximation fundamentally limits the

	XRT-I	XRT-S
Number of Collimators	4	1
Height	32 mm	32 mm
Blade Substrate	Aluminum	Aluminum
Blade Thickness	120 $\mu\text{m}$	120 $\mu\text{m}$
Blade Height	22 mm	22 mm
Height from Blade Top to Reflector Top	30 mm	30 mm
Number of nested shells	175	168
Blade/Telescope	700	672
Mass/Collimator	2.7 kg	2.7 kg

Table 5.2: Design Parameters for Pre-collimator

angle resolution achievable. More significantly, the combination of the figure error in the replication mandrels and the imperfection in the thermo-forming process (to about 4 micrometers in the low frequency components of the figure error in the axial direction) limits the angular resolution to about 1 minute of arc.

### 5.1.2 Pre-collimator

The pre-collimator, which blocks off stray light that otherwise would enter the detector at a larger angle than intended, consists of concentrically nested aluminum foils similar to that of the reflector substrates. They are shorter, 22mm in length, and thinner, 120 micrometers in thickness. They are positioned in a fashion similar to that of the reflectors, by 13 grooved aluminum plates at each circular edge of the pieces. They are installed on top of their respective primary reflectors along the axial direction. Due to their smaller thickness, they do not significantly reduce the entrance aperture in that direction more than the reflectors already do. Pre-collimator foils do not have reflective surfaces (neither front nor back). The relevant dimensions are listed in Table 5.2.

### 5.1.3 Thermal Shields

The *Astro-E2* XRTs are designed to function in a thermal environment of  $20 \pm 7.5^\circ\text{C}$ . The reflectors, due to its composite nature and thus its mismatch in coefficients of thermal expansion, suffer from thermal distortion that degrades the angular resolution of the telescopes in temperature outside this range. Thermal gradient also distorts the telescope in a larger scale. Even though sun shields and other heating elements on the spacecraft help in maintaining a reasonable thermal environment, thermal shields are integrated on top of the pre-collimator stage to provide the needed thermal control.

## 5.2 XRT Performance

Important parameters of the performance of the XRTs include the total effective area and its energy dependence, as well as the angular resolution, field of view, and stray light rejection.

### 5.2.1 Effective Area

The XRTs have a total collective area of more than  $2000 \text{ cm}^2$  at low X-ray energies. The high collecting efficiency of the *Astro-E2* XRTs is made possible by the thin-foil reflectors and a compact

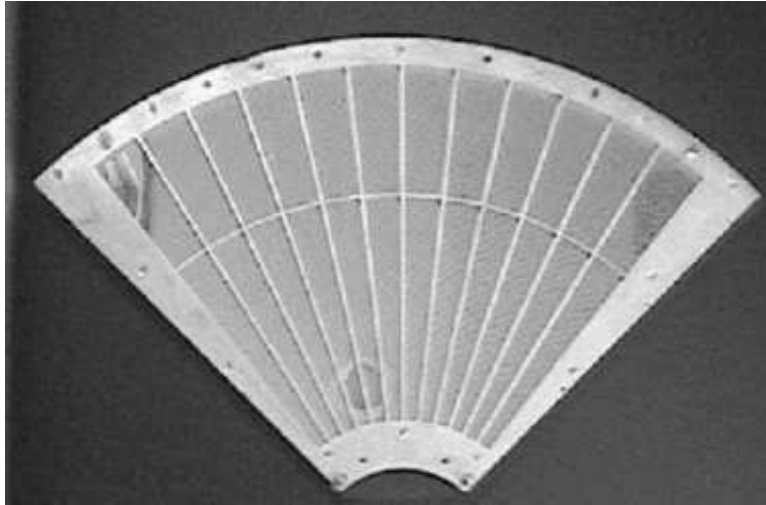
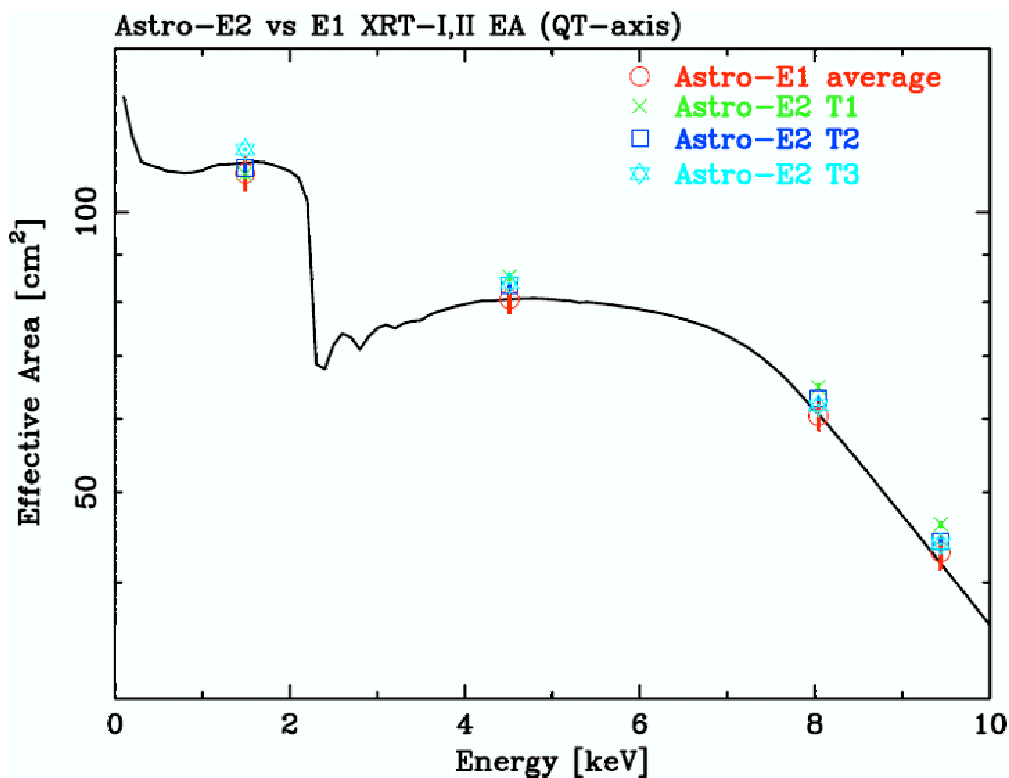


Figure 5.3: A thermal shield.


 Figure 5.4: The predicted effective area of a quadrant of the *Astro-E2* XRT-Is compared to measurements taken at particular energies for three different XRTs.

design. In fact, only  $\sim 20\%$  of the active aperture is lost to the thickness of the reflector themselves. An addition of  $\sim 8\%$  is blocked by the alignment structures (and a smaller fraction to the gap between quadrant housings). Nearly  $900 \text{ cm}^2$  of geometric collecting area for each telescope remains usable for X-ray reflection, from which effective area of typically  $440 \text{ cm}^2$  is obtained at  $1.5 \text{ keV}$  and  $250 \text{ cm}^2$  at  $8 \text{ keV}$ . See Figure 5.4 for a graphical representation of effective area as a function of energy.

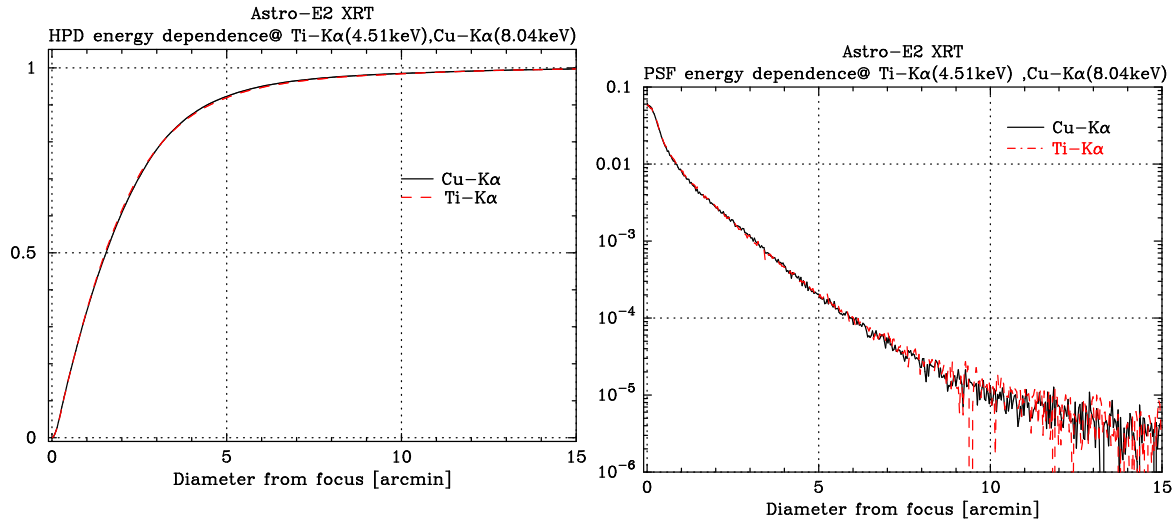


Figure 5.5: (a) Encircled Energy Function at Ti-K (4.5 keV) and Cu-K (8.0 keV). (b) Point Spread Function for the same energies. .

### 5.2.2 Angular Resolution

The angular resolution, traditionally measured in terms of half-power diameter, depends significantly on the proper axial curvature of the reflectors and their proper focusing from the distributed set of reflectors. On the other hand, due to the development of the replication method and its improvement, the micro-roughness is not as significant a factor as the geometric factors, such as slope errors, for resolution degradation. The average value of angular resolution of *Astro-E2* XRTs is about 1.9' (half-power diameter) and is nearly independent of X-ray energy. Half-power diameter is derived from the encircled energy function, which is a function of the total power enclosed within a radius. An example of an encircled energy function and the point spread function are shown in Figure 5.5(a) & (b).

### 5.2.3 Optical Axes

Optical axis is defined as the direction of maximum throughput. It is defined for each quadrant of an XRT and the combination represents that of the telescope. These directions for individual quadrants, by design, are to coincide with the mechanical axis of the telescope system. Any mismatch of optical axes within the telescope or mismatch of the combined direction to that of the mechanical axis will lower the throughput for on-axis sources. However, the image position on the detector will not shift due to the nature of double reflections. The optical axes of individual quadrants were adjusted during quadrant integration and are generally within  $\pm 1'$  of the nominal direction.

### 5.2.4 Focal Length

Focal length is defined as the distance of the image plane at which the image is most concentrated (having the smallest half-power diameter, for example). It is defined for individual quadrants and their combination represents the overall performance for an XRT. (For individual quadrant, it can also be measured effectively as the distance at which the image is symmetrical about the image center.) Focal length is "built-in" at the quadrant level and cannot be adjusted once the quadrant is built. The error in focal length of the quadrants in an XRT thus manifests itself in the degradation of the angular resolution, since the image plane is fixed at the detector position. Error in focal

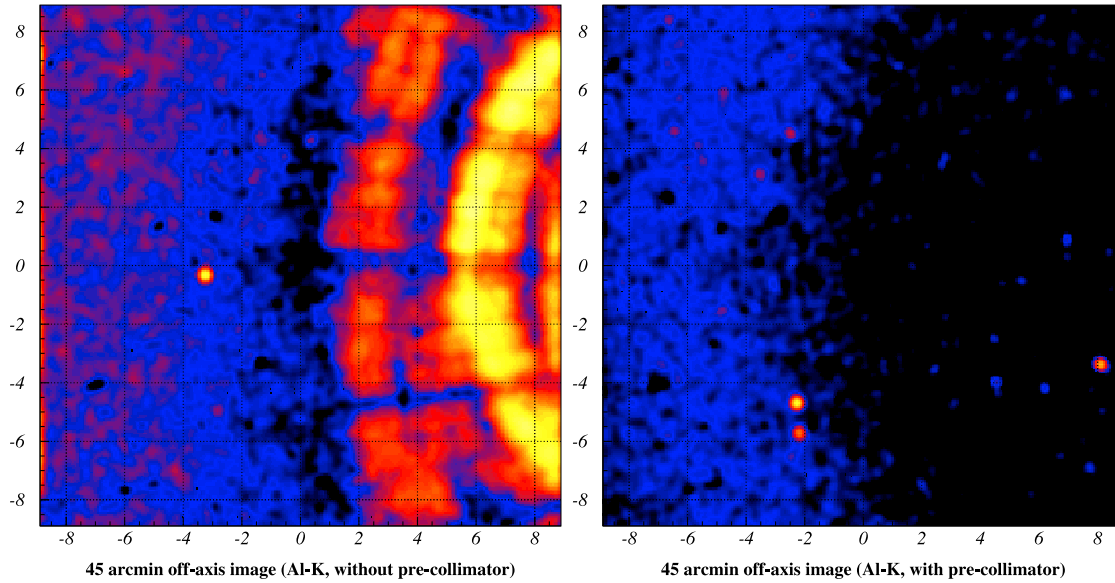


Figure 5.6: Stray light images of the spare quadrant in the field of view of the XIS at 45' off axis. The [Left] and [Right] panels correspond to the images at Al-K (1.49 keV) before and after the pre-collimator installation, respectively. In each panel the right side is dominated by a stray light component from “secondary-only reflection” while the left side is by dominated by “backside reflection.” The stray flux is reduced by two orders of magnitude after the pre-collimator installation. The small filled circles in both images are identified as background particles, *i.e.*, cosmic rays.

length is intimately related to that of the angular resolution and it is primarily affected by the relative error of reflector positioning at the 2 edges of the reflectors. It also has dependence on the location of reflectors (inner vs. outer). For the *Astro-E2* XRTs, the focal lengths are typically within several cm of the nominal values. The angular resolution shown in §5.2.2 was measured at nominal focal distance and thus has already absorbed the error of focal length.

### 5.2.5 Field of View and Stray Light

Off-axis X-rays far out the field of view may not follow the intended light path but still enter the detector. Such ghost image can come from single reflection at the secondary stage, or it may be formed after making a backside reflection at the primary reflector, even though the backside of a reflector is not very reflective. To eliminate such stray light from entering the detector, a set of collimating blades is used to block off large angle reflection. Figure 5.6 shows an example of the elimination of stray light with the collimator action.

## Chapter 6

# X-ray Spectrometer (XRS)

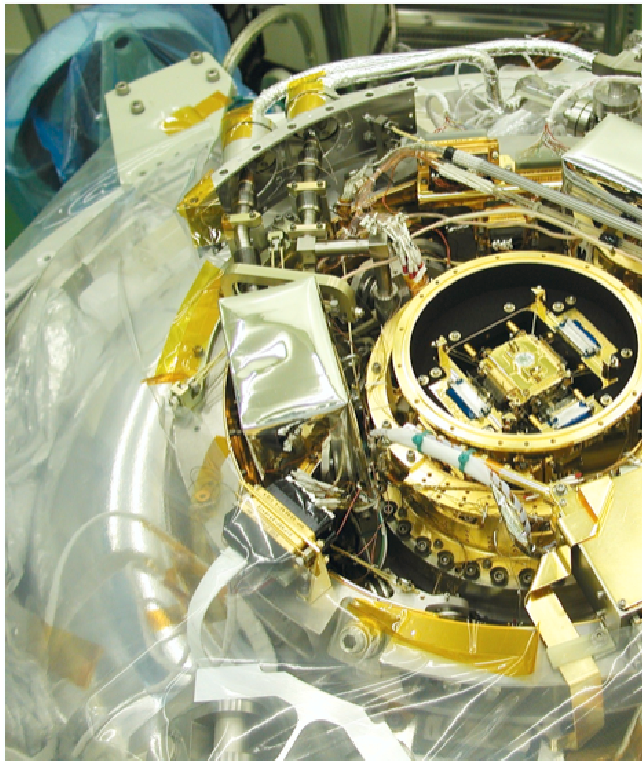


Figure 6.1: The *Astro-E2* XRS in the lab.

The XRS, shown in Figure 6.1, is the prime instrument onboard the *Astro-E2* satellite, providing high resolution X-ray spectra for cosmic sources simultaneously over a broad range of energies,  $\sim 0.3$  to 12 keV, at an unprecedented energy resolution of 6 – 7 eV (FWHM) with very good efficiency. It was constructed jointly by NASA/GSFC and ISAS/JAXA, based on principles of operation developed at NASA/GSFC and the University of Wisconsin. The XRS works by measuring the temperature difference resulting from an absorption of a photon, and thus it is a “microcalorimeter” (cf. Fig. 6.3). It will be the first such instrument flown on an orbiting observatory. While in principle it is a simple instrument, the details are complicated, as the sensors must be maintained at a precisely regulated cryogenic temperature. The X-ray sensors themselves, the signal processing electronics, the Adiabatic Demagnetization Refrigerator (ADR), and the liquid helium cryostat are supplied by GSFC. The cryogenic dewar, including the solid neon tank surrounding the helium



tank, and the mechanical cooler, was built by ISAS and Sumitomo Heavy Industries in Japan, and the Filter Wheel was developed mainly at Tokyo Metropolitan University.

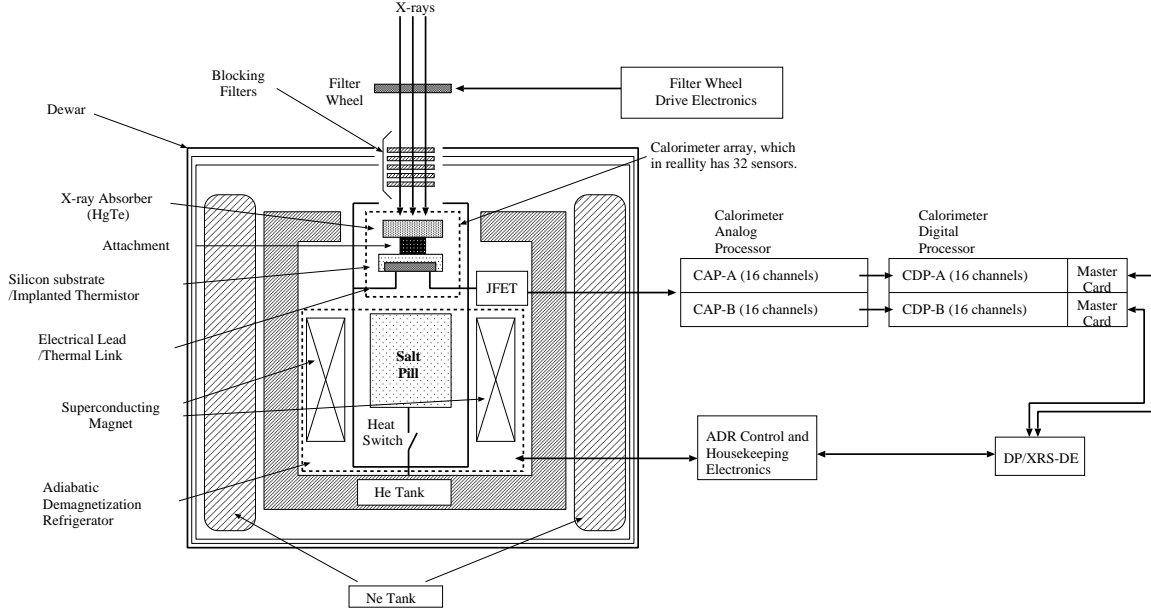


Figure 6.2: A schematic diagram of the entire XRS instrument, showing the main subsystems.

## 6.1 Principles of Operation of the XRS Detector

The determination of the energy of the incident photon  $E_{\text{ph}}$  is accomplished by measuring the temperature rise  $\Delta T$  (assumed to be much smaller than the heat sink temperature  $T$ ) associated with its absorption. Schematically, the detector is illustrated in Fig. 6.2; it consists of a monolithic, etched silicon structure formed into an array of  $6 \times 6$  pixels on a  $0.64 \text{ mm} \times 0.64 \text{ mm}$  grid. Only 30 of the 36 possible pixels in the grid are used as detectors<sup>1</sup>. Each pixel consists of an etched silicon square with implanted thermistor with an absorber glued on top. The silicon thermistor is isolated from the heat sink by four etched silicon beams. The absorber is  $\sim 10 \mu\text{m}$  above the plane of the silicon, and extends beyond the edges of the silicon beams.

The absorber size is  $0.624 \text{ mm} \times 0.624 \text{ mm}$ . If the thermal conductance between the thermistor and heat sink is  $G$ , and the heat capacity of the detector is  $C$ , then absorption of a photon with energy  $E_{\text{ph}}$  results in  $\Delta T$  given by

$$\Delta T = E_{\text{ph}}/C$$

and the detector returns to the heat sink temperature with a time constant

$$\tau = C/G.$$

The rise time of the temperature is  $\sim 0.7 - 0.8 \text{ ms}$ , and the  $1/e$  fall time is about  $3.5 \text{ ms}$ , which determines the throughput as a function of the counting rate (see Sec. 2.3 and below).

The fundamental limit on the energy resolution of the detector is determined by the random transport of phonons between the detector and the thermal bath in the link connecting them and by the bandwidth of the measurement. For an ideal calorimeter with a resistive thermometer, this bandwidth is set by the Johnson noise. This is because the signal and phonon noise (which have the

<sup>1</sup>Originally 31 pixels were available for imaging. During testing in March 2004, the JFET for the calibration pixel failed and the JFET from pixel 3 in the imaging array was used to replace it.



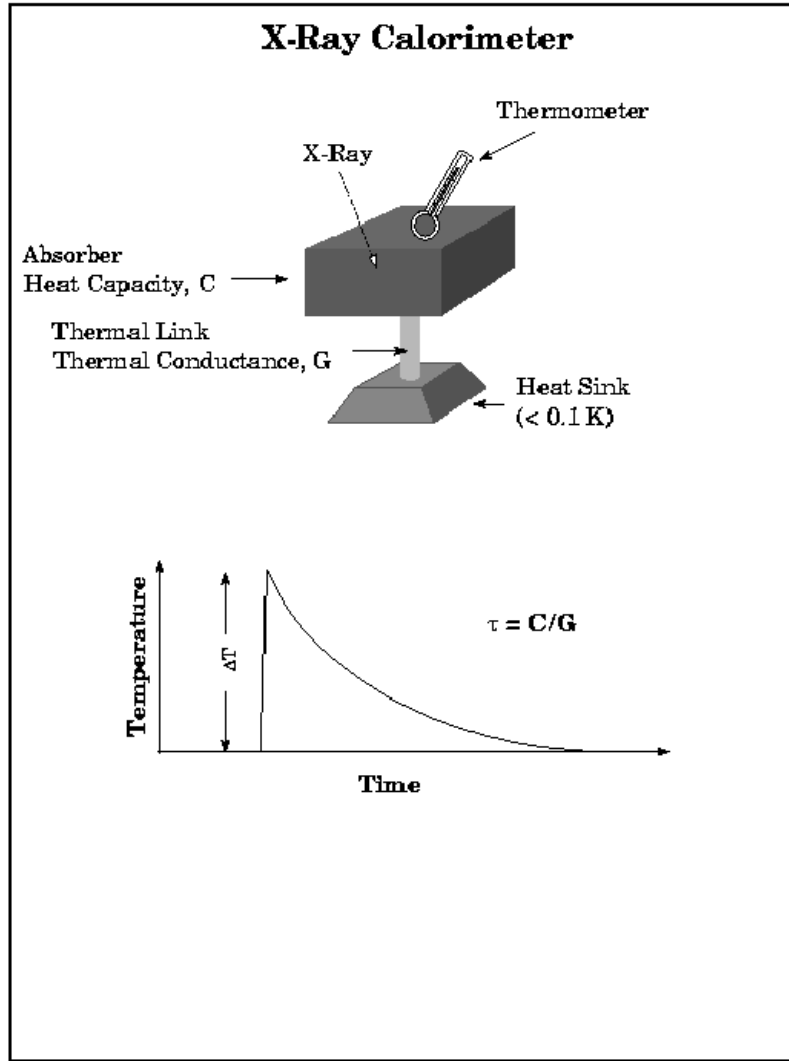


Figure 6.3: Principle of operation of the XRS. The deposited photon energy  $E_{\text{ph}}$  creates a temperature rise  $\Delta T = E_{\text{ph}}/C$ , where  $C$  is the heat capacity of the pixel. The pulse subsequently decays with the time constant  $\tau$  of about  $C/G$ , where  $G$  is the thermal conductance of the pixel supports.

same frequency dependence) fall relative to the Johnson noise at high frequencies. For a detector of heat capacity  $C$ , operating at the bath (heat sink) temperature  $T$ , the limiting FWHM energy resolution is

$$\Delta E = 2.35\eta(kT^2C)^{1/2},$$

where  $k$  is the Boltzman's constant. The variable  $\eta$  is dependent on the design of the thermometer, and for XRS-like thermometers is of the order of 2. The XRS design uses an optimal filter technique, which requires multiple sampling of the pulse and weighted averaging of the samples over a time interval spanning several time constants. Since this must be done without an adjacent pulse present in the time series, this, in turn, sets the maximum counting rate.

The thermometers in the XRS detectors are resistive, operating on the principle of phonon-

assisted electron hopping conduction, where the conductivity rises rapidly with an increase in temperature. In such a thermometer the resistance  $R$  depends on temperature  $T$  such that

$$R = R_0 \exp((T_0/T)^{1/2}).$$

These thermometers are ion-implanted into the individual pixels, and the contacts to the thermometer are brought out by conductive traces. The thermometer is biased at an approximately constant current via a voltage divider, and the increase in the temperature will appear as a change of voltage across it. The thermometers under bias have a resistance of the order of 30 M $\Omega$ . The voltage across each thermometer is applied to the gate of a JFET source follower amplifier, with an output impedance of  $\sim 2000\Omega$ . The JFET amplifiers are housed in a separate enclosure, since silicon JFETs need to operate at temperatures  $\sim 130$  K for the lowest noise, and thus need to be thermally isolated from the detectors and the ADR. The signal is subsequently sent to the Calorimeter Analog Processor (CAP). The CAP provides power to the detectors and further amplifies the signals (by a factor of 20,000). The CAP has 32 channels, each of which handles data from a single calorimeter pixel.

The energy resolution of the detector improves with decreasing heat capacity of the materials chosen for the substrate and for the absorber, and thus one of the challenges of the design is to find material of the lowest possible heat capacity that is sufficiently opaque to X-rays. Many materials, including silicon, the material used for the detector structure, have extremely low heat capacities at low temperatures. However, silicon is not suitable for X-ray absorption, since the large electronic bandgap allows many long-lived trap sites for the electrons, precluding rapid and efficient conversion of the X-ray to thermal energy. Thus, a separate absorber is needed. For the XRS, mercury telluride (HgTe) was chosen as the absorber, providing a relatively large opacity to X-rays with a relatively low heat capacity. The thickness of the absorber is  $\sim 8.0$   $\mu\text{m}$ ; this will stop 95% of 6 keV X-rays and achieve an energy resolution of 6 – 7 eV at 60 mK. The drop in the efficiency of the XRS at high energies is due to the absorber becoming transparent.

## 6.2 Details of the XRS Design

### 6.2.1 XRS Cryogenic System

In addition to the need to keep the heat capacity of the absorber to the minimum, the XRS must operate at a low temperature to minimize the phonon noise and maximize the sensitivity of the resistive thermometer. To achieve the required energy resolution ( $\sim 6$  eV FWHM) with the required detector size implies that the operating temperature must be below 0.1 K. For the XRS, there are four stages of cooling. The primary source of cooling is a 130 liter solid neon dewar. The life of the neon is extended by the use of a mechanical cooler which cools the outer radiation shield of the dewar. The solid neon maintains a temperature of  $\sim 17$  K, and surrounds a  $\sim 32$  liter tank filled with liquid helium. The liquid helium is vented to space, and maintains a temperature of  $\sim 1.3$  K. The final stage of cooling is accomplished via the use of an adiabatic demagnetization refrigerator (ADR). This allows operation down to 50 mK; for the XRS, the nominal operating temperature will be 60 mK. Accurate temperature regulation is crucial, as the detector response depends directly on its temperature. A change in temperature results in a corresponding change in the energy scale calibration. **Therefore the ADR is specified to maintain the temperature to better than 10  $\mu\text{K}$  rms over a 10s to 10min timescale.** Longer term temperature drifts are accounted for by a dedicated calibration pixel. Temperature control is accomplished by adjusting the magnetic field via a feedback loop. The expected lifetime of the on-board cryogens is  $\sim 2.5$  years. This corresponds to operating the cooler 50% of the time; a slightly longer lifetime is expected if the cooler can operate at all times.

The ADR operates by aligning the magnetic moments (electron spins) of the molecules in the salt pill with a superconducting magnet, running at  $\sim 2$  A and providing a magnetic field of  $\sim 2$  Tesla. At the start of a cycle, the magnet is ramped up to a full field and the salt pill is connected to the liquid helium bath via a gas-gap heat switch, transferring the heat to the liquid helium bath. Once the salt pill has reached an equilibrium, the heat switch is opened, and at this point the magnetic field is reduced to nearly zero. This allows the spins of the electrons in the salt molecules to randomize adiabatically, causing the salt to cool as they do. It is expected that the *Astro-E2* ADR can maintain the 60 mK temperature while in orbit for  $\sim 1$  day, at which point the magnetic spins are completely randomized, and no more heat can be absorbed. At this point, a “recharge” of the refrigerator is necessary, and the cycle is started again. The “recharge” of the refrigerator, typically lasting  $\sim 1$  hour, can be done partially while the observed astrophysical target is behind the Earth.

### 6.2.2 XRS blocking filters

The XRS detectors must be kept at their operating temperature, so they have to be shielded from the ambient radiation field (even deep space is warmer than the operating XRS detectors!). More significantly, the Poisson noise associated with the discrete nature of ambient photons would appear as additional noise in the signal detected from individual X-rays; from a practical standpoint, it is also necessary to keep the heat load on the cryogenic system to a minimum. To prevent this, the calorimeter pixels are shielded from the ambient radiation field via a set of blocking filters, located in the field of view of the detectors. These filters have to be sufficiently thick to block (either by absorbing or reflecting) infrared radiation from the spacecraft and the dewar as well as geocoronal UV, while allowing for good transmission of X-rays. The XRS employs five blocking filters made of thin films of aluminized polyimide. From the outside to inside, these are located on the Dewar Main Shell (DMS), on the Inner Vapor Cooled Shield (IVCS), at the Neon tank, on the outside of the Calorimeter Front End Assembly (FEA), and on the Calorimeter Thermal Sink (CTS) (on the lid of the detector box). The filter transmission determines the lowest observable energy by the XRS. It is expected that the XRS filters will allow throughput down to  $\sim 0.3$  keV.

### 6.2.3 XRS Filter Wheel and In-flight Calibration

As discussed above, the XRS detectors require a relatively long time after an absorption event to recover for the next event. In addition, as noted in §4.5, sufficiently bright sources will cause the XRS resolution to degrade. This is due to X-rays hitting the silicon frame outside of the pixels and thermal crosstalk from other pixels which is a source of noise that at very high incident flux begins to degrade the XRS resolution in the Hi-res and Mid-res grade events. For an observation of a point source, we project that the resolution will degrade to  $\sim 10$  eV for source fluxes  $F(0.3-12 \text{ keV}) \sim 10^{-8} \text{ ergs/s/cm}^2$ . Therefore, to observe bright sources with the XRS while avoiding event pile-up the X-ray flux must be reduced.

This can be accomplished with the Filter Wheel, a circular plate made of aluminum with six mounting positions for the filter elements. As summarized in Table 6.1, two positions (position # 1 and # 2) out of the six remain open, another two (# 3 and # 4) are filled with  $300\mu\text{m}$  thick Beryllium (Be) filters, and the other two (# 5 and # 6) are provided with Neutral Density (ND) filters which are made of a  $200 \mu\text{m}$  thick molybdenum plate with 1802 small pin-holes, and have nominal transmission of 10 %.

In order to monitor the calibration of the XRS detector in orbit, we have attached  $^{55}\text{Fe}$  isotopes for the positions # 1, # 3 and # 5 at the center of the filter elements. In addition, we have further equipped the open position already having the  $^{55}\text{Fe}$  isotope with a  $^{41}\text{Ca}$  isotope at the end of the

Position	1	2	3	4	5	6
Filter	Open	Open	Be 300 $\mu\text{m}$	Be 300 $\mu\text{m}$	ND 10 %	ND 10 %
Cal Source	—	$^{55}\text{Fe}$ , $^{41}\text{Ca}$	—	$^{55}\text{Fe}$	—	$^{55}\text{Fe}$

Table 6.1: Filter Element and Calibration Source on Filter Wheel

mounting position, for calibrating the energy-dependence of the XRS gain. The expected intensity is 0.1–0.2 cps/pixel for  $^{55}\text{Fe}$  and  $\sim 0.1$  cps/XRS for  $^{41}\text{Ca}$ . The introduction of these Filter Wheel calibration sources is one of the changes from *Astro-E*.

The effect of these filters on the effective area of the XRS is shown in Fig. 2.3. Regarding the types of sources for which the filter wheel may be needed, we note again that except for the Crab nebula, there are no known diffuse sources, such as clusters of galaxies or supernova remnants which need the filter wheel; it may be needed for the bright Galactic binaries with a flux in excess of  $\sim 50$  milliCrab (cf. Figs. 2.10 and 2.11).

#### 6.2.4 In-flight gain-tracking of the XRS

The XRS includes an on-board calibration pixel to track variations in the gain, which could be caused by a drift in the temperature of the detector heat sink. Unlike the calibration sources on the filter wheel (which are too weak to be effective for this purpose), this pixel is not in the field of view. The calibration pixel is offset several millimeters from the imaging array, and is illuminated by a collimated  $^{55}\text{Fe}$  source. The decay of  $^{55}\text{Fe}$  to  $^{55}\text{Mn}$  produces 5.899 and 5.88 keV ( $K\alpha_1$  and  $K\alpha_2$ ) and 6.490 keV ( $K\beta$ ) lines (with a half-life of 2.73 years). The count rate on the calibration pixel will be  $\sim 4.5$  counts per second at launch, falling to  $\sim 2.4$  after the nominal 2.5 year mission lifetime. Again, it is important to note that the imaging portion of the array is not illuminated at all by this internal calibration source.

The pulse height data from the calibration pixel (collected whenever the detector is on) will be used to create the XRS gain history files. It is anticipated that an absolute determination of the energy of a narrow monochromatic line (at energies below  $\sim 7$  keV) can be made with a precision of  $\lesssim 2$  eV.

### 6.3 On-board Signal Processing in the XRS

The analog signals from the detectors, amplified by the CAP, are sent to the Calorimeter Digital Processor (CDP) for processing. Both analog and digital signal processing chains are split into two independent 16-channel sides. Each channel of the CDP consists of a low-pass antialiasing filter, analog-to-digital (A/D) converter and a Digital Signal Processor (DSP). The antialiasing filter cuts off frequencies above 2 kHz. The A/D part of the DSP samples and digitizes the data at a rate of 12288 Hz with 14-bit resolution. For High Resolution events (see the next section), 2048 samples are required to analyze a single pixel. Therefore, the amount of raw data in a single pulse is 2048 samples  $\times$  14 bits/sample = 28672 bits. The DSP determines the pulse height and arrival time, and outputs a digital event packet. A single event packet is 64 bits in length, which compares favorably to the amount of the raw data. Parenthetically, the default telemetry limit for the XRS is 10240 bits/sec, which corresponds to about 160 events/s/array, or an average of 5 events/s/pixel. The data stream is compressed before transmission, so the exact maximum count rate will depend on the data itself. It should be noted that in addition to this telemetry limit, above this count rate the energy resolution will degrade due to pileup effects. Independently, the XRS has an inherent hardware limit on the counting rate of 50 counts/s/pixel; counts in excess of this limit are simply

discarded. Note that there are no user-specified parameters for the XRS, except for the setting of the filter wheel.

### 6.3.1 Searching for X-ray events

In order to provide the X-ray event data to the telemetry, the DSP has to detect the presence of X-ray pulses in the data stream. To do this, the DSP calculates a smoothed derivative of the data. The initial pulses are detected when the derivative exceeds a fixed threshold. An additional task of the DSP is to find secondary events which might be superposed on the tails of the initial pulses. If a secondary pulse is not recognized as such, this may affect the determination of the pulse heights of the initial pulses. Hence it is important for the DSP to detect secondary pulses even if they are much smaller than the initial pulses.

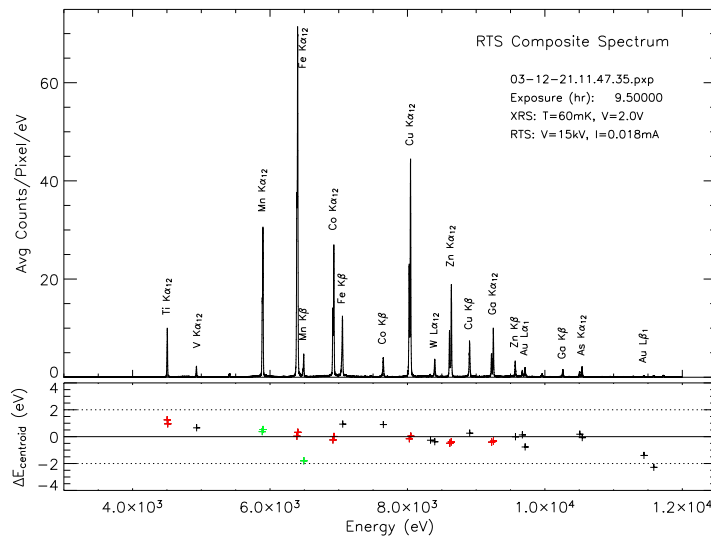


Figure 6.4: Calibration spectrum from the XRS flight detector array showing the resolution and centroiding for emission lines between 4.5–12 keV.

To search for secondary pulses, the DSP/CDP compares the smoothed derivative with a template of the single-pulse derivative shape stored in the CDP. The derivative shape template is subtracted from the measured derivative by scaling the peak values to form the *adjusted derivative*. If the adjusted derivative rises above a threshold and then falls below within a specified length of time, a secondary pulse is detected. The secondary pulses are flagged so that they can be discriminated from initial pulses.

Once an initial pulse has been detected, the CDP begins counting down the length of a *Hi-resolution* data record (2048 samples). If the pulse count reaches zero without detecting any secondary pulses during  $2048/12288=167$  msec, the event is flagged as a *Hi-res* record (see Fig. 6.5 and the next section). If a secondary pulse does occur, the initial (primary) pulse will be processed and flagged as either a *Mid-res* or *Low-res* event, and the counter will reset to the full Hi-res length. The secondary pulse will then be graded as well. As noted below, Mid-res secondary pulses have lower energy resolution than Mid-res primary events.

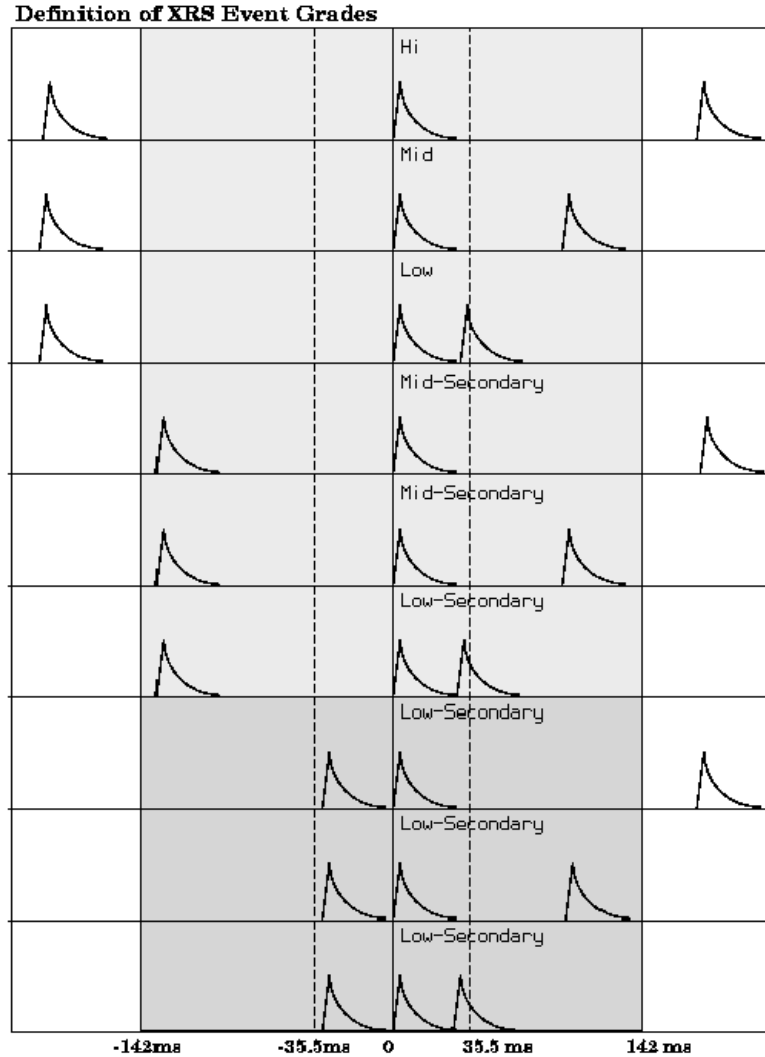


Figure 6.5: Diagram showing the event grade determination in the XRS data processing chain.

### 6.3.2 Pulse Height Determination:

The main task for the CDP is to get the best possible estimate of the height of each pulse. The zeroth-order estimate of the pulse height is the peak value of the pulse minus the baseline value, but this is not a good measure because of noise. In order to determine the pulse height value as precisely as possible using all the samples in the pulse, the XRS uses the *optimal filtering* technique. In this technique, noise is reduced by weighted averaging of all the samples in the pulse. This requires an accurate template of a “clean” pulse. The Hi-res grade applies only when there is only a single pulse in the block of 2048 samples.

To create the optimal filter, the average pulse (2048 samples in 167 msec) is Fourier transformed and in Fourier space the pulse is divided by the power spectrum of the noise. Finally the result is inverse Fourier transformed to create the Hi-res template. In order to estimate the noise power spectrum, a relatively large number (100–200) of individual noise power spectra, each of which

is made from a single noise record of 2048 samples, are averaged. The average pulse is made by averaging similar pulses which fall in a limited range on the pulse-height vs rise-time plane. The optimal filtering template for the Hi-res grade thus has 2048 samples in time space. The *optimal pulse height* is calculated by multiplying the data and optimal filter sample-by-sample and adding them up. This procedure cancels out the interference of the noise component in the pulse.

The above method of pulse-height calculation cannot be used when there are two or more events in the train of 2048 samples. If two pulses are closer than 2048 samples but not “too close,” a shorter optimal filtering template, typically 512 samples long, is used (see Fig. 6.5). This method of pulse height calculation is called *Mid-res* grade. In general, shorter templates are less effective in determining and rejecting the interference of noise at particular frequencies. In the absence of noise induced externally (such as microphonics or 60 Hz interference) the Mid-res primary pulses will give approximately the same resolution as the Hi-res grade.

When pulses are too close even for the Mid-res grade, pulse heights are determined simply measuring the heights of the peak over the baseline level; these are the *Low-res* grade. The baseline and the magnitude of the peak are measured by taking an average of typically eight samples.

Each XRS event has flags indicating which of the three methods of pulse height determination was used. Hi-res events provide a resolution that is limited by the detector and amplifier electronics, and this has been as good as 5 eV (FWHM) at 1 keV. In the absence of noise, the Mid-res grade (primary events only) provides better than 6 eV resolution at 1 keV. The Low-res grade gives a resolution around 30 eV. Mid-res secondary events have a large low-energy tail which reduces their resolution significantly relative to Mid-res primary events. These secondary events require a post-processing correction that is still under development, which could restore most of the lost energy resolution. However, for AO-1, we encourage proposers to exclude secondary events from their simulations. The relative fraction of events in the Hi-, Mid-, and Low-res grades as a function of the XRS counting rate (per pixel) are given in Fig. 2.11.

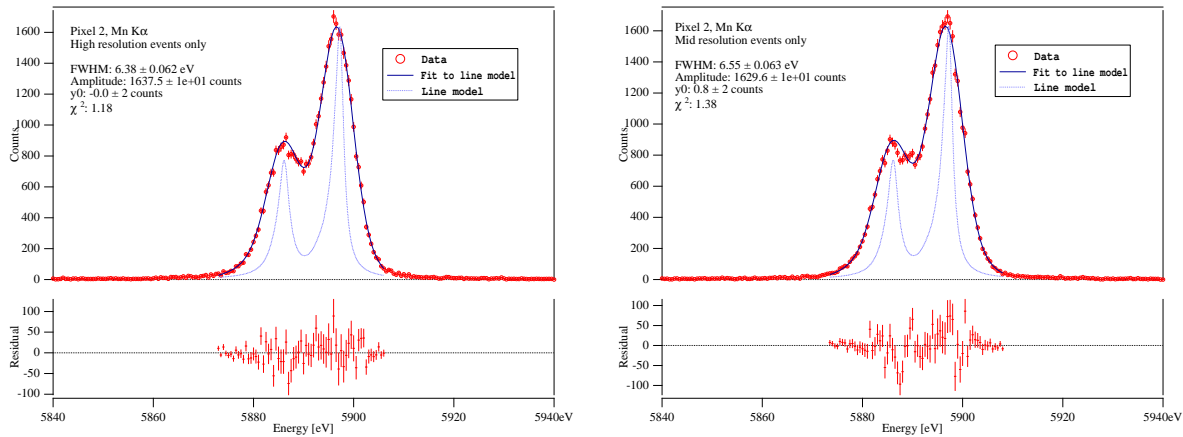


Figure 6.6: [Left] XRS spectral resolution at Mg K $\alpha$  using Hi-res events only. [Right] The same plot using Mid-res (primary) events only.

Figure 6.6 shows the effective resolution of both Hi- and Mid-res primary events, using data taken from Mg K $\alpha$  lines at 5.8876 and 5.8988 keV. The XRS line shape is very nearly Gaussian, as can be seen in Figure 6.7. Unlike grating spectrometers the line shape is determined by the XRS detector itself, and is totally independent of the X-ray mirror. Although Fig. 6.6 shows results only from pixel 2 and Fig. 6.7 is from pixel 5, the pixels in the XRS array are quite uniform with the exception of two pixels. For 28 of the pixels, the resolution is only slightly energy dependent, 5.5–6 eV at low ( $< 1$  keV) energies and rising slowly to about 6–7 eV at 6 keV. Two pixels, #11

Pixel	$E < \sim 1 \text{ keV}$	$E = 3.3 \text{ keV}$	$E = 6 \text{ keV}$
11	$\sim 5.5 \text{ eV}$	$\sim 7 \text{ eV}$	8 eV
20	$\sim 5.5 \text{ eV}$	$\sim 10 \text{ eV}$	14 eV
others	$\sim 5.5 \text{ eV}$	$\sim 6 \text{ eV}$	$\sim 6.5 \text{ eV}$

Table 6.2: The energy-dependence of XRS pixels;  $1\sigma$  measurement uncertainties are 0.3 eV. Note that the two unusual pixels are on the perimeter of the array and should have minimal impact on most observations.

and #20 (see Fig. 2.5) have an energy that is much more energy dependent, as shown in Table 6.2. The energy resolution of these two pixels is not included in the proposal response matrix. However, after in-flight calibration is complete, it is expected that response matrices will be available for individual pixels as needed.

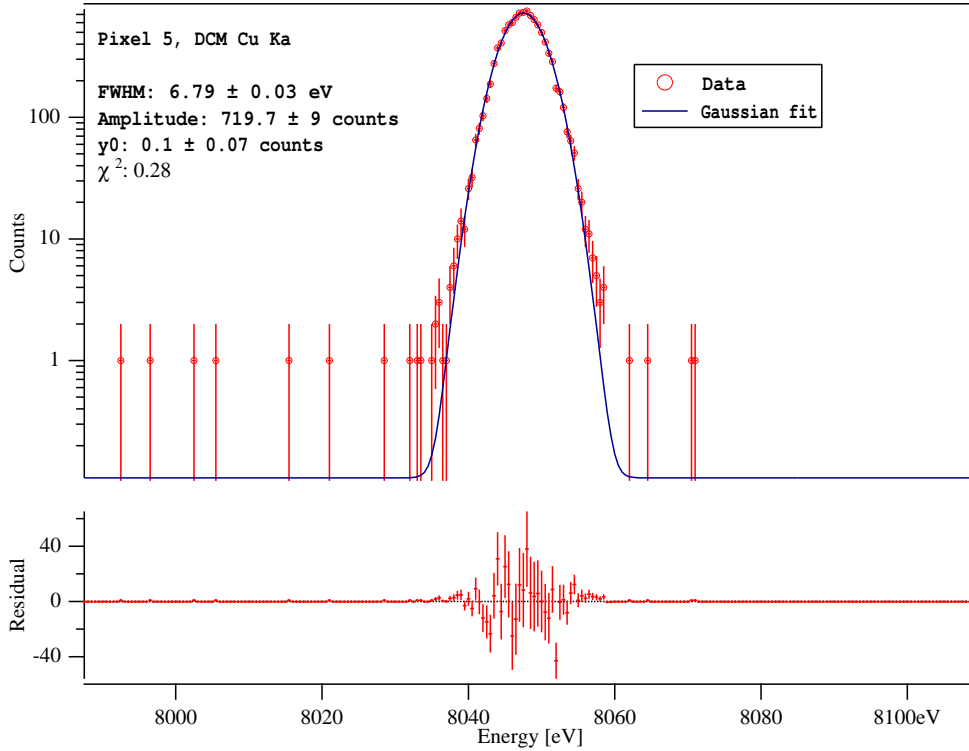


Figure 6.7: XRS measurement of Cu K $\alpha$  emission line on a logarithmic scale compared to a simple Gaussian fit.

### 6.3.3 XRS Timing Accuracy

Each event time is reconstructed from a number of intermediate values, and represents Coordinated Universal Time (UTC) at the spacecraft when the photon was absorbed. The absolute time accuracy will be  $\sim 100\mu\text{s}$ , a limit set by the spacecraft clock and electronics in the XRS. The relative timing accuracy within a single observation should be  $\sim 10\mu\text{s}$ . However, there may be a statistically significant (10s of  $\mu\text{s}$ ) systematic error in time-tagging as a function of photon energy, so proposers should assume the timing accuracies of  $\sim 100\mu\text{s}$ .



## 6.4 XRS Background

While the XRS is physically a small detector, it can still be subject to background events. Most likely the strongest contribution will be from energetic protons depositing some of their energy in the XRS. The planned *Astro-E2* orbit is quite similar to ASCA's, so the particle background also should be similar. Outside of the SAA the background rate in the ASCA SIS was roughly  $1 \text{ count cm}^{-2} \text{ s}^{-1}$ . With this, and given the expected proton spectrum, it is expected that the XRS may experience as many as  $4 \times 10^{-3} \text{ counts s}^{-1}$  per pixel, with  $\sim 60\%$  depositing more than 10 keV. While this is still a low rate, the XRS features an anti-coincidence detector for an added insurance against sudden increases in flux (and, possibly, allowing the data acquired during the SAA passages to be usable). To be useful, this device has to be located close to the XRS, and so it has to operate below 0.1 K. The XRS anti-coincidence detector is a  $1 \text{ cm}^2$ , 0.5 mm thick ionization detector made of doped Si, and placed directly behind the XRS array. The device is configured as a PIN diode operating in a reverse bias configuration (although at these low temperatures such a diode acts essentially as a capacitor).

Simulations with the high-energy physics tool GEANT4 show that the anti-coincidence detector will be triggered by 98% of the particles which pass through a pixel. In addition, because the particles which miss the anti-coincidence detector are mostly those which pass through the X-ray pixels at a steep angle, 90% of them will deposit more than 10 keV in the pixel, and will thus be rejectable strictly on an energy basis. Thus our total unrejected particle background is 0.2% of the particle rate. Individual events from the anti-coincidence detector are not telemetered to the ground, but XRS X-ray events that were recorded within a set time window of the anti-coincidence event are flagged "ANTICO." In addition, one can use the timing information to reject events that occurred nearly-simultaneously in multiple adjacent pixels (the so-called "pixel-to-pixel" events), as those are likely to be particle-induced. One-minute totals of the number of anti-coincidence detector events are also telemetered to the ground.

The expected performance of the anti-coincidence detector suggests that the background should be dominated by secondary particles (*i.e.* electrons and photons). In combination with our knowledge of the ASCA unrejected background, we expect this to be a few counts/pixel/day.

## Chapter 7

# X-ray Imaging Spectrometer (XIS)

### 7.1 Overview of the XIS

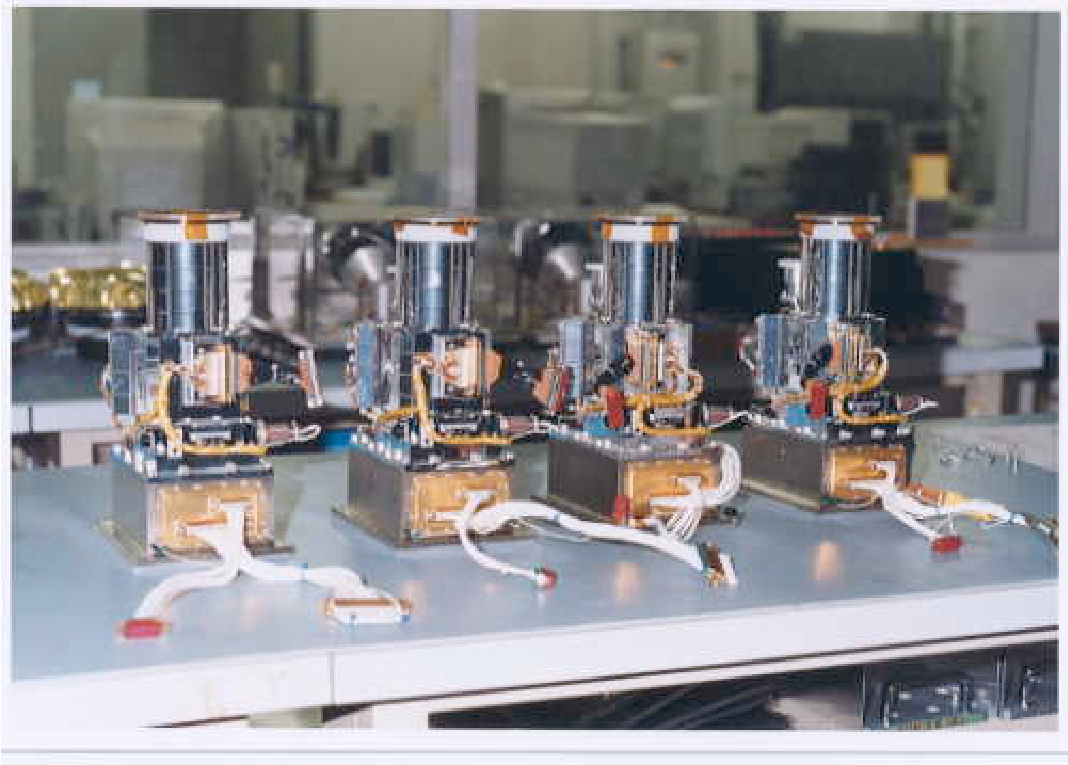


Figure 7.1: The four XIS detectors before installation onto *Astro-E2*.

*Astro-E2* will contain four XIS instruments, shown in Figure 7.1. These employ X-ray sensitive silicon charge-coupled devices (CCDs), which are operated in a photon-counting mode, similar to that used in the ASCA SIS, *Chandra* ACIS, and *XMM-Newton* EPIC. In general, X-ray CCDs operate by converting an incident X-ray photon into a charge cloud, with the magnitude of charge proportional to the energy of the absorbed X-ray. This charge is then shifted out onto the gate of an output transistor via an application of time-varying electrical potential. This results in a voltage level (often referred to as “pulse height”) proportional to the energy of the X-ray photon.

The four *Astro-E2* XISs are named XIS-S0, S1, S2 and S3, each located in the focal plane of an X-ray Telescope; those telescopes are known respectively as XRT-I0, XRT-I1, XRT-I2, and

XRT-I3. Each CCD camera has a single CCD chip with an array of  $1024 \times 1024$  picture elements (“pixels”), and covers an  $18' \times 18'$  region on the sky. Each pixel is  $24 \mu\text{m}$  square, and the size of the CCD is  $25 \text{ mm} \times 25 \text{ mm}$ . Two of the XISs are equipped with back-side illuminated CCDs, and other two use front-side illuminated CCDs. The XIS has been partially developed at MIT (CCD sensors, analog electronics, thermo-electric coolers, and temperature control electronics), while the digital electronics and a part of the sensor housing were developed in Japan, jointly by Kyoto Univ., Osaka Univ., Rikkyo Univ., Ehime Univ., and ISAS.

A CCD has a gate structure on one surface to transfer the charge packets to the readout gate. The surface of the chip with the gate structure is called the “front side”. A front-side illuminated CCD (FI CCD) detects X-ray photons that pass through its gate structures, i.e. from the front side. Because of the additional photo-electric absorption at the gate structure, the low-energy quantum detection efficiency (QDE) of the FI CCD is rather limited. Conversely, a back-side illuminated CCD (BI CCD) receives photons from “back,” or the side without the gate structures. For this purpose, the undepleted layer of the CCD is completely removed in the BI CCD, and a thin layer to enhance the electron collection efficiency is added in the back surface. A BI CCD retains a high QDE even in sub-keV energy band because of the absence of gate structure on the photon-detection side. However, a BI CCD tends to have a slightly thinner depletion layer, and the QDE is a little worse in the high energy band. To balance these effects, two of the XISs use BI CCDs and others use FI CCDs. As of writing this document, it is not determined which XISs will have the BI CCDs.

To minimize the thermal noise, the sensors need to be kept at  $\sim -90^\circ\text{C}$  during observations. This is accomplished by thermo-electric coolers (TECs), controlled by TEC Control Electronics, or TCE. The Analog Electronics (AE) drives the CCD clocks, reads and amplifies the data from the CCDs, performs the analog-to-digital conversion, and routes the signals to the Digital Electronics (DE). The AE and TCE are located in the same housing, and together, they are called the AE/TCE. *Astro-E2* has two AE/TCEs; AE/TCE01 is used for XIS-S0 and S1, and AE/TCE23 is used for XIS-S2 and S3. The digital electronics system for the XISs consists of two Pixel Processing Units (PPU) and one Main Processing Unit (MPU); PPU01 is associated with AE/TCE01, and PPU23 is associated with AE/TCE23. The PPUs receive the raw data from AE, carry out event detection, and send event data to the MPU. The MPU edits and packets the event data, and sends them to the satellite’s main digital processor.

To reduce contamination of the X-ray signal by optical and UV light, each XIS has an Optical Blocking Filter (OBF) located in front of it. The OBF is made of polyimide with a thickness of  $1000 \text{ \AA}$ , coated with a total of  $1200 \text{ \AA}$  of aluminum ( $400 \text{ \AA}$  on one side and  $800 \text{ \AA}$  on the other side). To facilitate the in-flight calibration of the XISs, each CCD sensor has two  $^{55}\text{Fe}$  calibration sources. One is installed on the door to illuminate the whole chip, while the other is located on the side wall of the housing to illuminate two corners of the CCD. The door-mounted source will be used for initial calibration only; once the door is opened, it will not illuminate the CCD. In addition to the radio isotopes, we can utilize the charge injection capability of the CCD for some calibrations. This allows an arbitrary amount of charge to be input to the pixels at the top row of the imaging region (exposure area), i.e. the far side from the frame-store region. This charge injection capability may be used to measure the CTI (charge transfer inefficiency) of each column, or even to reduce the CTI. How the charge injection capability will be used will be determined after launch.

Fig. 7.2 provides a schematic view of the XIS system. Charge clouds produced in the CCD by the X-rays focused by the XRT are accumulated on the exposure area for a certain exposure period (typically 8 s in the “normal” mode), and the data are transferred to the Frame Store Area after each exposure. Data stored in the Frame Store Area are read-out sequentially by the AE, and sent to the PPU after the conversion to the digital data. The data are put into the memory in PPU named Pixel RAM. Subsequent data processing is done by accessing the Pixel RAM.

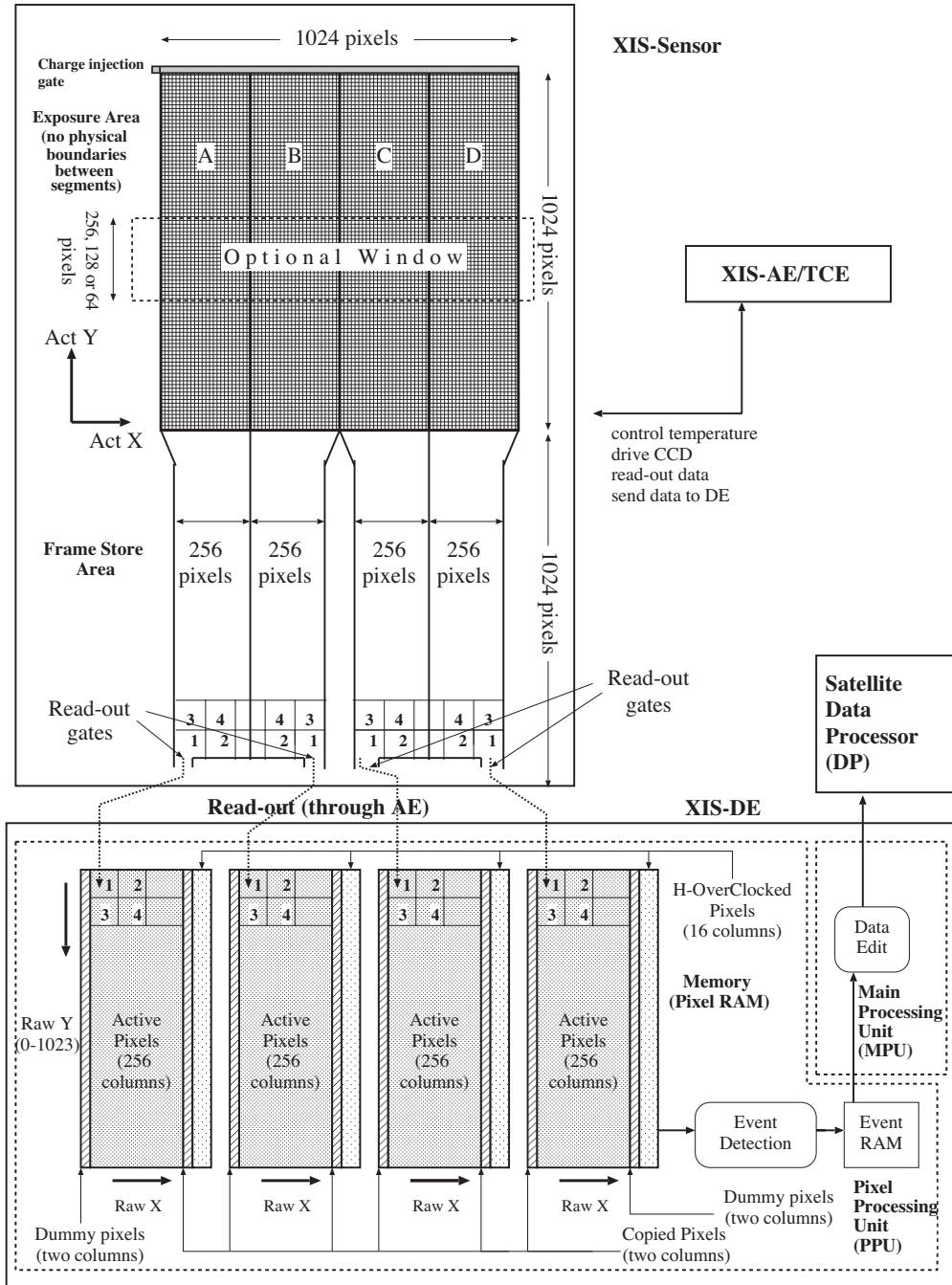


Figure 7.2: One XIS instrument. Each XIS consists of a single CCD chip with  $1024 \times 1024$  X-ray sensitive cells, each  $24 \mu\text{m}$  square. *Astro-E2* contains four CCD sensors (XIS-S0 to S3), two AE/TCUs (AE/TCE01 and AE/TCE23), two PPU's (PPU01 and PPU23), and one MPU. AE/TCU01 and PPU01 service XIS-S0 and XIS-S1, while AE/TCE23 and PPU23 service XIS-S2 and XIS-S3. Two of the XIS CCDs will be front-illuminated (FI) and two will be back-illuminated (BI).

## 7.2 CCD Pixels and Coordinates

A single XIS CCD chip consists of four segments (marked A, B, C and D in Fig. 7.2) and correspondingly has four separate readout nodes. Pixel data collected in each segment are read out from

the corresponding readout node and sent to the Pixel RAM. In the Pixel RAM, pixels are given RAWX and RAWY coordinates for each segment in the order of the readout, such that RAWX values are from 0 to 255 and RAWY values are from 0 to 1023. These physical pixels are named *Active pixels*.

In the same segment, pixels closer to the read-out node are read-out faster and stored in the Pixel RAM faster. Hence, the order of the pixel read-out is the same for segments A and C, and for segments B and D, but different between these two segment pairs, because of the different locations of the readout nodes. In Fig. 7.2, numbers 1, 2, 3 and 4 marked on each segment and Pixel RAM indicate the order of the pixel read-out and the storage in the Pixel RAM.

In addition to the Active pixels, the Pixel RAM stores the *Copied pixels*, *Dummy pixels* and *H-Over-Clocked pixels* (cf. Fig. 7.2). At the borders between two segments, two columns of pixels are copied from each segment to the other. Thus these are named Copied pixels. On both sides of the outer segments, two columns of empty Dummy Pixels are attached. In addition, 16 columns of H-Over-Clocked pixels are attached to each segment.

Actual pixel locations on the chip are calculated from the RAW XY coordinates and the segment ID during ground processing. The coordinates describing the actual pixel location on the chip are named ACT X and ACT Y coordinates (cf. Fig. 7.2). It is important to note that the RAW XY to ACT XY conversion depends on the on-board data processing mode (cf. § 7.4).

### 7.3 Pulse Height Determination, Residual Dark-current Distribution, and Hot Pixels

When a CCD pixel absorbs an X-ray photon, the X-ray is converted to an electric charge, which in turn produces a voltage at the analog output of the CCD. This voltage (“pulse-height”) is proportional to the energy of the incident X-ray. In order to determine the true pulse-height corresponding to the input X-ray energy, it is necessary to subtract the *Dark Levels* and correct possible *optical Light Leaks*.

Dark Levels are non-zero pixel pulse-heights caused by leakage currents in the CCD. In addition, optical and UV light may enter the sensor due to imperfect shielding (“light leak”), producing pulse heights that are not related to X-rays. In the case of the ASCA SIS, these were handled via a single mechanism: Dark Levels of  $16 \times 16$  pixels were sampled and their (truncated) average was calculated for every exposure. Then the same average Dark Level was used to determine the pulse-height of each pixel in the sample. After the launch of ASCA, it was found that the Dark Levels of different pixels were actually different, and their distribution around the average did not necessarily follow a Gaussian. The non-Gaussian distribution evolved with time (referred to as Residual Dark-current Distribution or RDD), and resulted in a degradation of the energy resolution due to incorrect Dark Levels.

For the *Astro-E2* XIS, Dark Levels and Light Leaks are calculated separately in normal mode. Dark Levels are defined for each pixel; those are expected to be constant for a given observation. The PPU calculates the Dark Levels in the Dark Initial mode (one of the special diagnostic modes of the XIS); those are stored in the Dark Level RAM. The average Dark Level is determined for each pixel, and if the dark level is higher than the hot-pixel threshold, this pixel is labeled as a *hot pixel*. Dark Levels can be updated by the Dark Update mode, and sent to the telemetry by the Dark Frame mode. Unlike the case of ASCA, Dark Levels are not determined for every exposure, but the same Dark Levels are used for many exposures unless they are initialized or updated. Analysis of the ASCA data showed that Dark Levels tend to change mostly during the SAA passage of the satellite. Dark Update mode may be employed several times a day after the SAA passage.

Hot pixels are pixels which always output over threshold pulse-heights even without input signals. Hot pixels are not usable for observation, and their output has to be disregarded during scientific analysis. The ASCA SIS did not identify hot pixels on-board, and all the hot pixel data were telemetered and removed during the data analysis procedure. The number of hot pixels increased with time, and eventually occupied significant parts of the telemetry. In the case of XIS, hot pixels are detected on-board by the Dark Initial mode, and their positions and pulse-heights are stored in the Hot-pixel RAM and sent to the telemetry. Thus, hot pixels can be recognized on-board, and they are excluded from the event detection processes. It is also possible to specify the hot pixels manually.

The Light Leaks are calculated on board with the pulse height data after the subtraction of the Dark Levels. A truncated average is calculated for  $64 \times 64$  pixels in every exposure and its running average produces the Light Leak. Thus, the Light Leak is basically same as the Dark Level in ASCA SIS.

The Dark Levels and the Light Leaks are merged in the parallel-sum (P-Sum) mode, so Dark Update mode is not available in P-Sum mode. The Dark Levels, which are defined for each pixel as the case of the normal mode, are updated every exposure. It may be considered that the Light Leak is defined for each pixel in P-Sum mode.

## 7.4 On-board Event Analysis

The main purpose of the on-board processing of the CCD data is to reduce the total amount transmitted to ground. For this purpose, the PPU searches for a characteristic pattern of charge distribution (called an event) in the pre-processed (post- Dark Levels and Light Leaks subtraction) frame data. When an X-ray photon is absorbed in a pixel, the photoionized electrons can spread into at most 4 adjacent pixels. An event is recognized when a valid pulse-height (one between the Event Lower and Upper Thresholds) is found that exceeds the pulse-heights in the eight adjacent pixels (e.g. it is the peak value in the  $3 \times 3$  pixel grid). In P-Sum mode, only the horizontally adjacent pixels are considered. The Copied and Dummy pixels ensure that the event search is enabled on the pixels at the edges of each segment. Again, in the case of P-Sum mode only the inner one of the two columns of Copied or Dummy pixels on each side of the Segment is necessary and used. The RAW XY coordinates of the central pixel are considered the location of the event. Pulse-height data for the adjacent  $5 \times 5$  square pixels (or in P-Sum mode 3 horizontal pixels) are sent to the Event RAM as well as the pixel location.

The MPU reads the Event RAM and edits the data to the telemetry format. The amount of information sent to telemetry depends on the editing mode of the XIS. All the editing modes (in normal mode; see §7.5) are designed to send the pulse heights of at least 4 central pixels of an event to the telemetry, because the charge cloud produced by an X-ray photon can spread into at most 4 pixels. Information of the surrounding pixels may or may not output to the telemetry depending on the editing mode. The  $5 \times 5$  mode outputs the most detailed information to the telemetry, i.e. all 25 pulse-heights from the  $5 \times 5$  pixels containing the event. The size of the telemetry data per event is reduced by a factor of 2 in  $3 \times 3$  mode, and another factor of 2 in  $2 \times 2$  mode. Details of the pulse height information sent to the telemetry are described in the next section.

## 7.5 Data Processing Modes

There are two different kinds of on-board data processing modes. The *Clock modes* describe how the CCD clocks are driven, and determine the exposure time, exposure region, and time resolution.

The Clock modes are determined by a kind of program loaded to the AE. The *Editing modes* specify how detected events are edited, and determine the formats of the XIS data telemetry. Editing modes are determined by the digital electronics.

It is possible to select different mode combinations for the four XISs independently. However, we expect that most observations will use all four in Normal  $5 \times 5$  or  $3 \times 3$  Mode (without Burst or Window options). Other modes are useful for bright sources (when pile-up or telemetry limitations are a concern) or if a higher time resolution ( $< 8$  s) is required.

### 7.5.1 Clock Modes

The following two kinds of Clock Modes are available. Furthermore, two options (Window and Burst options) may be used in combination with the Normal Mode.

- **Normal Mode:** If neither *Window* nor *Burst* option (see below) is specified, the exposure time is 8 seconds, and all the pixels on the CCD are read out every 8 seconds. This can be combined with either of the  $5 \times 5$ ,  $3 \times 3$ , and  $2 \times 2$  Editing modes.
- **Parallel Sum Mode:** The pixel data from multiple rows are summed in the Y-direction on the CCD, and the sum is put in the Pixel RAM as a single row. The number of rows to add is commandable. Parallel Sum mode can be used only with the Timing Editing mode, and the Y coordinate is used to determine the event arrival time. As a result, no spatial resolution is available in the Y-direction. The time resolution of the Parallel Sum Mode is  $8 \text{ s}/1024 \sim 7.8 \text{ ms}$ .

### 7.5.2 Window and Burst Options

The following table indicates how the effective area and exposure time are modified by the Burst and Window options.

Option	Effective area (nominal: $1024 \times 1024$ pixels)	Exposure time (in 8 s period)
None	$1024 \times 1024$ pixels	8 s
Burst	$1024 \times 1024$ pixels	$(n/256) \times 8 \text{ s} \times 1 \text{ exposure}$
Window	$256 \times 1024$ pixels	$2 \text{ s} \times 4 \text{ exposures}$
	$128 \times 1024$ pixels	$1 \text{ s} \times 8 \text{ exposures}$
	$64 \times 1024$ pixels	$0.5 \text{ s} \times 16 \text{ exposures}$
Burst & Window	$256 \times 1024$ pixels	$(n/64) \times 2 \text{ s} \times 4 \text{ exposure}$
	$128 \times 1024$ pixels	$(n/32) \times 1 \text{ s} \times 8 \text{ exposure}$
	$64 \times 1024$ pixels	$(n/16) \times 0.5 \text{ s} \times 16 \text{ exposure}$

Note:  $n$  is an integer.

In the Normal Clock mode, the *Window* and *Burst* options can modify the effective area and exposure time, respectively. The two options are independent, and may be used simultaneously. These options cannot be used with the Parallel Sum Clock mode.

- **Burst Option:** All the pixels are read out every 8 seconds (if the Window option is not specified), but the exposure time can be chosen arbitrarily (with a  $1/32$  second step) within the read-out interval. This option may be used to avoid event pile-up when observing a bright source. However, a dead time is introduced in the exposure. If the exposure is  $t$  s, there is a  $8 - t$  s dead-time every 8 s.

- Window Option:** This option allows shorter exposure times by reading out more frequently only a portion of the CCD. Only the parts of the chip within the Y-direction range specified by the commandable Window is used for exposure (cf. Fig. 7.2). The Window width in the Y-direction is either 256, 128 or 64 pixels, and its position is arbitrary. When the Window width is 256 pixels, the exposure time becomes a quarter of that without the Window option (i.e. 2 s), and the Pixel RAM is filled with the data from four successive exposures. Similarly, when the Window width is 128 or 64 pixels, the exposure time becomes 1/8 or 1/16 of that without the Window option respectively, and the Pixel RAM is filled with the data from 8 or 16 successive exposures.

We show in Fig. 7.3 the time sequence of exposure, frame-store transfer, CCD readout, and storage to the pixel RAM (in PPU) in normal mode with or without Burst/Window option. Note that a dead time is introduced when the Burst option is used.

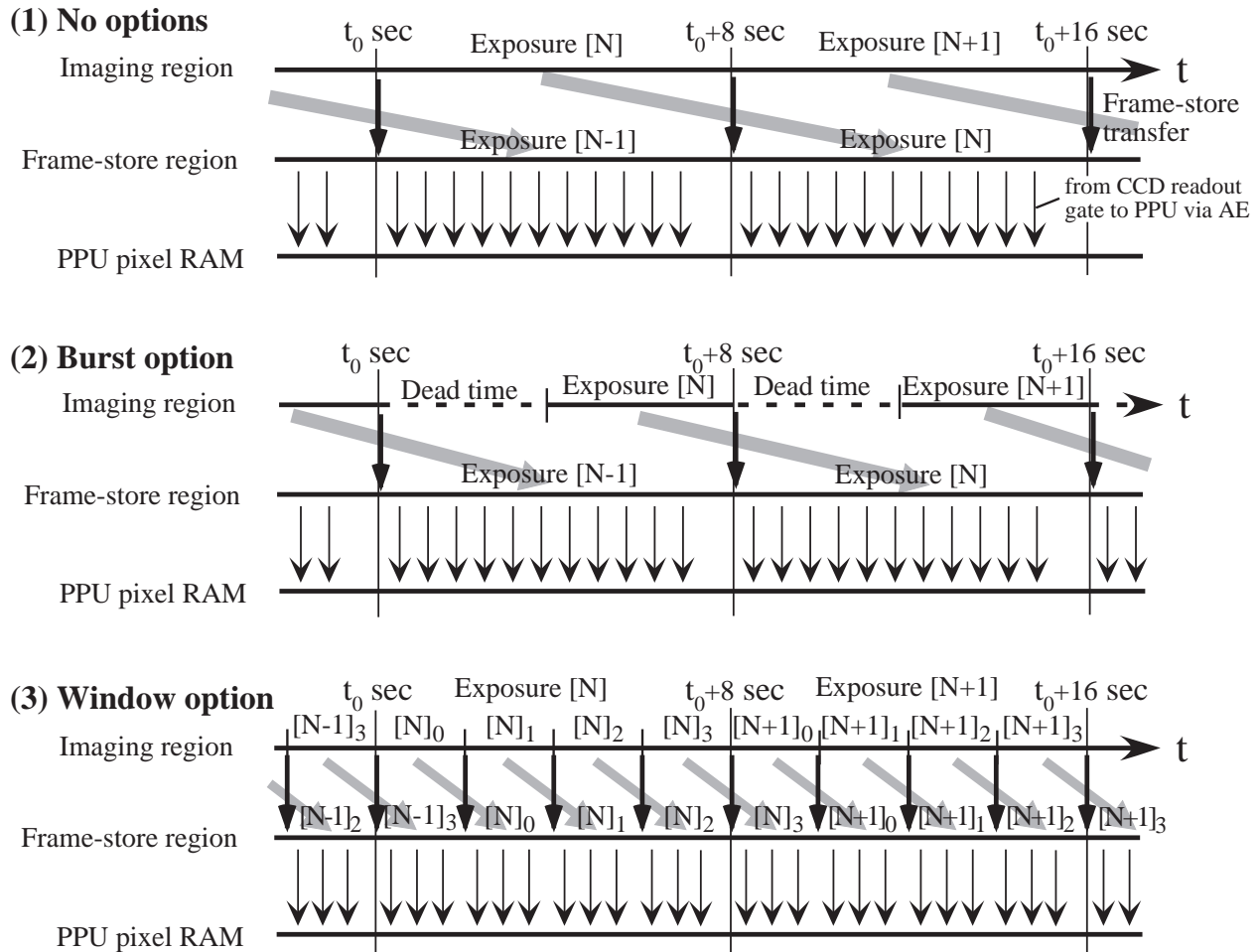


Figure 7.3: Time sequence of the exposure, frame-store transfer, CCD readout, and data transfer to the pixel RAM in PPU is shown (1) in normal mode without options, (2) in normal mode with Burst option, and (3) in normal mode with Window option. In this example, the 1/4 Window option is assumed.



### 7.5.3 Editing Modes

We explain only the observation modes here. Three modes ( $5 \times 5$ ,  $3 \times 3$ , and  $2 \times 2$ ) are usable in normal modes, and only the timing mode in the P-Sum mode.

#### Observation Modes

- **$5 \times 5$  mode:** All the pulse heights of the 25 pixels centered at the event center are sent to the telemetry. This is used with the Normal Clock mode.
- **$3 \times 3$  mode:** Pulse heights of the 9 pixels centered at the event center are sent to the telemetry with the 1-bit information (pulse height larger than the Split Threshold Outer or not) for the surrounding 16 pixels. This is used with the Normal Clock mode.
- **$2 \times 2$  mode:** Pulse heights of the  $2 \times 2$  square pixels are sent to the telemetry. The  $2 \times 2$  pixels are selected to include the event center, second highest pixel in the cross centered at the event center, and the 3rd (or 4th) highest pixel in the cross. The 1-bit information (pulse height larger than the Split Threshold Outer or not) of the 8-attached pixels is also output to the telemetry. This is used with the Normal Clock mode.
- **Timing mode:** Total pulse height and the *Grades* of the event are output to the telemetry. Pulse heights of at most three pixels in the X-direction are summed to give the total pulse height if they are over the Inner Split Threshold. Position and number of pixels exceeding the threshold determines the *Grades*. This is used only with the P-Sum Clock mode. Window and Burst Options are not available in the Timing mode.

We show in Fig. 7.4 the pixel pattern whose pulse height or 1-bit information is sent to the telemetry. We do not assign grades to an event on board in the Normal Clock mode. This means that a dark frame error, if present, can be corrected accurately during the ground processing even in  $2 \times 2$  mode. The definition of the grades in P-Sum mode is shown in Fig. 7.5.

The current expectation is that there will be no differences between the  $5 \times 5$ ,  $3 \times 3$  and  $2 \times 2$  modes. However, we recommend the use of the  $5 \times 5$  mode, or  $3 \times 3$  mode, whenever this is possible within the telemetry limit (which is the case for all but the brightest sources), just in case the extra information might make a difference in reducing some unforeseen systematic errors. With the *Chandra* CCDs, for example,  $5 \times 5$  mode has been used to aid in identifying cosmic ray events.

Besides the observation modes given above, the XIS instrument has several diagnostic modes, used primarily in determining the dark current levels. It is unlikely that those would be used by guest observers.

### 7.5.4 Discriminators

Two kinds of discriminators, area and grade discriminators, can be applied during the on-board processing. The grade discriminator is available only in the timing mode.

The area discriminator is used when we want to reject some (or most) of the frame data from the event extraction. The discriminator works on the Pixel RAM. When the discriminator is set, a part of the Pixel RAM is not used for the event extraction. This may be useful when a bright source is present in the XIS field of view other than the target source. If we set the discrimination area to include only the bright source, we can avoid outputting unnecessary events to the telemetry. Only a single, rectangular area can be specified in a segment for discrimination. Either inside or outside of the area can be rejected from the event extraction. The area discriminator works on the Pixel

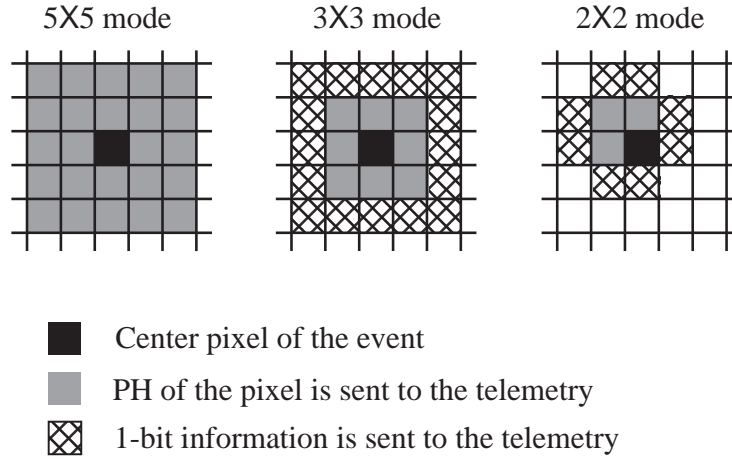


Figure 7.4: Information sent to the telemetry is shown for  $5 \times 5$ ,  $3 \times 3$ , and  $2 \times 2$  modes. 1-bit information means whether or not the PH of the pixel exceeds the outer split threshold. In  $2 \times 2$  mode, the central 4 pixels are selected to include the second and the third (or fourth) highest pixels among the 5 pixels in a cross centered at the event center.

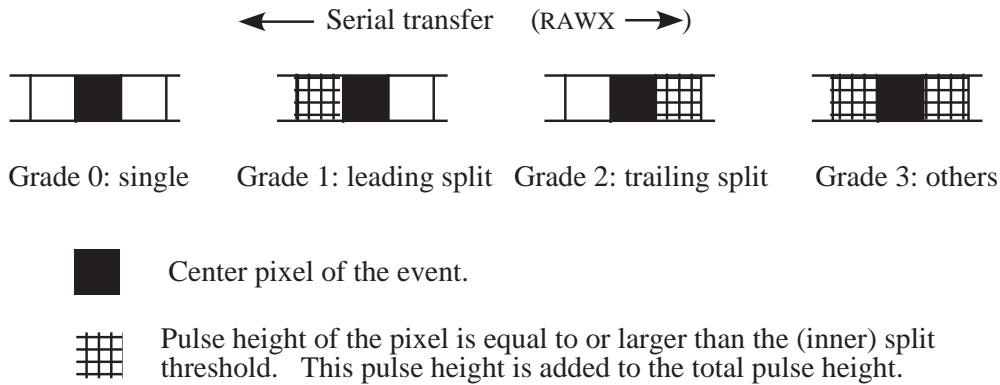


Figure 7.5: Definition of the grades in the P-Sum/timing mode. Total pulse height and the grade of the event are output to the telemetry. Note that the grades are defined referring to the direction of the serial transfer, so the central pixel of a grade 1 event has the *larger* RAWX value, while the opposite is true for a grade 2 event.

RAM, not for the physical area of the CCD. This is important when we apply the discriminator with the window option.

The Grade discriminator is used only in the timing mode. Any combination of the 4 grades can be selected to discriminate the grade for telemetry output.

We do not have the level discriminator which was used in ASCA SIS. The same function can be realized, however, by changing the event threshold.

## 7.6 Photon pile-up

The XIS is essentially a position-sensitive integrating instrument, with the nominal interval between readouts of 8 s. If during the integration time one or more photons strike the same CCD pixel, or

one of its immediate neighbors, these cannot be correctly detected as independent photons: this is the phenomenon of photon pile-up. Here, the modest angular resolution of the *Astro-E2* XRT is an advantage: the central  $3 \times 3$  pixel area receives 2% of the total counts of a point source, and  $\sim 10\%$  of the counts fall within  $\sim 0.15$  arcmin of the image center. We calculated the count rate at which 50% of the events within the central  $3 \times 3$  pixels are piled-up (the pile-up fraction goes down as we move out of the image center; this fraction is  $< 5\%$  for the 0.15 arcmin radius) — although we offer no formal justification for this particular limit, this is compatible with our ASCA SIS experience (i.e., at this level, the pile-up effects do not dominate the systematic uncertainties). **This limit corresponds to  $\sim 10$  cps for a point source observed in the normal mode (full window).** For somewhat brighter sources, window options can be used to reduce the exposure time per frame (the count rate limit is inversely proportional to the exposure time — 1/8 window option reduces the exposure time from 8 s to 1 s, and raises the limit to  $\sim 80$  cps). For even brighter sources, timing mode is recommended: because of the extremely short effective exposure time (8 s/1024  $\sim$  7.8 ms), the pile-up limit is several thousand cps (despite the on-board summing of rows and the one dimensional nature of the event detection algorithm).

From the standpoint of *Astro-E2* proposals, prior to launch, the most appropriate mode can only be estimated; again, we currently believe that a source yielding a total XIS counting rate of 10 counts/s/XIS or less can be observed using the “normal” mode. We emphasize that the *Astro-E2* personnel at ISAS/JAXA or the NASA *Astro-E2* GOF will work with the observers to assure the optimum yield of every observation via selection of the best XIS mode for a given target.

## 7.7 Expected background rate and the telemetry limit

In the case of the XIS, most of the background originates from charged particles (the non-X-ray background, or NXB). The cosmic X-ray background (CXB) rate is much smaller and the flickering pixels are negligible. However, the NXB rate may be much higher compared to ASCA SIS, because XIS has larger CCD area and thicker CCD substrate. We estimated the NXB rate of XIS by referring to the ASCA SIS and *Chandra* ACIS data.

Telemetry limits of FI CCD (counts/XIS/8s)			
Data rate	$5 \times 5$	$3 \times 3$	$2 \times 2$
Superhigh	1950 (2100)	4040 (4190)	8240 (8380)
High	850 (1000)	1850 (2000)	3860 (4010)
Medium	310 (460)	770 (910)	1680 (1830)
Low	— (46)	— (92)	40 (180)

Note: the values in the parenthesis are telemetry limits when no background is present. An event threshold of 100 adu (0.36 keV) is assumed.

The above table shows the estimated telemetry limits of the FI CCD in various editing modes and the telemetry data rates. The NXB rate of the BI CCD may be higher than the FI CCD. The estimated NXB rate in the BI CCD is not available as of the writing of this document; see the *Astro-E2* websites for updated information (see App. C). The low telemetry data rate will not be usable with a BI CCD. When we calculate the telemetry limits, we assumed a nominal telemetry allocation ratio among XRS, XIS, and HXD. The ratio depends on the data rate and may be changed after the launch. The telemetry limits also depend on the event threshold and the data compression efficiency. We apply a simple data compression algorithm to the event data, whose efficiency may depend on the energy spectrum of the source. Thus the telemetry limits listed above should be regarded as only approximate values.

### 7.7.1 Out-of-time events

X-ray photons detected during the frame-store transfer do not correspond to the true image, but instead appear as a streak or blur in the readout direction. These events are called out-of-time events., and they are an intrinsic feature of CCD detectors. Similar streaks are seen from bright sources observed with *Chandra* and *XMM-Newton*. Out-of-time events produce a tail in the image, which can be an obstacle to detecting a low surface brightness feature in an image around a bright source. Thus the out-of-time events reduce the dynamic range of the detector. Since XIS spends 25 ms in the frame-store transfer, about 0.3% ( $= 0.025/8 \times 100$ ) of all events will be out-of-time events. However, because the orientation of the CCD chip is different among the sensors, one can in principle distinguish a true feature of low surface brightness and the artifact due to the out-of-time events by comparing the images from two or more XISs.

## 7.8 Radiation Damage and On-board Calibration of the XIS

The performance of X-ray CCDs gradually degrades in the space environment due to the radiation damage. This generally causes an increase in the dark current and a decrease of the charge transfer efficiency (CTE). In the case of XIS, the increase of the dark current is expected to be small due to the low ( $-90^{\circ}\text{C}$ ) operating temperature of the CCD. However, a decrease in CTE is unavoidable. Thus, continuous calibration of CCD on orbit is essential to the good performance of the XIS. For this purpose, we use a radio isotope source and charge injection as explained below:

- (i) Each XIS carries  $^{55}\text{Fe}$  calibration sources near the two corners of the chip, which will be used to monitor the instrument gain.
- (ii) Each XIS CCD is equipped with charge injection capability, which may be useful to measure and even suppress CTI.

It is difficult to predict before launch how well we can calibrate the long-term performance change of XIS on orbit. However, the XIS may be assumed to perform at the nominal pre-launch level for the purpose of Cycle 1 proposals.

## Chapter 8

# Hard X-ray Detector



Figure 8.1: The Hard X-ray Detector before installation.

The Hard X-ray Detector (HXD; see Figure 8.1) is a non-imaging, collimated hard X-ray scintillating instrument sensitive in the band of  $\sim 10$  keV to  $\sim 600$  keV.

It has been developed jointly by the University of Tokyo, Aoyama Gakuin University, Hiroshima University, ISAS/JAXA, Kanazawa University, the National Laboratory for High Energy Physics (KEK), the Research Center for Nuclear Physics of Osaka University, Saitama University, SLAC, and RIKEN. Its main purpose is to extend the bandpass of the *Astro-E2* observatory to the highest feasible energies, thus allowing broad-band studies of celestial objects.

The HXD sensor (HXD-S) is a compound-eye detector instrument, consisting of 16 main detectors (arranged as a  $4 \times 4$  array) and the surrounding 20 crystal scintillators for active shielding. Each unit actually consists of two types of detectors: a GSO/BGO phoswich counter, and 2 mm-thick PIN silicon diodes located inside the well, but in front of the GSO scintillator. The PIN

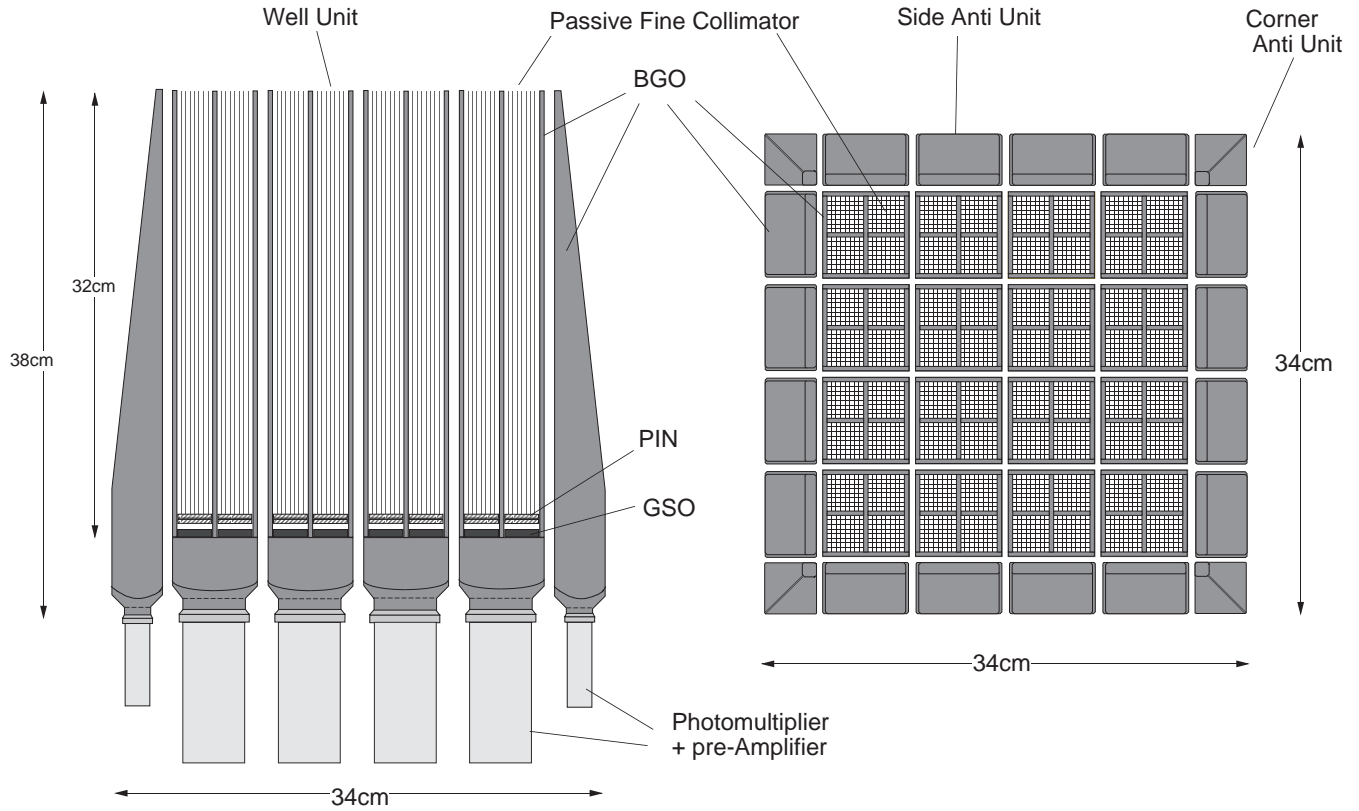


Figure 8.2: Schematic picture of the HXD instrument, which consists of two types of detectors: the PIN diodes located in the front of the GSO scintillator, and the scintillator itself.

diodes are mainly sensitive below  $\sim 60$  keV, while the GSO/BGO phoswich counter (scintillator) is sensitive above  $\sim 30$  keV. The scintillator signals are read out by photomultiplier tubes. The schematic drawing of the HXD is given in Fig. 8.2. The HXD features an effective area of  $\sim 160$  cm<sup>2</sup> at 20 keV, and  $\sim 330$  cm<sup>2</sup> at 100 keV (see Fig. 8.2). The energy resolution is  $\sim 3.0$  keV (FWHM) for the PIN diodes, and  $7.6/\sqrt{E}$  % (FWHM) for the scintillators where  $E$  is energy in MeV. The HXD time resolution is 61  $\mu$ s.

## 8.1 GSO/BGO Counter Units

Each main detector unit is of a well-type design with active anti-coincidence shields. The shields and the coarse collimator itself are made of Bismuth Germanate (BGO;  $\text{Bi}_4\text{Ge}_3\text{O}_{12}$ ) crystals, while the X-ray sensing material “inside the well” is GSO (Gadolinium Silicate, or  $\text{Gd}_2\text{SiO}_5(\text{Ce})$ ) crystal. The aspect ratio of the coarse collimators yields an acceptance angle for the GSO of  $4.5^\circ$  (FWHM). Each unit thus forms a  $2 \times 2$  matrix, containing four 24 mm  $\times$  24 mm, 5 mm thick GSO crystals, each placed behind the PIN diode. The reason for the choice of the two different crystals for the sensor and the shield is dictated by the large stopping ability of both, yet the very different rise/decay times, of  $\sim 706$  ns for BGO, and  $\sim 122$  ns for GSO, at a working temperature of  $-20^\circ\text{C}$ . This allows for an easy discrimination of the shield vs. X-ray sensor signals, where a single PM tube can discriminate between the two types of scintillators in which an event may have occurred. Any particle events or Compton events that are registered by both the BGO and GSO can be rejected by this phoswich technique, utilizing custom-made pulse-shaping LSI circuits. The BGO crystals are also placed underneath of the GSO sensors, and thus each well is a five-sided anti-coincidence

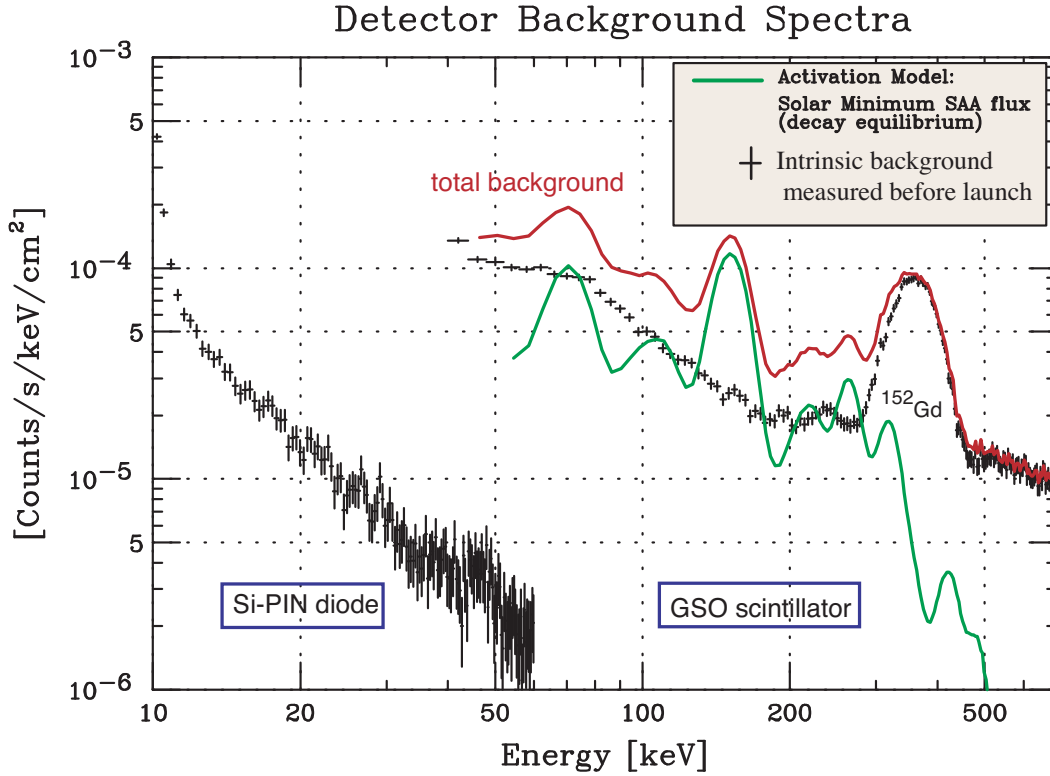


Figure 8.3: The HXD background, including both intrinsic and cosmic components for both the PIN and GSO detectors.

system.

## 8.2 PIN Diodes

The low energy response of the HXD is provided by 2 mm thick PIN silicon diodes, placed in front of each GSO crystal. The diodes absorb X-rays with energies below  $\sim 40$  keV, but gradually become transparent to harder X-rays, which in turn reach and are registered by the GSO detectors. The X-rays are photoelectrically absorbed in the PIN diodes, and the signal is amplified, converted to a digital form, and read out by the associated electronics. The PIN diodes are of course also shielded from particle events by the BGO shields, as they are placed inside the deep BGO wells. The field of view of the PIN diodes is collimated to  $34' \times 34'$  FWHM by the passive fine collimators. Above  $\sim 100$  keV, the GSO field of view approaches the actively collimated  $4.5^\circ$  (FWHM), because the fine collimators become gradually transparent.

## 8.3 HXD Background, Background Rejection, and its Sensitivity

Although the HXD is a non-imaging instrument, its instantaneous background may be reproduced through modeling, without requiring separate off-source observations. This is because the HXD has been designed to achieve an extremely low in-orbit background ( $< 1 \times 10^{-4}$  c s<sup>-1</sup> cm<sup>-2</sup> keV<sup>-1</sup>), based on a combination of novel techniques: (1) the five-sided tight BGO shielding as mentioned above; (2) the use of the 20 shielding counters made of thick BGO crystals which surround the 16 main GSO/BGO counters; (3) sophisticated onboard signal processing and onboard event selection, employing both high-speed parallel hardware circuits in the Analog Electronics, and CPU-based

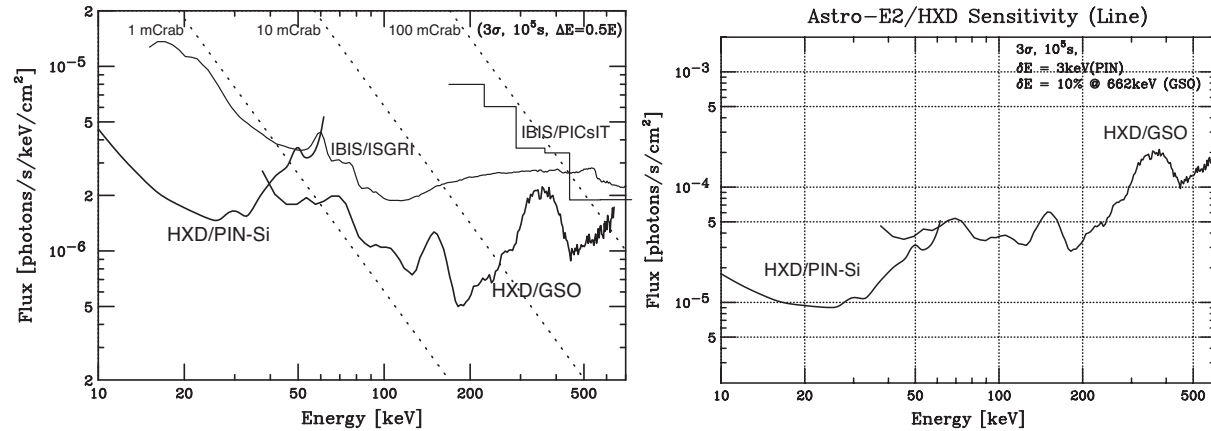


Figure 8.4: [Left] The sensitivity of the HXD to continuum emission, taking into account the expected background. [Right] Same, for line emission.

signal handling in the Digital Electronics; and (4) the careful choice of materials that do not get strongly radio-activated under in-orbit particle bombardment. Finally, the fine collimator effectively reduces both the CXB contribution and the source confusion.

The current best estimate of the detector background is plotted in Fig. 8.3; this plot includes the intrinsic background component as measured on the ground, and the component expected due to detector activation. Figure 8.4[Left] illustrates the sensitivity of the detector for the measurement of the continuum, while Fig. 8.4[Right] gives the sensitivity to line emission. As is the case for every non-imaging instrument (and in particular, for those sensitive in the hard X-ray range), the limiting factor for the sensitivity of the HXD will be the error in estimation of background. Current estimates of this error are about 10% at  $1\sigma$ , and the final goal is about 5%. For sources fainter than the background estimation error, background subtraction has to be performed carefully. Since this is the first space flight of the HXD-type detector, the details will depend on the experience with in-orbit data, and the status of background estimation error and procedures for background subtraction will be presented on the *Astro-E2* websites. For any pre-flight estimates, the background files are available at the *Astro-E2* proposal websites listed in Appendix C.

## 8.4 Data analysis procedure

HXD data are accumulated by event by event basis. After on-board data selection, event data are further screened by the ground pipe-line analysis process. By referring to the trigger and flag information (including the inter-unit anti-coincidence hit patterns), the pipe-line assigns specific grades to the HXD events such as pure PIN events and pure GSO events. Detector responses and background files that match the particular grade of the events will be provided by the HXD team. Note that currently there are no user-specified parameters for the HXD.



# Appendix A

## Acronyms

The following table lists acronyms used in this document, along with the chapter where they are first used or defined.

Chapter	Acronym	Definition
2	ADR	Adiabatic Demagnetization Refrigerator
7	AE	Analog Electronics
2	BGO	Bismuth Germanate
2	BI	Back-illuminated
3	CALDB	Calibration Database
6	CAP	Calorimeter Analog Processor
7	CCD	Charge-Coupled Devices
6	CDP	Calorimeter Digital Processor
3	Co-I	Co-investigator
7	CTE	Charge Transfer Efficiency
7	CTI	Charge Transfer Inefficiency
6	CTS	Calorimeter Thermal Sink
7	CXB	Cosmic X-ray Background
7	DE	Digital Electronics
6	DMS	Dewar Main Shell
6	DSP	Digital Signal Processor
2	EEF	Encircled Energy Function
5	EOB	Extensible Optical Bench
6	FEA	Front End Assembly
2	FI	Front-illuminated
6	FW	Filter Wheel (on XRS)
2	FWHM	Full-width half-maximum
3	FITS	Flexible Image Transport System
3	FTOOLS	FITS Tools

Chapter	Acronym	Definition
1	GO	Guest Observer
1	GOF	Guest Observer Facility
3	GRB	Gamma-Ray Burst
1	GSFC	Goddard Space Flight Center
2	GSO	Gadolinium Silicate
3	HEASARC	High Energy Astrophysics Science Archive Research Center
2	HETG	High Energy Transmission Grating (on <i>Chandra</i> )
2	HPD	Half-Power Diameter
1	HXD	Hard X-Ray Detector
1	ISAS	Institute of Space and Astronautical Science
6	IVCS	Inner Vapor Cooled Shield
1	JAXA	Japan Aerospace Exploration Agency
6	JFET	Junction Field Effect Transistor
2	LETG	Low Energy Transmission Grating (on <i>Chandra</i> )
7	MPU	Main Processing Unit
4	NRA	NASA Research Announcement
1	NASA	National Aeronautics and Space Administration
4	NOI	Notice of Intent
7	NXB	Non-X-ray Background
7	OBF	Optical Blocking Filter
2	PIN	Positive Intrinsic Negative
2	PI	Principal Investigator
7	PPU	Pixel Processing Units
4	PSPC	Position-Sensitive Proportional Counter (on ROSAT)
7	P-Sum	Parallel-Sum
7	QDE	Quantum Detection Efficiency
7	RDD	Residual Dark-current Distribution
2	RGS	Reflection Grating Spectrometer (on <i>XMM-Newton</i> )
4	RFA	Research Focus Area
3	RPS	Remote Proposal Submission tool
3	SAA	South Atlantic Anomaly
2	S/C	Spacecraft
6	SIS	Solid-state Imaging Spectrometer (on ASCA)
1	SWG	Science Working Group
7	TCE	TEC Control Electronics
7	TEC	Thermo-Electric Coolers
1	TOO	Target Of Opportunity
2	USC	Uchinoura Space Center
1	XIS	X-Ray Imaging Spectrometer
1	XRS	X-Ray Spectrometer
1	XRT	X-Ray Telescope
1	XRT-I	X-Ray Telescope for one of the four XIS detectors
1	XRT-S	X-Ray Telescope for the XRS detector

## Appendix B

### SWG Target List

The SWG target list is presented here twice, sorted both by type of source and by Right Ascension (RA) and Declination (Dec). Details of targets with constraints are listed in the last section.

## B.1 Targets Sorted by Category

### B.1.1 Calibration

Target	RA	Dec	Pri.	Exp.	#obs
E0102-72	01 04 02.4	-72 01 59.9	A	20	1
E0102-72	01 04 02.4	-72 01 59.9	A	200	4
E0102-72	01 04 02.4	-72 01 59.9	A	20	1
E0102-72	01 04 02.4	-72 01 59.9	A	200	4
E0102-72	01 04 02.4	-72 01 59.9	A	20	1
E0102-72	01 04 02.4	-72 01 59.9	A	20	1
E0102-72	01 04 02.4	-72 01 59.9	A	20	1
E0102-72	01 04 02.4	-72 01 59.9	A	20	1
AXAF DEEP FIELD S	03 32 28.0	-27 48 30.0	A	140	1
CAPELLA	05 16 41.4	+45 59 52.8	A	180	4
N132D	05 25 02.9	-69 38 56.0	A	50	5
CRAB.AT.AIM.POINT	05 34 32.0	+22 00 52.1	A	10	1
CRAB.VIGNETTING	05 34 32.0	+22 00 52.1	A	40	8
CRAB.STRAY	05 34 32.0	+22 00 52.1	A	60	6
CRAB.AIMPOINT.SEARCH	05 34 32.0	+22 00 52.1	A	25	5
CRAB.FC.RESPONSE	05 34 32.0	+22 00 52.1	A	40	8
ETA CARINAE	10 45 03.6	-59 41 04.2	A	20	1
LOCKMAN HOLE	10 52 43.0	+57 28 48.0	A	60	1
MRK421	11 04 27.3	+38 12 31.8	A	12	1
GX301-2	12 26 37.6	-62 46 13.0	A	80	4
3C 273 (OFFSET)	12 29 06.7	+02 03 08.6	A	20	2
3C273	12 29 06.7	+02 03 08.6	A	80	1
PSR B1509-58	15 13 54.2	-59 08 06.0	A	80	1
4U1626-67	16 32 16.8	-67 27 43.0	A	5	1
VEGA	18 36 56.3	+38 47 01.3	A	10	1
CYGNUS LOOP	20 55 59.9	+31 59 48.4	A	10	1
CAS A	23 23 24.0	+58 48 54.0	A	3	1
CAS A	23 23 24.0	+58 48 54.0	A	3	1
CAS A	23 23 24.0	+58 48 54.0	A	12	4
CAS A	23 23 24.0	+58 48 54.0	A	3	1
CAS A	23 23 24.0	+58 48 54.0	A	3	1
CAS A	23 23 24.0	+58 48 54.0	A	12	4

### B.1.2 Gamma-Ray Burst

Target	RA	Dec	Pri.	Exp.	#obs
GRB AFTERGLOW	00 00 00.0	+00 00 00.0	A(TOO)	200	5

### B.1.3 Stars and Star Forming Regions

Target	RA	Dec	Pri.	Exp.	#obs
73P/SCHWASSMANN-WACH	01 24 08.4	-10 09 02.2	A	35	3
ALGOL	03 08 10.1	+40 57 20.3	A	80	1
V773 TAU	04 14 12.9	+28 12 12.3	A	80	1
ETA CARINAE	10 45 03.6	-59 41 04.0	A	50	1
9P/TEMPEL1	13 37 25.0	-09 28 04.3	B	40	10
RHO OPH CORE F	16 27 28.0	-24 39 33.5	A	200	1
73P/SCHWASSMANN-WACH	20 26 48.8	+29 44 27.5	A	5	1
73P/SCHWASSMANN-WACH	21 20 37.0	+24 41 28.2	A	20	1

### B.1.4 CV'S and XRB'S

Target	RA	Dec	Pri.	Exp.	#obs
EXO 0748-67	07 48 33.8	-67 45 07.4	A	120	1
VELA X-1	09 02 06.8	-40 33 17.4	A	90	1
VELA X-1	09 02 06.8	-40 33 17.4	A	30	1
GX 301-2	12 26 37.6	-62 46 13.0	B	50	2
GX 301-2	12 26 37.6	-62 46 13.0	A	70	2
EX HYDRA	12 52 24.4	-29 14 56.7	A	80	1
CIR X-1	15 20 41.0	-57 10 00.0	B	40	2
XTE J1550-564	15 50 58.7	-56 28 36.0	A(TOO)	40	1
4U1624-49	16 28 02.4	-49 11 25.0	B	40	1
4U1626-67	16 32 16.8	-67 27 43.0	B	100	1
XTE J1650-500	16 50 01.0	-49 57 45.0	A(TOO)	40	1
GRO J1655-40	16 54 00.0	-39 50 43.4	A(TOO)	40	1
HER X-1	16 57 49.8	+35 20 32.6	B	60	3
GX 339-4	17 02 49.5	-48 47 23.0	A(TOO)	40	1
1E1743.1-2843	17 46 21.0	-28 43 44.0	A	100	1
GX 13+1	18 14 31.0	-17 09 26.0	A	50	1
AM HERCULIS	18 16 13.3	+49 52 04.2	B	80	1
V4641 SGR	18 19 21.6	-25 24 25.1	A(TOO)	40	1
4U 1822-37	18 25 46.7	-37 06 18.9	B	40	1
V603 AQL	18 48 54.5	+00 35 02.6	B	80	1
SS433	19 11 49.6	+04 58 57.7	A	120	4
GRS 1915+105	19 15 11.0	+10 56 44.9	A	80	1
CYG X-1	19 58 21.6	+35 12 06.1	A(TOO)	40	1
CYG X-1	19 58 21.7	+35 12 05.8	B	100	4
CYGNUS X-3	20 32 26.5	+40 57 09.0	A	100	1
SS CYG (OUTBURST)	21 42 42.7	+43 35 09.5	A(TOO)	40	1
SS CYG (QUIESCENCE)	21 42 42.7	+43 35 09.5	A	40	1

**B.1.5 Galactic Diffuse Emission**

Target	RA	Dec	Pri.	Exp.	#obs
TYCHO'S SNR NW	00 25 00.3	+64 10 41.0	B	100	1
TYCHO'S SNR CTR	00 25 19.3	+64 08 11.0	A	120	1
TYCHO'S SNR E	00 25 55.3	+64 07 13.0	B	100	1
N103B	05 08 59.6	-68 43 36.0	B	40	1
SNR 1987A	05 35 28.3	-69 16 13.0	B	40	1
PUPPIS A N	08 22 00.0	-42 37 25.0	B	20	1
PUPPIS A NE	08 23 34.3	-42 46 19.2	B	50	1
PUPPIS A E KNOT	08 24 10.8	-42 57 54.0	B	35	1
VELA BULLET D	09 00 09.6	-45 54 54.8	B	50	1
G292.0+1.8 NW	11 24 22.8	-59 13 45.0	B	50	1
G292.0+1.8 PULSAR	11 24 39.1	-59 16 22.4	B	50	1
RCW 86	14 41 08.6	-62 40 25.4	B	100	1
SN1006 S KNOT	15 02 30.0	-42 06 08.0	A	80	1
SN1006 CENTER	15 02 56.1	-41 55 58.3	A	80	1
SN1006 SE	15 03 39.6	-42 06 05.0	A	80	1
SN1006 NE	15 03 52.4	-41 47 21.8	A	80	1
KEPLER	17 30 42.4	-21 28 48.5	B	100	1
RADIO ARC	17 46 18.6	-28 53 48.0	B	100	1
THE RIDGE EMISSION	17 45 30.0	-29 06 00.0	B	100	1
THE RIDGE EMISSION	17 45 30.0	-29 06 00.0	A	100	1
THE GALACTIC CENTER	17 45 31.1	-29 02 29.0	A	100	1
SGR A	17 45 44.1	-29 00 23.0	A	60	1
SGR B2	17 47 20.1	-28 23 12.0	A	100	1
W49B	19 11 11.1	+09 06 08.1	A	150	1
CYGNUS LOOP POS3	20 55 31.9	+31 52 48.4	A	30	1
CYGNUS LOOP POS2	20 55 45.9	+31 56 18.4	A	30	1
CYGNUS LOOP POS1	20 55 59.9	+31 59 48.4	A	40	1
CAS A W	23 23 12.1	+58 48 39.9	A	50	1
CAS A N	23 23 23.7	+58 50 22.4	A	50	1
CAS A E	23 23 40.2	+58 48 00.7	A	50	1

**B.1.6 Extragalactic Compact Sources**

Target	RA	Dec	Pri.	Exp.	#obs
NGC 3783	11 39 01.8	-37 44 19.0	A	150	1
3C120	04 33 11.1	+05 21 15.6	A	100	1
IC 4329A	13 49 19.3	-30 18 34.4	A	80	1
NGC1068	02 42 40.0	+00 00 47.0	A	100	1
MRK766	12 18 26.5	+29 48 46.0	A	100	1
NGC 7314	22 35 46.1	-26 03 02.2	A	100	1
NGC 5506	14 13 14.8	-03 12 27.0	A	80	1
NGC 4151	12 10 32.5	+39 24 20.9	A	50	1
NGC 4051	12 03 10.0	+44 31 53.0	A	100	1
NGC 2992	09 45 42.0	-14 19 35.0	A	20	1
IRAS18325-5926	18 36 58.0	-59 24 09.0	A	100	1
MCG-6-30-15	13 35 53.8	-34 17 44.0	A	200	1
CENTAURUS A	13 25 27.6	-43 01 08.8	A	40	1
NGC4507	12 35 36.6	-39 54 33.0	B	100	1
NGC 3031	09 55 33.0	+69 03 55.0	B	160	1
NGC 2992	09 45 42.0	-14 19 35.0	B	20	1
NGC 3516	11 06 47.5	+72 34 06.9	B	150	2
CIRCINUS GALAXY	14 13 09.9	-65 20 20.5	B	100	1

**B.1.7 Extragalactic Diffuse Sources**

Target	RA	Dec	Pri.	Exp.	#obs
NGC 253	00 47 33.0	-25 17 18.0	A	100	1
PERSEUS OFFSET1	03 19 32.1	+41 30 42.5	A	50	1
PERSEUS CLUSTER	03 19 48.1	+41 30 42.5	A	100	1
PERSEUS OFFSET2	03 20 04.1	+41 30 42.5	A	50	1
NGC 1399	03 38 29.1	-35 27 03.0	B	90	1
A520W	04 54 03.5	+02 55 14.0	B	80	1
A520E	04 54 15.0	+02 55 14.0	B	60	1
A754	09 09 18.7	-09 41 07.1	A	80	1
M 82	09 55 55.0	+69 40 47.0	B	100	1
ABELL 1060	10 36 42.8	-27 31 42.0	B	100	1
NGC4406 OFFSET	12 26 08.8	+13 00 16.6	A	50	1
NGC4406	12 26 12.4	+12 56 50.4	A	50	1
M87 NW	12 30 37.1	+12 26 26.6	A	50	1
M87	12 30 49.4	+12 23 26.6	A	50	1
M87 EAST	12 31 01.7	+12 23 26.6	A	50	1
NGC 4636	12 42 49.9	+02 41 16.0	A	100	1
NGC 4649	12 43 39.6	+11 33 09.9	B	100	1
CENTAURUS CLUSTER	12 48 48.9	-41 18 44.0	A	90	1
NGC5044 GROUP	13 15 24.0	-16 23 24.0	A	100	1
A1795	13 48 53.0	+26 35 34.0	A	40	1
ABELL 2142	15 58 22.1	+27 13 22.8	B	80	1
A 2199	16 28 37.0	+39 31 28.0	B	100	1
A2218	16 35 52.3	+66 12 35.0	B	140	1
A 2256 OFFSET	17 03 20.0	+78 39 12.0	A	60	1
A 2256 CENTER	17 04 10.0	+78 38 00.0	A	40	1
ABELL_3667_CENTER	20 12 32.5	-56 50 16.6	A	40	1
ABELL_3667_SE	20 13 00.4	-56 52 46.3	A	100	1
A2597	23 25 20.0	-12 07 30.0	B	50	1

**B.2 Targets Sorted by RA**

Abbrev.	Target Type
GRB	Gamma-Ray Burst
CAL	Calibration
GDE	Galactic Diffuse Emission
EDS	Extragalactic Diffuse Sources
XRB	CV's and XRB's
SFR	Stars and Star Forming Regions
ECS	Extragalactic Compact Sources



Target	RA	Dec	Cat.	Pri.	Exp.	#obs
GRB AFTERGLOW	00 00 00.0	+00 00 00.0	GRB	A(TOO)	200	5
TYCHO'S SNR NW	00 25 00.3	+64 10 41.0	GDE	B	100	1
TYCHO'S SNR CTR	00 25 19.3	+64 08 11.0	GDE	A	120	1
TYCHO'S SNR E	00 25 55.3	+64 07 13.0	GDE	B	100	1
NGC 253	00 47 33.0	-25 17 18.0	EDS	A	100	1
E0102-72	01 04 02.4	-72 01 59.9	CAL	A	20	1
E0102-72	01 04 02.4	-72 01 59.9	CAL	A	20	1
E0102-72	01 04 02.4	-72 01 59.9	CAL	A	20	1
E0102-72	01 04 02.4	-72 01 59.9	CAL	A	20	1
E0102-72	01 04 02.4	-72 01 59.9	CAL	A	20	1
E0102-72	01 04 02.4	-72 01 59.9	CAL	A	20	1
E0102-72	01 04 02.4	-72 01 59.9	CAL	A	200	4
E0102-72	01 04 02.4	-72 01 59.9	CAL	A	200	4
73P/SCHWASSMANN-WACH	01 24 08.4	-10 09 02.2	SFR	A	35	3
NGC1068	02 42 40.0	+00 00 47.0	ECS	A	100	1
ALGOL	03 08 10.1	+40 57 20.3	SFR	A	80	1
PERSEUS OFFSET1	03 19 32.1	+41 30 42.5	EDS	A	50	1
PERSEUS CLUSTER	03 19 48.1	+41 30 42.5	EDS	A	100	1
PERSEUS OFFSET2	03 20 04.1	+41 30 42.5	EDS	A	50	1
AXAF DEEP FIELD S	03 32 28.0	-27 48 30.0	CAL	A	140	1
NGC 1399	03 38 29.1	-35 27 03.0	EDS	B	90	1
V773 TAU	04 14 12.9	+28 12 12.3	SFR	A	80	1
3C120	04 33 11.1	+05 21 15.6	ECS	A	100	1
A520W	04 54 03.5	+02 55 14.0	EDS	B	80	1
A520E	04 54 15.0	+02 55 14.0	EDS	B	60	1
N103B	05 08 59.6	-68 43 36.0	GDE	B	40	1
CAPELLA	05 16 41.4	+45 59 52.8	CAL	A	180	4
N132D	05 25 02.9	-69 38 56.0	CAL	A	50	5
CRAB_AT_AIM_POINT	05 34 32.0	+22 00 52.1	CAL	A	10	1
CRAB_AIMPOINT_SEARCH	05 34 32.0	+22 00 52.1	CAL	A	25	5
CRAB_FC_RESPONSE	05 34 32.0	+22 00 52.1	CAL	A	40	8
CRAB_VIGNETTING	05 34 32.0	+22 00 52.1	CAL	A	40	8
CRAB_SFRAY	05 34 32.0	+22 00 52.1	CAL	A	60	6
SNR 1987A	05 35 28.3	-69 16 13.0	GDE	B	40	1
EXO 0748-67	07 48 33.8	-67 45 07.4	XRB	A	120	1
PUPPIS A N	08 22 00.0	-42 37 25.0	GDE	B	20	1
PUPPIS A NE	08 23 34.3	-42 46 19.2	GDE	B	50	1
PUPPIS A E KNOT	08 24 10.8	-42 57 54.0	GDE	B	35	1
VELA BULLET D	09 00 09.6	-45 54 54.8	GDE	B	50	1
VELA X-1	09 02 06.8	-40 33 17.4	XRB	A	30	1
VELA X-1	09 02 06.8	-40 33 17.4	XRB	A	90	1
A754	09 09 18.7	-09 41 07.1	EDS	A	80	1
NGC 2992	09 45 42.0	-14 19 35.0	ECS	A	20	1
NGC 2992	09 45 42.0	-14 19 35.0	ECS	B	20	1
NGC 3031	09 55 33.0	+69 03 55.0	ECS	B	160	1
M 82	09 55 55.0	+69 40 47.0	EDS	B	100	1

Target	RA	Dec	Cat.	Pri.	Exp.	#obs
ABELL 1060	10 36 42.8	-27 31 42.0	EDS	B	100	1
ETA CARINAE	10 45 03.6	-59 41 04.0	SFR	A	50	1
ETA CARINAE	10 45 03.6	-59 41 04.2	CAL	A	20	1
LOCKMAN HOLE	10 52 43.0	+57 28 48.0	CAL	A	60	1
MRK421	11 04 27.3	+38 12 31.8	CAL	A	12	1
NGC 3516	11 06 47.5	+72 34 06.9	ECS	B	150	2
G292.0+1.8 NW	11 24 22.8	-59 13 45.0	GDE	B	50	1
G292.0+1.8 PULSAR	11 24 39.1	-59 16 22.4	GDE	B	50	1
NGC 3783	11 39 01.8	-37 44 19.0	ECS	A	150	1
NGC 4051	12 03 10.0	+44 31 53.0	ECS	A	100	1
NGC 4151	12 10 32.5	+39 24 20.9	ECS	A	50	1
MRK766	12 18 26.5	+29 48 46.0	ECS	A	100	1
NGC4406 OFFSET	12 26 08.8	+13 00 16.6	EDS	A	50	1
NGC4406	12 26 12.4	+12 56 50.4	EDS	A	50	1
GX 301-2	12 26 37.6	-62 46 13.0	XRB	B	50	2
GX 301-2	12 26 37.6	-62 46 13.0	XRB	A	70	2
GX301-2	12 26 37.6	-62 46 13.0	CAL	A	80	4
3C 273 (OFFSET)	12 29 06.7	+02 03 08.6	CAL	A	20	2
3C273	12 29 06.7	+02 03 08.6	CAL	A	80	1
M87 NW	12 30 37.1	+12 26 26.6	EDS	A	50	1
M87	12 30 49.4	+12 23 26.6	EDS	A	50	1
M87 EAST	12 31 01.7	+12 23 26.6	EDS	A	50	1
NGC4507	12 35 36.6	-39 54 33.0	ECS	B	100	1
NGC 4636	12 42 49.9	+02 41 16.0	EDS	A	100	1
NGC 4649	12 43 39.6	+11 33 09.9	EDS	B	100	1
CENTAURUS CLUSTER	12 48 48.9	-41 18 44.0	EDS	A	90	1
EX HYDRA	12 52 24.4	-29 14 56.7	XRB	A	80	1
NGC5044 GROUP	13 15 24.0	-16 23 24.0	EDS	A	100	1
CENTAURUS A	13 25 27.6	-43 01 08.8	ECS	A	40	1
MCG-6-30-15	13 35 53.8	-34 17 44.0	ECS	A	200	1
9P/TEMPEL1	13 37 25.0	-09 28 04.3	SFR	B	40	10
A1795	13 48 53.0	+26 35 34.0	EDS	A	40	1
IC 4329A	13 49 19.3	-30 18 34.4	ECS	A	80	1
CIRCINUS GALAXY	14 13 09.9	-65 20 20.5	ECS	B	100	1
NGC 5506	14 13 14.8	-03 12 27.0	ECS	A	80	1
RCW 86	14 41 08.6	-62 40 25.4	GDE	B	100	1
SN1006 S KNOT	15 02 30.0	-42 06 08.0	GDE	A	80	1
SN1006 CENTER	15 02 56.1	-41 55 58.3	GDE	A	80	1
SN1006 SE	15 03 39.6	-42 06 05.0	GDE	A	80	1
SN1006 NE	15 03 52.4	-41 47 21.8	GDE	A	80	1
PSR B1509-58	15 13 54.2	-59 08 06.0	CAL	A	80	1
CIR X-1	15 20 41.0	-57 10 00.0	XRB	B	40	2
XTE J1550-564	15 50 58.7	-56 28 36.0	XRB	A(TOO)	40	1
ABELL 2142	15 58 22.1	+27 13 22.8	EDS	B	80	1

Target	RA	Dec	Cat.	Pri.	Exp.	#obs
RHO OPH CORE F	16 27 28.0	-24 39 33.5	SFR	A	200	1
4U1624-49	16 28 02.4	-49 11 25.0	XRБ	B	40	1
A 2199	16 28 37.0	+39 31 28.0	EDS	B	100	1
4U1626-67	16 32 16.8	-67 27 43.0	XRБ	B	100	1
4U1626-67	16 32 16.8	-67 27 43.0	CAL	A	5	1
A2218	16 35 52.3	+66 12 35.0	EDS	B	140	1
XTE J1650-500	16 50 01.0	-49 57 45.0	XRБ	A(TOO)	40	1
GRO J1655-40	16 54 00.0	-39 50 43.4	XRБ	A(TOO)	40	1
HER X-1	16 57 49.8	+35 20 32.6	XRБ	B	60	3
GX 339-4	17 02 49.5	-48 47 23.0	XRБ	A(TOO)	40	1
A 2256 OFFSET	17 03 20.0	+78 39 12.0	EDS	A	60	1
A 2256 CENTER	17 04 10.0	+78 38 00.0	EDS	A	40	1
KEPLER	17 30 42.4	-21 28 48.5	GDE	B	100	1
THE RIDGE EMISSION	17 45 30.0	-29 06 00.0	GDE	A	100	1
THE RIDGE EMISSION	17 45 30.0	-29 06 00.0	GDE	B	100	1
THE GALACTIC CENTER	17 45 31.1	-29 02 29.0	GDE	A	100	1
SGR A	17 45 44.1	-29 00 23.0	GDE	A	60	1
RADIO ARC	17 46 18.6	-28 53 48.0	GDE	B	100	1
1E1743.1-2843	17 46 21.0	-28 43 44.0	XRБ	A	100	1
SGR B2	17 47 20.1	-28 23 12.0	GDE	A	100	1
GX 13+1	18 14 31.0	-17 09 26.0	XRБ	A	50	1
AM HERCULIS	18 16 13.3	+49 52 04.2	XRБ	B	80	1
V4641 SGR	18 19 21.6	-25 24 25.1	XRБ	A(TOO)	40	1
4U 1822-37	18 25 46.7	-37 06 18.9	XRБ	B	40	1
VEGA	18 36 56.3	+38 47 01.3	CAL	A	10	1
IRAS18325-5926	18 36 58.0	-59 24 09.0	ECS	A	100	1
V603 AQL	18 48 54.5	+00 35 02.6	XRБ	B	80	1
W49B	19 11 11.1	+09 06 08.1	GDE	A	150	1
SS433	19 11 49.6	+04 58 57.7	XRБ	A	120	4
GRS 1915+105	19 15 11.0	+10 56 44.9	XRБ	A	80	1
CYG X-1	19 58 21.6	+35 12 06.1	XRБ	A(TOO)	40	1
CYG X-1	19 58 21.7	+35 12 05.8	XRБ	B	100	4
ABELL_3667_CENTER	20 12 32.5	-56 50 16.6	EDS	A	40	1
ABELL_3667_SE	20 13 00.4	-56 52 46.3	EDS	A	100	1
73P/SCHWASSMANN-WACH	20 26 48.8	+29 44 27.5	SFR	A	5	1
CYGNUS X-3	20 32 26.5	+40 57 09.0	XRБ	A	100	1
CYGNUS LOOP POS3	20 55 31.9	+31 52 48.4	GDE	A	30	1
CYGNUS LOOP POS2	20 55 45.9	+31 56 18.4	GDE	A	30	1
CYGNUS LOOP	20 55 59.9	+31 59 48.4	CAL	A	10	1
CYGNUS LOOP POS1	20 55 59.9	+31 59 48.4	GDE	A	40	1

Target	RA	Dec	Cat.	Pri.	Exp.	#obs
73P/SCHWASSMANN-WACH	21 20 37.0	+24 41 28.2	SFR	A	20	1
SS CYG (OUTBURST)	21 42 42.7	+43 35 09.5	XRB	A(TOO)	40	1
SS CYG (QUIESCENCE)	21 42 42.7	+43 35 09.5	XRB	A	40	1
NGC 7314	22 35 46.1	-26 03 02.2	ECS	A	100	1
CAS A W	23 23 12.1	+58 48 39.9	GDE	A	50	1
CAS A N	23 23 23.7	+58 50 22.4	GDE	A	50	1
CAS A	23 23 24.0	+58 48 54.0	CAL	A	12	4
CAS A	23 23 24.0	+58 48 54.0	CAL	A	12	4
CAS A	23 23 24.0	+58 48 54.0	CAL	A	3	1
CAS A	23 23 24.0	+58 48 54.0	CAL	A	3	1
CAS A	23 23 24.0	+58 48 54.0	CAL	A	3	1
CAS A	23 23 24.0	+58 48 54.0	CAL	A	3	1
CAS A E	23 23 40.2	+58 48 00.7	GDE	A	50	1
A2597	23 25 20.0	-12 07 30.0	EDS	B	50	1

### B.3 Target Constraints

Some of the SWG targets are constrained or unusual in some fashion. The constraints are listed below, ordered by RA and Declination. Observations listed with “BE” use the BE filter.

Target	RA	Dec	Exp.	#obs	Note
73P/SCHWASSMANN-WACH	01 24 08.4	-10 09 02.2	35	3	Obs 3, on 2006 June 12, 0UT
AXAF DEEP FIELD S	03 32 28.0	-27 48 30.0	140	1	Before XIS Door Open
VELA BULLET D	09 00 09.6	-45 54 54.8	50	1	BE
VELA X-1	09 02 06.8	-40 33 17.4	30	1	Phi orb=0.86-0.14
VELA X-1	09 02 06.8	-40 33 17.4	90	1	Phi orb =0.47-0.53
NGC 2992	09 45 42.0	-14 19 35.0	20	1	2 obs to be separated by > 6 months
NGC 2992	09 45 42.0	-14 19 35.0	20	1	2 obs to be separated by > 6 months
MRK421	11 04 27.3	+38 12 31.8	12	1	observe when $F_X$ (2-10 keV) > $3.5e - 10 \text{ erg/cm}^2/\text{s}$
GX 301-2	12 26 37.6	-62 46 13.0	50	2	Phi orb=0.96-0.98
GX 301-2	12 26 37.6	-62 46 13.0	70	2	Phi orb=0.20-0.22
GX301-2	12 26 37.6	-62 46 13.0	80	4	Phi orb=0.9-1.0, 4 pointings to illuminate the XRS array
3C273	12 29 06.7	+02 03 08.6	80	1	To be coordinated with <i>Chandra</i> and/or <i>XMM-Newton</i>
9P/TEMPEL1	13 37 25.0	-09 28 04.3	40	10	Observe at perihelion (July 4, 2005)
CIR X-1	15 20 41.0	-57 10 00.0	40	2	BE; Phi orb=0.9-0.2; two 20 ksec obs during contact orbits
XTE J1550-564(TOO)	15 50 58.7	-56 28 36.0	40	1	BE; observe when > 30 c/s in RXTE ASM
XTE J1650-500(TOO)	16 50 01.0	-49 57 45.0	40	1	BE
GRO J1655-40 (TOO)	16 54 00.0	-39 50 43.4	40	1	BE
HER X-1	16 57 49.8	+35 20 32.6	60	3	Main-on, outside eclipse
GX 339-4 (TOO)	17 02 49.5	-48 47 23.0	40	1	BE
V4641 SGR (TOO)	18 19 21.6	-25 24 25.1	40	1	Observe when > 30 mCrab using RXTE ASM
SS433	19 11 49.6	+04 58 57.7	120	4	4 obs in one orbital period required; 120 ksec at phase 0, 20 ksec at phase 0.25, 40 ksec at phase 0.5, 20 ksec at phase 0.75. Phases 20050321, 20050430, and 20050921 acceptable
CYG X-1 (TOO)	19 58 21.6	+35 12 06.1	40	1	BE; high/soft state
CYG X-1	19 58 21.7	+35 12 05.8	100	4	BE; at 4 orbital phases
73P/SCHWASSMANN-WACH	20 26 48.8	+29 44 27.5	5	1	Obs 1 on May 12, 2006
73P/SCHWASSMANN-WACH	21 20 37.0	+24 41 28.2	20	1	Obs 2 on May 14, 2006

# Appendix C

## Important Web/e-mail/postal addresses

### Primary Astro-E2 Sites

Japan: <http://www.astro.isas.jaxa.jp/astroe/>

US : <http://heasarc.gsfc.nasa.gov/docs/astroe/astroegof.html>

ESA: <http://www.rssd.esa.int/Astro-E2>

### Official US announcement:

[http://research.hq.nasa.gov/code\\_s/nra/current/nnh04zss001n-astroe2/index.html](http://research.hq.nasa.gov/code_s/nra/current/nnh04zss001n-astroe2/index.html)

### NASA Site for NOIs and Cover Pages:

<http://proposals.hq.nasa.gov>

### Astro-E2 GOF:

<http://heasarc.gsfc.nasa.gov/docs/astroe/astroegof.html>

The “Proposal & Tools” button is of particular note.

### Tools:

Viewing	<a href="http://heasarc.gsfc.nasa.gov/Tools/Viewing.html">http://heasarc.gsfc.nasa.gov/Tools/Viewing.html</a>
PIMMS	<a href="http://heasarc.gsfc.nasa.gov/docs/software/tools/pimms.html">http://heasarc.gsfc.nasa.gov/docs/software/tools/pimms.html</a>
MAKI	<a href="http://heasarc.gsfc.nasa.gov/Tools/maki/maki.html">http://heasarc.gsfc.nasa.gov/Tools/maki/maki.html</a>
XSPEC	<a href="http://heasarc.gsfc.nasa.gov/docs/xanadu/xspec/index.html">http://heasarc.gsfc.nasa.gov/docs/xanadu/xspec/index.html</a>
xrssim	<a href="http://heasarc.gsfc.nasa.gov/docs/astroe/prop_tools/xrssim/xrssim_usage.html">http://heasarc.gsfc.nasa.gov/docs/astroe/prop_tools/xrssim/xrssim_usage.html</a>
WebPIMMS	<a href="http://heasarc.gsfc.nasa.gov/Tools/w3pimms.html">http://heasarc.gsfc.nasa.gov/Tools/w3pimms.html</a>
WebSPEC	<a href="http://heasarc.gsfc.nasa.gov/webspec/webspec.html">http://heasarc.gsfc.nasa.gov/webspec/webspec.html</a>

### Questions:

The US GOF can be reached using the web form available at <http://heasarc.gsfc.nasa.gov/docs/astroe/as>

### Technical Description

Japan: <http://www.astro.isas.jaxa.jp/astroe/proposal>

US: [http://heasarc.gsfc.nasa.gov/docs/astroe/prop\\_tools/astroe2\\_td/](http://heasarc.gsfc.nasa.gov/docs/astroe/prop_tools/astroe2_td/)

ESA: <http://www.rssd.esa.int/index.php?project=ASTROE2&page=A0Docs>

US (ftp): [ftp://legacy.gsfc.nasa.gov/astroe2/nra\\_info/astroe2\\_td.ps.gz](ftp://legacy.gsfc.nasa.gov/astroe2/nra_info/astroe2_td.ps.gz) US (ftp):  
[ftp://legacy.gsfc.nasa.gov/astroe2/nra\\_info/astroe2\\_td.pdf](ftp://legacy.gsfc.nasa.gov/astroe2/nra_info/astroe2_td.pdf)

**SWG Target list**

Japan: [http://www.astro.isas.jaxa.jp/astroe/proposal/swg\\_lst.html](http://www.astro.isas.jaxa.jp/astroe/proposal/swg_lst.html)

US: [http://heasarc.gsfc.nasa.gov/docs/astroe/prop\\_tools/swg\\_lst.html](http://heasarc.gsfc.nasa.gov/docs/astroe/prop_tools/swg_lst.html)

**RPS (for Japanese proposals)**

<http://rps.astro.isas.jaxa.jp/RPS.pl>

**RPS (for US proposals)**

<http://heasarc.gsfc.nasa.gov/cgi-bin/RPS/ASTROE/RPS.pl>

(or email [rps@legacy.gsfc.nasa.gov](mailto:rps@legacy.gsfc.nasa.gov))

**RPS (for ESA proposals)**

<http://www.rssd.esa.int/cgi-bin/RPS/ASTROE/RPS.pl>

(or email [rps@rssd.esa.int](mailto:rps@rssd.esa.int))